

Theoretical Study on
the Nonlinear Model Order Reduction Method
and Its Application to Motor Analysis

Miwa Tobita

KYOTO UNIVERSITY

DOCTORAL THESIS

Theoretical Study on the
Nonlinear Model Order
Reduction Method and Its
Application to Motor Analysis

Author

Miwa Tobita

*A thesis submitted in fulfillment of the requirements
for the degree of Doctor of Philosophy*

in the

Department of Electrical Engineering
Graduate School of Engineering
Kyoto University

February 2024

This dissertation includes amended versions of the following articles.

©2022 IEEE. Reprinted, with permission, from “Nonlinear Model Order Reduction of Induction Motors Using Parameterized Cauer Ladder Network Method,” *IEEE Transactions on Magnetics*, vol. 58, no. 9, Art no. 8205504, Sept. 2022, doi: 10.1109/TMAG.2022.3171743.

©2022 IEEE. Reprinted, with permission, from “Nonlinear Model Order Reduction of a Variable Reluctance Stepper Motor Using the Parameterized Cauer Ladder Network Method,” *IEEE Transactions on Magnetics*, vol. 59, no. 5, Art no. 8200604, May 2023, doi: 10.1109/TMAG.2022.3232701.

©2023 IEEE. Reprinted, with permission, from “Hysteretic Finite Element Analysis Using a Semi-implicit Method Combined with the Predictor-Corrector Scheme,” *IEEE Transactions on Magnetics*, Early access, 2023, doi: 10.1109/TMAG.2023.3302875.

Reproduced from “A Model Order Reduction of Hysteretic Eddy-current Fields in Electric Machines Using Cauer Ladder Network Method,” *AIP Advances*, vol. 13, no. 2, Art no. 025208, February 2023, doi: 10.1063/9.0000417, with the permission of AIP Publishing.

Acknowledgments

First and foremost, I would like to express my sincere gratitude to Prof. Tetsuji Matsuo for his invaluable guidance throughout the research process. His direction, actions, and remarks not only allowed me to focus on essential issues but also demonstrated that genuine confidence exists quietly within.

I am grateful to Prof. Takashi Hikihara for inspiring me to explore unfamiliar territories and think beyond conventional boundaries. His encouragement to pursue a doctorate and insights into potential career paths are greatly appreciated.

I extend my heartfelt gratitude to Prof. Shinji Doi, whose support extended beyond technical guidance to include engaging conversations and a philosophical perspective encompassing informatics, linguistics, and playwriting.

I would like to thank Prof. Yoshiharu Omura for igniting my enthusiasm for discovering unknown phenomena. His mission-oriented spirit inspired me to cultivate a mindset of exploration.

Special appreciation goes to Prof. Stéphane Clénet, who attentively listened to my ideas, providing new perspectives and constructive feedback. Our discussions on culture and leadership broadened my outlook in both research and daily life.

I am deeply thankful to Prof. Takeshi Mifune for giving me insights, practical support, and warm encouragement, which were indispensable to this research.

I express my sincere thanks to Prof. Shingo Hiruma, whose reliable advice on fundamental and advanced theoretical development enhanced the overall depth of this research.

I appreciate Mr. Hideaki Nagamine for generously sharing his expertise and engaging in interesting discussions.

My thanks extend to Ms. Asumi Takenouchi, Mr. Katsuya Shimizu, Ms. Sumiko Taguchi, and the A cluster office staff for their generous assistance.

I greatly appreciate Mr. Wei Chen for enriching the possibilities of the parametric/parameterized CLN method through our exciting discussions.

Special recognition goes to Dr. Takashi Hirakawa, who provided emotional support during challenging phases.

Finally, I would like to express my deepest gratitude to my family. Their continuous encouragement and support were indispensable in completing this demanding journey.

Abstract

Electric motors play a pivotal role in vehicle electrification and industrial automation. For the optimal control and design of rare-earth-free motors such as induction motors (IMs) and variable reluctance (VR) stepper motors to be achieved, demand for transient eddy-current analyses with higher accuracy and speed than the conventionally widely-used finite element (FE) analysis is increasing. Moreover, motor dynamics are significantly influenced by the nonlinear magnetic characteristics of the iron core, which further increases the computational burden of the FE analysis.

To reduce the computation time of the nonlinear transient analysis, this thesis employs the model order reduction (MOR) method, which reduces the number of unknown variables without sacrificing accuracy. Leveraging the Cauer ladder network (CLN) method, a MOR method introduced in 2017, this thesis develops the parameterized CLN method to account for nonlinear magnetic characteristics, including magnetic hysteresis characteristics.

First, this thesis develops the parameterized CLN method to model nonlinear magnetic characteristics. The parameter variation is properly included in the state equations either through additional terms or by considering magnetic flux as a state variable.

Subsequently, the method is used to analyze an IM and stepper VR motor. The state of magnetic flux is used as a parameter to achieve both fast and accurate analysis for a wide range of operation points. The parameterized CLN method is further extended to incorporate magnetic hysteresis for accurate iron loss estimation.

This thesis also proposes the semi-implicit method to avoid convergence issues and reduce computation time in hysteresis FE analysis, which is used to obtain static loops for constructing the hysteresis model used in the CLN method.

The parameterized CLN method can be used as a behavior model for exploring the optimal control of IMs and VR stepper motors, facilitating an optimal control of electric machines even when the eddy currents largely influence the machine characteristics under high-frequency inputs.

Contents

Contents	vii
List of Figures	xi
1 General Introduction	1
1.1 Background	1
1.2 Review of Model Order Reduction Methods	2
1.2.1 Projection-based MOR Methods	3
Proper Orthogonal Decomposition Method	4
Dynamic Mode Decomposition Method	5
Pade via Lanczos Method	5
1.2.2 Equivalent Circuit Methods	6
Electric-equivalent Lumped-parameter Method	6
Equivalent Magnetic Network Method	6
1.3 Review of the Cauer Ladder Network Method	7
1.3.1 Theoretical Development	8
1.3.2 Application to 3D Analysis	9
1.3.3 Consideration of Nonlinear Magnetic Characteristics	9
1.3.4 Consideration of Hysteresis in the Standard Cauer Circuit for Modelling Iron Sheets	9
1.3.5 Multi-port Extension and Motor Application	10
1.4 Objective of This Thesis	11
1.5 Outline of This Thesis	12
2 Numerical Modeling of Electromagnetic Fields in Electric Ma- chines	15
2.1 Governing Equations of Eddy Current Fields	15
2.2 Boundary Conditions	17
2.3 Space Discretization	18
2.3.1 Weighted Residual Method	18
2.3.2 Galerkin Method Using the Whitney Form	20
Nodal Elements	21
Edge Elements	21
Facet Elements	21
Incidence Matrices	22

2.3.3	Discretized Eddy-Current Field Equations	22
2.4	Cauer Ladder Network Method	23
2.4.1	Single-port Cauer Ladder Network Method	24
2.4.2	Multi-port Cauer Ladder Network Method	27
2.4.3	Procedure of the CLN Method	28
2.4.4	Computation Time of the CLN Method Compared with FEM	29
3	Theoretical Development of the Parameterized CLN Method	31
3.1	Parameterized CLN Method	32
3.1.1	Parameterization of Reluctivity and Differential Reluctivity .	32
3.1.2	Parameterized CLN Method Based on Reluctivity	33
3.1.3	Parameterized CLN Method Based on Differential Reluctivity	35
3.2	Network Equations Using the Magnetic Flux as a Variable	37
3.3	Numerical Results	38
3.3.1	Offline Calculation	38
	Preparation of the Network Elements	38
	Preparation of the Parameter Variation Term	39
3.3.2	Online Calculation	42
3.3.3	Computation Time	44
3.3.4	Solution of Network Equations Using Magnetic Flux as a Variable	45
3.4	Summary	46
4	Analysis of Induction Motors Using the Parameterized Multi-port CLN	47
4.1	Parameterized Motor CLN	49
4.1.1	Definition of State Vectors on the Interface	49
4.1.2	State Equations Solved in the Online Calculation	51
	Stator	51
	Rotor	52
	Interface	52
	Solution of the State Equations	52
4.1.3	Parameterization of the Multi-port Network	52
	Parameterization of the Stator Inductance	53
	Selection of Parameter Vectors for IM Analysis	53
4.1.4	Offline Calculations	54
	Preparation of the Stator Inductance	54
	Preparation of the Rotor Network	55
4.2	Numerical Results	55
4.2.1	Offline Calculation of Stator Inductance	55
4.2.2	Online Computation	57
4.2.3	Computation Time	58
4.3	Summary	60

5	Analysis of Variable Reluctance Stepper Motors Using the Parameterized Multi-port CLN	61
5.1	Parameterized CLN for a Stepper Motor	61
5.1.1	Definition of Source Current and Parameters	62
5.1.2	Coupling with the Equation of Motion	63
5.2	Numerical Results	63
5.2.1	Offline Computation	64
5.2.2	Online Computation	66
	Continuous Rotation	66
	Stepwise Rotation and Step-out Motion	66
5.2.3	Evaluation of Computation Time	67
5.3	Summary	68
6	Hysteretic Magnetic Field as a Nonlinear Problem	69
6.1	Semi-implicit Method for FE Analysis	70
6.1.1	SI Method for Transient Analysis	70
6.1.2	Combination With the Predictor–Corrector Scheme	71
6.1.3	SI Method for Static Analysis	73
6.1.4	Numerical Results	73
6.1.4.1	Transient Analysis	75
	Sinusoidal input	75
	PWM input	76
6.1.4.2	Static Analysis	76
6.1.4.3	Comparison of the computation time	77
6.2	Hysteretic CLN Method	78
6.2.1	CLN Without Hysteresis	79
	CLN Recurrence Formula for a Laminated Core	79
	Parameterization	80
	State Equations	80
6.2.2	Construction of the Hysteretic CLN	81
6.2.3	Online Calculation of Hysteretic CLN	81
6.2.4	Numerical Analysis	83
6.2.4.1	Offline Calculation	83
	Preparation of Network Elements	83
	Identification of the Scalar Play Model	83
6.2.4.2	Online Calculation	84
6.2.4.3	Computation Time	85
6.3	Summary	87
7	Concluding Remarks	89
A	Newton–Raphson Method for Hysteretic FE Analysis of Laminated Cores	93
B	Play Model	95

B.1	Macroscopic Models of Magnetic Hysteresis	95
B.2	Scalar Play Model	95
B.3	Vector Play Model	97
	References	99

List of Figures

1.1	Concept of a projection-based MOR method; it reduces the number of unknown variables from N to N_r through projection onto a new set of basis vectors.	4
1.2	(a) Single-port and (b) multi-port Cauer ladder networks.	8
1.3	Outline of the thesis.	13
2.1	Definition of analysis domains and boundaries.	17
2.2	Overview of the structure of the CLN method.	24
2.3	Relationship between the basis vectors and network elements using an iron-cored inductor model as an example.	26
2.4	Procedure of the CLN method; first the network elements are prepared in the offline calculation, and then the state equations are solved in the online calculation.	29
2.5	Schematic illustration of the computation time; the CLN and FEM are compared.	29
3.1	CLN parametrized with α	32
3.2	Iron-cored inductor with dimensions in millimeters.	38
3.3	B–H characteristics of the iron core assumed in the simulation.	39
3.4	Result of (a) R_{2n} and (b) L_{2n+1} using ν	39
3.5	Results of (a) R_{2n}^d and (b) L_{2n+1}^d using ν^d	40
3.6	Result of $\mathbf{a}_{2k-1}^T \mathbf{K} d\mathbf{a}_{2n-1}/dI_1$ using ν	40
3.7	Result of $(\mathbf{a}_{2k-1}^d)^T d(\mathbf{K}^d \mathbf{a}_{2n-1}^d)/dI_1$ using ν^d	41
3.8	Results of L_1 and $L_1 + I_1 \mathbf{a}_1^T \mathbf{K} d\mathbf{a}_1/dI_1$ using ν	41
3.9	Results of L_1^d and $L_1^d + I_1 (\mathbf{a}_1^d)^T d(\mathbf{K}^d \mathbf{a}_1^d)/dI_1$	41
3.10	Transient waveform of the total current I_t obtained using the FEM, linear CLN method, and nonlinear CLN method with and without the parameter variation terms (nonlinear 1 and 2, respectively) when ν is used with $\alpha = I_1$. The applied electric field E_S is indicated as a blue solid line.	43
3.11	Transient waveform of the total current obtained using the FEM, linear CLN method, and nonlinear CLN method when ν^d is used with $\alpha = I_1$	43
3.12	Computational results of currents flowing through each stage of the CLN when ν is used. The parameter variation terms are neglected in (a) nonlinear 1, whereas they are included in (b) nonlinear 2.	44

3.13	Currents flowing through each stage of the CLN when ν^d is used (nonlinear d).	44
3.14	(a) Transient waveform of the total current obtained using the FEM, linear CLN method, and nonlinear CLN method where the network equation is directly derived from the CLN. (b) Currents flowing through each stage.	45
4.1	Network including the CLN for motor application.	48
4.2	Overview of the motor analysis using the parameterized CLN method.	48
4.3	State variables on the interface \mathbf{I} and Φ are defined such that $\mathbf{I} \cdot d\Phi/dt$ represents the Poynting vector flowing through the interface.	49
4.4	(a) Induction motor model, (b) mesh generated in the finite element space. The mesh for the stator and rotor domains is shown in different colors. ©2022 IEEE	56
4.5	(a) U-phase diagonal component, and (b) three-phase diagonal components ($I_{\text{src}} = 500$ AT) of the inductance \mathbf{L}_{00}	56
4.6	(a) The coil flux Φ_{coil} , and (b) the coil phase θ_{coil}	57
4.7	(a) The gap flux Φ_{gap} , and (b) the gap phase θ_{gap}	57
4.8	Amplitude of the input current I_{src}	58
4.9	Transient waveforms of (a) V-phase magnetic flux, and (b) torque. They were obtained using the FEM, linear CLN (L), nonlinear CLN parameterized by the source current (α_1), coil flux (α_2), and gap flux (α_3). ©2022 IEEE	59
4.10	Torque averaged in the final cycle with various (a) slips, and (b) input frequencies. ©2022 IEEE	59
5.1	Stator network including the stator winding resistance \mathbf{R}_s driven by a voltage source \mathbf{V}_{src}	62
5.2	Configuration of the VR stepper motor model analyzed in this study. ©2022 IEEE	64
5.3	(a) Trapezoidal and (b) rectangular current inputs. ©2022 IEEE	65
5.4	(a) Self-inductances L_{UU} , L_{VV} , and L_{WW} with $q = 1$. (b) Magnetic flux interlinking the coils. ©2022 IEEE	65
5.5	Time evolution of (a) electromagnetic torque and (b) rotor angle calculated using the parameterized CLN method (CLN), linear CLN (CLN Lin.), and FE analysis (FE). ©2022 IEEE	66
5.6	(a) Torque and (b) rotor angle of stepwise rotation. The results of the truncated network (Trunc.) are also shown. ©2022 IEEE	67
5.7	Time evolution of the (a) torque and (b) rotor angle when the load torque was small. A step-out motion was observed at $t = 1$ s. ©2022 IEEE	68
6.1	Procedure of the SI method combined with the PC scheme.	72
6.2	(a) Iron-core inductor used in the simulation. Point A indicates the probe for obtaining data from the local field. The unit of the dimension is mm. (b) Mesh created in (a). ©2023 IEEE	74

6.3	Symmetric B–H loop characteristics of the iron core given by the vector play model.	74
6.4	Results of the SI method with the sinusoidal electric field input E_s , which is plotted in (a). (b) Magnetic flux density at the probe. (c) PC difference d_{PC} and errors, e_P and e_C . ©2023 IEEE	75
6.5	H_y – B_y locus of the SI and NR method with (a) sinusoidal and (b) PWM inputs. ©2023 IEEE	76
6.6	Results of the SI method with the PWM input shown in (a). Magnified figures are shown on the right. The plotted parameters in (b) and (c) are the same as those in Fig. 6.4. ©2023 IEEE	77
6.7	Results of a static analysis using the SI method with the sinusoidal input shown in (a). The plotted parameters in (b) and (c) are the same as those in Fig. 6.4.	78
6.8	Static (a) H_y – B_y and (b) I – Φ loops of the SI and NR method.	78
6.9	(a) Cauer ladder network (CLN) without hysteresis, where the circuit elements are functions of flux Φ_1 . (b) CLN with hysteresis, constructed by replacing the inductances of (a). The first stage inductance, representing the DC magnetic field, incorporates magnetic hysteresis characteristics.	79
6.10	(a) Inductance and (b) resistance of the CLN as functions of I_1 without hysteresis characteristics. (c) CLN resistances as functions of the first stage magnetic flux $\Phi_1 = L_1 I_1$. (d) Ratio of the inductances L_{2k+1}/L_1 ($k = 1, 2$).	84
6.11	(a) Symmetric I – Φ loops obtained using FE static analysis. Four loops are shown out of 52 generated loops. (b) Loops produced using the identified scalar play model.	85
6.12	(a) Locus of the total current I_t and magnetic flux Φ_1 obtained using the non-hysteretic and hysteretic FE analyses (blue and red lines, respectively), proposed CLN method (solid black line), and truncated CLN (dotted black line). (b)(c) Magnified figures of (a). (d) Comparison of the iron loss.	86
B.1	Play hysteron with its width ζ [1]. It responds with some delay when the change in input X is inverted.	96

Chapter 1

General Introduction

1.1 Background

Electric motors play a central role in the electrification of automobiles as well as robotization and automation in industry. Owing to the limited availability of natural resources, rare-earth-free motors, such as induction motors (IMs) and variable reluctance (VR) stepper motors, can be in high demand in the coming decades. Electromagnetic field simulations can be prominent tools for optimizing the design and control of these motors; in particular, for automobiles and automation, the entire control system, including the power converter, should be optimized. For motor operations to be tested under various conditions, fast transient analyses with high accuracy are required.

Furthermore, recent developments in semiconductor technologies have enabled the switching frequency of power converters to be up to several hundred kilohertz. The eddy currents generated by the high harmonic components can have a significant impact on motor characteristics.

A major challenge in the electromagnetic simulation of motors with such high frequencies is an excessively long computation time, particularly for the transient analysis in control applications. While the finite element method (FEM) is widely used for motor analysis because of its high accuracy, its computational cost can be exceedingly large because it requires a large number of unknown variables. Moreover, the analysis of high-frequency input demands a smaller timestep and finer computational mesh, which further increases the computational cost. Executing

the FEM for all operation conditions required for the optimization of variable-speed control systems is unrealistically time-consuming.

Therefore, in recent years, model order reduction (MOR) methods have been actively studied to reduce the computation time while maintaining computational accuracy. MOR methods produce a reduced model, which ideally reproduces the characteristics of the original full model but has significantly fewer unknown variables.

In addition, nonlinear MOR methods [2–5] have been vigorously investigated because the nonlinear magnetic characteristics of the iron core significantly impact motor dynamics. However, this has been a challenge because nonlinearity adds complexity to the dynamics, and constructing a reduced model that can represent all the possible states becomes extremely costly. For IMs and stepper VR motors, in particular, simultaneously handling the nonlinearity of material characteristics and the input containing high-frequency temporal components with MOR is difficult. Additionally, spatial harmonics caused by nonuniform motor structures should be properly represented by the reduced model. Existing nonlinear MORs cannot produce reliable results for transient operations with various input frequencies, amplitudes, and slips of IMs or mechanical load angles of stepper motors.

This thesis aims to establish a nonlinear MOR for electric machines, particularly for IMs and VR stepper motors through the Cauer ladder network (CLN) method. The CLN method has been extensively studied over the past few years since it was first proposed in Ref. [6]. The following sections review the CLN method and other MOR methods.

1.2 Review of Model Order Reduction Methods

Among several types of MOR methods, projection-based MOR methods are promising tools for significantly reducing the number of unknown variables; hence, they are reviewed in the following. The CLN method can be considered a projection-based MOR method. Equivalent magnetic and electric circuits are conventionally widely used as surrogate models and are also summarized in Section 1.2.2. They rely heavily on the physical interpretation, whereas the projection-based MOR method is fundamentally a mathematical approach.

1.2.1 Projection-based MOR Methods

Projection-based MOR methods reduce the number of unknown variables defined in the finite element (FE) space by constructing a set of new basis vectors and using only dominant basis vectors for computation so that significantly fewer variables can represent the original model without losing much information. The following explanation focuses on *a posteriori* MOR, where the basis vectors for order reduction are prepared before executing transient calculations.

Fig. 1.1 depicts the concept of a projection-based MOR method. In the FE analysis (left part of the figure), the field equations are solved by assigning field variables to finite elements, such as nodes, edges, and facet elements. The resultant discretized equation has N unknown variables, where N is the number of finite elements. In the analysis of a complicated geometry such as an electric motor, N can be more than ten thousand, and solving the linear equation multiple times (for each time step and iteration for nonlinear solutions) can be time consuming. Projection-based MOR methods reduce the number of unknown variables from N to N_r through the following two steps:

Step 1: Construct a new set of basis vectors. Some methods execute spatial and/or temporal mode decomposition on the state vectors of the characteristic operations of the full model, and employ the resultant modes for the new basis vectors.

Step 2: Select the first N_r dominant basis vectors and construct a reduced model (right part of the figure) by projecting the state vectors onto the selected bases. The equation in the reduced space involves only the coefficients of the N_r bases.

For fast and accurate analysis, N_r should be much smaller than N but sufficiently large to contain essential information of the full system.

Among numerous methods that have been studied, the proper orthogonal decomposition (POD) method and dynamic mode decomposition (DMD) method are considered promising candidates for the electromagnetic field analysis of motors. Moreover, the Pade via Lanczos (PVL) method has been extensively studied mathematically. The applications and limitations of these methods are discussed in the following.

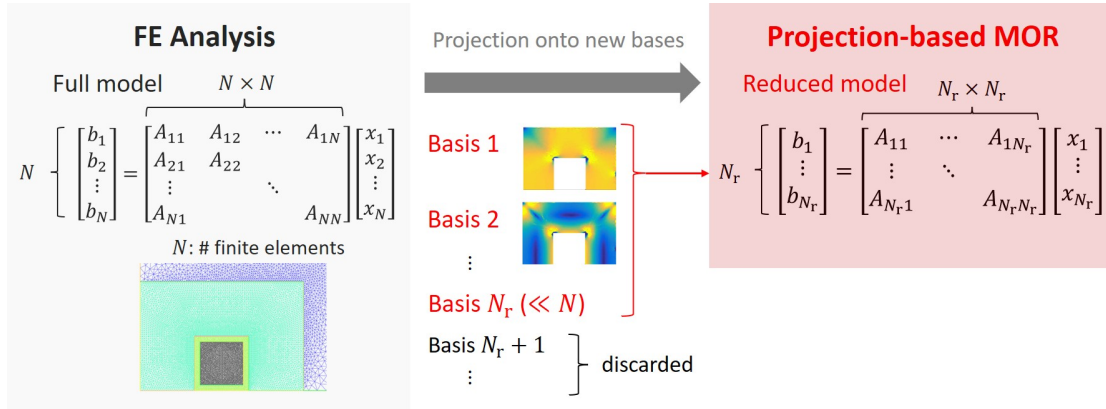


Figure 1.1: Concept of a projection-based MOR method; it reduces the number of unknown variables from N to N_r through projection onto a new set of basis vectors.

Proper Orthogonal Decomposition Method The POD method obtains basis vectors by applying the singular value decomposition (SVD) to snapshots, which consist of state variables of characteristic operations. Selecting appropriate snapshots as input data is the key to successfully creating an effective reduced model. The data is frequently obtained by executing the FE analysis for a limited number of operation conditions. SVD is used as the mode decomposition technique to construct the reduced model. Detailed explanations of the method are available in Ref. [7].

Ref. [8] applied the POD method to models with moving parts, and a permanent magnet synchronous machine (PMSM) was analyzed with the assumption of linear magnetic characteristics. The method involved constructing a basis from snapshots of vector and scalar potentials obtained evenly across all ranges of the mechanical angle. Ref. [9] further reduced the number of snapshots and unknown variables without degrading accuracy by dividing the mechanical angle at fixed intervals and constructing different bases for each division.

The application to IM analysis was reported in [10], which assumed linear magnetic characteristics. The snapshot matrix was constructed by sampling the states of the traditional no-load and locked tests. The starting motion was analyzed with an acceptable error when the frequency was constant. The study did not show whether the approach remains effective when the input frequency dynamically changes.

A major limitation of the method is that the accuracy deteriorates when all the possible states cannot be fully captured by the selected snapshots. Particularly,

when the magnetic saturation in the iron core is significant, including all the possible states in the basis generation is impossible. The POD method can exhibit a relatively large error of approximately 10% [9].

The gappy-POD method and POD-discrete empirical interpolation method (POD-DEIM) have been developed to include nonlinearity. These methods extract a limited number of sampling points of unknown variables from the nonlinear terms of the original system. They were used for the transient analysis of a single-phase power transformer [5]. Furthermore, a PMSM was analyzed using the POD-DEIM [11].

However, the use of the POD for the nonlinear simulation of eddy current fields in IMs and VR stepper motors remains an open problem. Refs. [12] and [13] performed a static magnetic field analysis of a switched reluctance machine and a bearingless synchronous reluctance motor, respectively, considering magnetic saturation. The limitation of both studies was that they neglected eddy currents, which can have a significant impact on the operation of IMs and VR stepper motors.

Dynamic Mode Decomposition Method The DMD method solves the time evolution of a system by obtaining the eigenvalues and vectors of a linear operator, which represents the temporal difference of snapshot vectors. The eigenvectors are derived in a reduced space whose bases are dominant singular vectors of the linear operator. The DMD method differs from the POD method in that not only the spatial mode but also the temporal difference is considered. It was applied to the magnetostatic field analysis of an interior permanent magnet synchronous motor (IPMSM), where eddy currents were not considered [14].

The limitation of this method also results from using the snapshot matrix; the error can increase when the states exhibit complex dynamics due to nonlinear material characteristics, eddy currents, and highly transient operations.

Pade via Lanczos Method The PVL method reduces the computational cost by applying the indirect moment matching to the transfer function matrix, which represents the input-output relationship of a linear equation system, and generating a lower-order transfer function matrix (Pade approximants) [15]. It was

applied to produce reduced-order models of electromagnetic problems involving multi-turn coils [16].

Although it is mathematically well established and has been extended to the block Lanczos algorithm for multiple-input multiple-output system [17, 18], it lacks physical interpretation such as an electric circuit representation. This hinders its application to complex problems; motor analysis using the PVL method as a principal method has not yet been reported.

1.2.2 Equivalent Circuit Methods

Electric-equivalent Lumped-parameter Method Simple electric-equivalent circuit representations, such as the d - q machine model and T-type and L-type equivalent circuits, have been widely used for the fast analysis of motors. In the circuits, the resistors represent loss and power output, and the inductors represent the coupling of magnetic flux between the stator and rotor and leaked flux.

Because the complex structure of the motor and the nonlinear characteristics of the material cannot be fully represented by the electric-equivalent circuit, computational accuracy cannot be satisfactory in the wide range of operations.

Equivalent Magnetic Network Method More elaborate equivalent circuit methods have been developed for constructing equivalent circuits from the physical phenomena and/or the material distribution. One of the most prevailing methods is the equivalent magnetic network (EMN) method.

The EMN method models a complex magnetic system as a network of simpler magnetic circuits. Several types of EMN have been developed, and the reluctance network analysis (RNA) is particularly suitable for addressing the dynamic modeling of flux distributions in the air gap for motors [19].

The EMN represents the flux paths of the cross-section of an electric machine in the form of a magnetic circuit. The circuit generally consists of two types of components: reluctance elements representing the spatial distribution of the magnetic reluctance of the material and power sources representing the magnetomotive force. Transient analysis of the magnetic circuit substitutes the mesh-based FE analysis.

The EMN is also adaptable to nonlinear magnetic materials by using the nonlinear permeances. Studies have also shown that the magnetic hysteresis characteristics can be incorporated by determining a circuit component based on the hysteresis modeling method. The method was applied to PMSM analysis [20]. The eddy-current loss was also represented by an additional circuit component.

The method can suffer from a trade-off between computation cost and accuracy. The number of circuit elements should be increased to accurately represent the distribution of magnetic flux, but the computation time also increases significantly, particularly when the nonlinear/hysteretic magnetic characteristics are considered. The EMN further lacks a method for systematic construction, which means that the constitution of the network is determined to reflect the experience and expectations of the designer.

1.3 Review of the Cauer Ladder Network Method

The CLN method is a projection-based MOR technique, where basis vectors are constructed by solving the CLN recurrence formula described in Section 2.4. The CLN method reduces the distribution of the electromagnetic field inside the electric machines to the network elements of the CLN, as shown in Fig. 1.2. The network elements are derived from the basis vectors of the reduced model. Unlike MOR methods based on the conventional mode decomposition techniques, the essential spatial modes of the eddy-current field can be efficiently extracted through hierarchical basis construction; hence, the CLN method shows superior convergence in high-frequency conditions [21].

The circuit expression provides a straightforward physical interpretation, which is useful for extension to modeling motors and including hysteretic material characteristics, as described in the following sections. Moreover, the network equations can be solved using commercial circuit solvers in a negligible amount of time, which offers easy implementation of analysis coupled with mechanical, heat, and control systems.

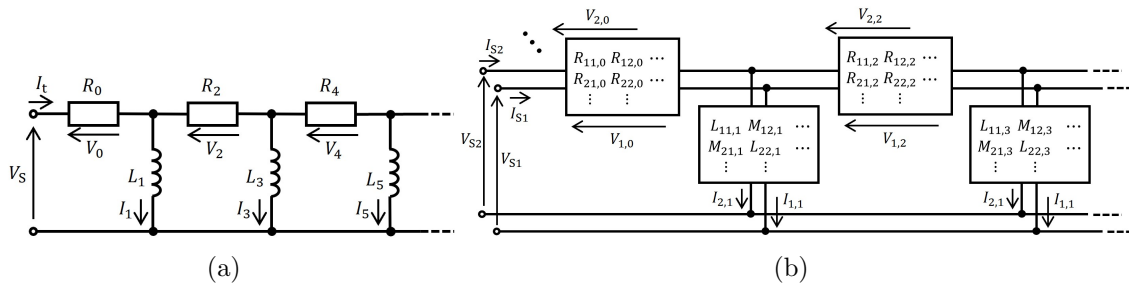


Figure 1.2: (a) Single-port and (b) multi-port Cauer ladder networks.

1.3.1 Theoretical Development

Before the CLN method was invented, the Cauer ladder circuit was known to be effective in modeling the iron losses of steel sheets [22–24]; the ladder circuit represents the continued fraction expansion of the ratio of the surface magnetic field to the average magnetic flux density. It was proved by Ref. [23] to be identical to the homogenization method utilizing Legendre polynomials as basis functions [25, 26], resulting in the clarification of its physical meaning [24].

Ref. [6] generalized the method for modeling electric machines without any restrictions in shapes and material distributions, which was the beginning of the CLN method. The CLN recurrence formula for generating the circuit elements was derived from the eddy-current equations and Cauer network equations assuming the continuous field. Joule losses and magnetic energies were equated with the summation of the energies computed from the decomposed modes and circuit elements.

A matrix formulation of the CLN method was derived in [21]. The circuit equations and CLN recurrence formula were derived, and proof of orthogonality of basis vectors based on energy norms was provided using variable vectors and matrices discretized in the FE space. The study also showed that the transformation of the CLN recurrence formula provides three-term recurrence formulae, from which two types of bi-Lanczos processes are obtained, whereas the PVL method contains one bi-Lanczos process. The numerical result of the CLN method terminated with a resistance agreed with that of the PVL method. Ref. [27] further clarified the connection between the CLN method discretized in the FE space and the PVL method; the discretized CLN algorithm can basically be considered to be the Lanczos algorithm, on which the PVL method is based.

1.3.2 Application to 3D Analysis

The scalar potential was introduced to the CLN recurrence formula in Ref. [5], which laid the foundation for the CLN analysis of 3D models with general coil connections including multiple conductors and stranded coils.

Ref. [28] presented the CLN formulation with magnetic vector potential A and current vector potential T . Ref. [29] combined the A - T formulation with the solution of scalar potentials, which can be solved using nodal elements and thus contributes to speeding up the computation. The vector potentials are derived from the scalar potentials through a fast projection technique [30].

1.3.3 Consideration of Nonlinear Magnetic Characteristics

Ref. [31] developed a single-port CLN that incorporates nonlinear material characteristics. The magnetic saturation in the iron core was represented by changing the circuit elements, which were prepared at several points in a range of a parameter, whose choice will be explained in detail in Chapter 3. The nonlinear CLN satisfactorily reproduced the transient response of an iron-core inductor even when the input voltage was sufficiently high for the core to exhibit nonlinearity.

1.3.4 Consideration of Hysteresis in the Standard Cauer Circuit for Modelling Iron Sheets

The standard Cauer circuit has been studied for modeling iron sheets, which laid the foundation for considering the magnetic hysteresis characteristics. Ref. [23] assumed that the magnetic field and magnetic flux density were decomposed to Legendre polynomials and their time-varying coefficients and proved that the Cauer circuit representation is derived from the governing equation of the one-dimensional quasi-static magnetic field along the thickness direction of a sheet.

The study clarified the physical meaning of the standard Cauer circuit; the following successive relationships are represented by the ladder network. When an external magnetic field is applied to an iron sheet, the main magnetic flux uniformly distributes along the thickness direction. It corresponds to the magnetic flux induced in the first inductor of the ladder circuit. Consequently, according

to Faraday's induction law, the time variation of the main magnetic flux induces an electromotive force that distributes linearly along the thickness direction. The eddy current resulting from the electromotive force corresponds to the current flowing through the first resistor of the ladder circuit. Furthermore, a counter magnetic field generated by the eddy current exhibits a quadratic distribution according to Ampere's circuital law, which corresponds to the magnetic flux created by the second inductor of the ladder circuit.

Exploiting the physical meaning, Ref. [23] further assumed that the nonlinear and hysteretic magnetic characteristics dominantly appear in the DC magnetic field and represented the hysteresis characteristics in the first inductor. This study will be detailed in Chapter 6.

1.3.5 Multi-port Extension and Motor Application

The CLN method was extended from a single-port model (Fig.1.2(a)) to a multi-port model (Fig.1.2(b)) for the application to multiple-input multiple-output systems. Ref. [32] showed that the matrix formulation of the single-port CLN can be naturally extended to a multi-port CLN; the impedances are converted from scalar values to $M \times M$ matrices, and currents and voltages at the elements are represented in vectors of size M , where M is the number of ports.

The multi-port CLN method was applied to analyze the motional electromotive force of linear IMs [33]. Stator and mover parts represented by the multi-port CLN were connected with the Fourier spatial harmonic components. The motional electromotive force was effectively incorporated from the boundary condition of the magnetic field on the interface between the stator and mover domains. It should be emphasized that this approach enabled the identical CLN to be used regardless of the position of the mover domain. The motor CLN effectively reproduced the generated force of the linear IM, which is significantly influenced by the induced eddy currents in the moving conductors in the mover CLN.

The established motor CLN was applied to analyze rotating machines [34], where only the dominant spatial harmonics were used for the calculation to reduce the computation time. The scalar potential was included in the CLN recurrence formula to satisfy the condition that the sum of eddy currents flowing through rotor bars among one pole pair is zero. Ref. [35] further reported that a skewed

rotor bar can also be analyzed by connecting the rotor CLN of a three-dimensional sliced model.

1.4 Objective of This Thesis

The objective of this thesis is to theoretically develop a parameterized CLN method. The developed theory is applied to the analysis of electric machines, particularly IMs and VR stepper motors. The parameterized CLN method is further developed to incorporate the magnetic hysteresis characteristics, which also influence the performance of electric machines.

The relation between previous research is summarized as follows:

- The theoretical basis of this thesis relies on the formulation of the single-port and multi-port CLN method in the discretized form [21, 32], as well as motor CLN formulated in Ref. [33].
- Ref. [31] developed the parameterized representation of the CLN to incorporate the degree of magnetic saturation. The dynamical behavior of the reduced bases, however, has not been rigorously discussed with time-varying orthogonal basis functions. This thesis derives the exact state equations of reduced systems, including the variation of the basis functions.
- The CLN method was extended to a multi-port model and applied to the analysis of IMs (Section 1.3.5). However, only the linear magnetic characteristics were considered in the previous studies. This thesis investigates the parameterization of the multi-port CLN to incorporate nonlinear magnetic characteristics.
- As indicated in Section 1.2, in the analysis of the IMs and VR stepper motors, conventional nonlinear MOR methods have difficulties in either analyzing eddy currents or simultaneously achieving low computational cost and high accuracy. This thesis aims to establish a fast and accurate nonlinear MOR of the eddy-current field.
- The reduced order model of magnetic materials has been studied using the Cauer network, and magnetic saturation and hysteresis

characteristics have been incorporated into the network, as mentioned in Section 1.3.4. This finding is exploited in this thesis to adapt the parameterized CLN method to analyze the hysteretic fields of electric machines.

- Sections 1.3.2 and 1.3.5 briefly mentioned that the preceding research introduced the scalar potential to the CLN formula. This thesis formulates the CLN recurrence formula for a 2D laminated coil model, where the gradient of scalar potentials at each sheet is designated as unknown variables.

This thesis addresses the following questions:

- How can the change in basis be incorporated into the state equations in the nonlinear CLN? (Chapter 3)
- Can the CLN method perform eddy current analysis of IMs and VR stepper motors when the nonlinear magnetic characteristics are considered? (Chapters 4 and 5)
- Can the CLN method model the hysteretic magnetic field? (Chapter 6)
- How much can the CLN method reduce computation time?

1.5 Outline of This Thesis

The outline of this thesis is shown in Fig. 1.3. After the introduction of the fundamental equations in Chapter 2, the parameterized CLN method is theoretically developed in Chapter 3. Thereafter, Chapters 4 and 5 apply the parameterized CLN method to the analysis of IMs and VR stepper motors, respectively. The incorporation of the magnetic hysteresis characteristics is described in Chapter 6.

The following summarizes each chapter:

- Chapter 2: The fundamentals of the single-port and multi-port CLN methods are introduced.

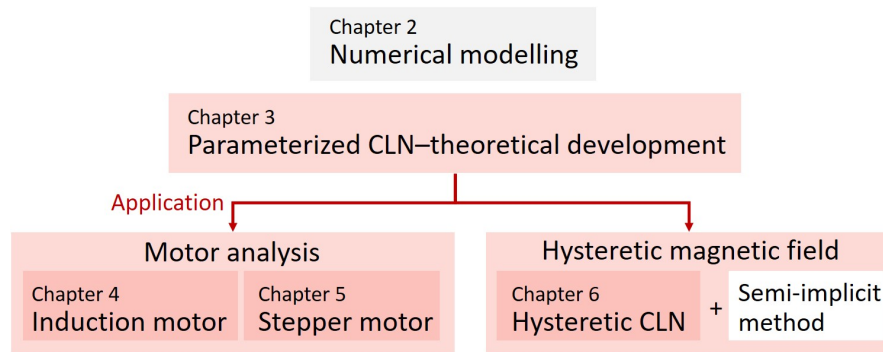


Figure 1.3: Outline of the thesis.

- Chapter 3: A theoretical study on the parameterized CLN method is conducted before developing the motor MOR. A general formulation for the parametrized CLN method is constructed with the time-varying orthogonal basis functions. Nonlinearities owing to the degree of magnetic saturation are specifically addressed.
- Chapter 4: The parameterized CLN method is applied to eddy-current simulations of a rotating induction motor by introducing the concept of parameterization to multi-port CLNs. The focus is specifically on selecting appropriate parameters to achieve high accuracy with a low computational cost.
- Chapter 5: The parameterized multi-port CLN constructed in Chapter 4 is further applied, with some modifications, to the eddy-current field analysis of a VR stepper motor. The dynamical operations, such as stepwise rotation and step-out motion, are simulated using the method.
- Chapter 6: Magnetic hysteresis characteristics are incorporated into the single-port parameterized CLN method. The hysteresis effect is represented by the first inductor of the CLN. Moreover, a time-stepping scheme for hysteretic FE analysis is developed to provide reliable static loops for constructing the hysteresis model in a short computation time.
- Chapter 7: Conclusions and future perspectives are presented.

Chapter 2

Numerical Modeling of Electromagnetic Fields in Electric Machines

This chapter introduces the fundamental equations of the eddy-current problems derived from Maxwell's equations, the space discretization method to solve the equations, and the CLN method to reduce the number of unknown variables of the discretized problem.

2.1 Governing Equations of Eddy Current Fields

This thesis considers problems in which the magnetoquasistatic approximation is valid, i.e., the displacement current is negligible; the target frequency of the analysis is below the MHz range, which hardly generates displacement current in magnetic materials constituting electric machines.

Omitting a term of displacement current in Maxwell's equations provides the governing equations of the eddy current field:

$$\nabla \times \mathbf{H} = \mathbf{J}, \quad (2.1)$$

$$\nabla \times \mathbf{E} = -\frac{\partial \mathbf{B}}{\partial t}, \quad (2.2)$$

$$\nabla \cdot \mathbf{B} = 0, \quad (2.3)$$

$$\nabla \cdot \mathbf{J} = 0, \quad (2.4)$$

where \mathbf{H} , \mathbf{J} , \mathbf{E} , and \mathbf{B} are variable vectors of the magnetic field, current density, electric field, and magnetic flux density, respectively.

The constitutive relationships are

$$\mathbf{H} = \nu \mathbf{B}, \quad (2.5)$$

$$\mathbf{J} = \sigma \mathbf{E} + \mathbf{J}_s = \mathbf{J}_e + \mathbf{J}_s, \quad (2.6)$$

where ν is the magnetic reluctivity, which is the inverse of the magnetic permeability μ , and σ is the electrical conductivity. The first term $\mathbf{J}_e = \sigma \mathbf{E}$ on the right-hand side of (2.6) represents the eddy current density, and the second term \mathbf{J}_s is the source current density.

In this thesis, eddy-current field equations are solved using \mathbf{A} - ϕ formulation, where \mathbf{A} and ϕ are the magnetic vector and electric scalar potentials, respectively. From (2.3), the existence of \mathbf{A} that satisfies

$$\nabla \times \mathbf{A} = \mathbf{B} \quad (2.7)$$

is guaranteed. The vector potential form of the eddy-current field equations is obtained by substituting (2.7), (2.5), and (2.6) into (2.1) and (2.2) as follows:

$$\nabla \times \nu \nabla \times \mathbf{A} = \sigma \mathbf{E} + \mathbf{J}_s, \quad (2.8)$$

$$\nabla \times \mathbf{E} = -\frac{\partial}{\partial t} \nabla \times \mathbf{A}. \quad (2.9)$$

Equation (2.9) implies the existence of the scalar potential ϕ that satisfies

$$\mathbf{E} + \frac{\partial \mathbf{A}}{\partial t} = -\nabla \phi. \quad (2.10)$$

From (2.4), (2.8), and (2.10), the \mathbf{A} - ϕ formulation is obtained as

$$\nabla \times \nu \nabla \times \mathbf{A} + \sigma \left(\frac{\partial \mathbf{A}}{\partial t} + \nabla \phi \right) = \mathbf{J}_s, \quad (2.11)$$

$$\nabla \cdot \sigma \left(\frac{\partial \mathbf{A}}{\partial t} + \nabla \phi \right) = 0. \quad (2.12)$$

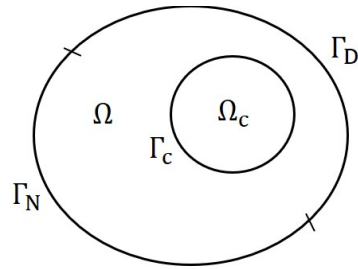


Figure 2.1: Definition of analysis domains and boundaries.

2.2 Boundary Conditions

The domain definition depicted in Fig. 2.1 is assumed hereafter. The entire domain Ω includes a conductive region Ω_c , outside of which the conductivity is zero. The boundary of Ω_c is represented by Γ_c . The Dirichlet and Neumann boundary conditions are imposed on the boundaries Γ_D and Γ_N , respectively.

For example, infinite boundaries within which the magnetic flux line is confined, or geometrical symmetric boundaries to which magnetic flux flows parallel, are handled as if the other side of the boundaries is the perfect electric conductor (PEC), and

$$\mathbf{E} \times \mathbf{n} = \mathbf{0}, \quad (2.13)$$

$$\mathbf{B} \cdot \mathbf{n} = 0, \quad (2.14)$$

are imposed, where \mathbf{n} is the unit vector normal on the boundary. Equation (2.14) is rewritten as $(\nabla \times \mathbf{A}) \cdot \mathbf{n} = 0$, and its sufficient condition is

$$\mathbf{A} \times \mathbf{n} = \mathbf{0}, \quad (2.15)$$

which is implemented as the Dirichlet boundary condition. From (2.10), (2.13), and (2.15), $\mathbf{n} \times \nabla \phi = \mathbf{0}$ is obtained; hence, the scalar potential must be constant on the boundary:

$$\phi = \text{const.}, \quad (2.16)$$

which is also imposed as the Dirichlet boundary condition.

When a symmetric boundary through which magnetic field lines cross perpendicularly is considered, the perfect magnetic conductor (PMC) conditions

$$\mathbf{H} \times \mathbf{n} = \mathbf{0}, \quad (2.17)$$

$$\mathbf{J}_e \cdot \mathbf{n} = 0, \quad (2.18)$$

are imposed. Equation (2.17) indicates that

$$(\nabla \times \mathbf{A}) \times \mathbf{n} = \mathbf{0}, \quad (2.19)$$

which is implemented as the Neumann boundary condition.

2.3 Space Discretization

If the target of the analysis has a simple geometry with uniform material characteristics, (2.8) and (2.9) could be analytically solved. However, in most practical engineering problems with complex shapes and material distribution, obtaining analytical solutions is extremely difficult, if not impossible. Instead, numerical analyses are often conducted by introducing the weighted residual method, which will be described in the following.

2.3.1 Weighted Residual Method

Equations (2.11) and (2.12) are called the strong form, where the second-order spatial differentiation of the variables must exist in the analysis region Ω . The weighted residual method summarized in this section derives a formulation with weaker restrictions, where only the existence of the first-order spatial differentiation is required. It solves (2.11) and (2.12) by determining the solution to the integrated form. The obtained equations are called the weak form. Because the weak form has continuity conditions that are more suitable to the actual potential characteristics, it can be more easily handled using numerical analyses. The derivation of the weak form is introduced in the following.

First, the notations of volume and boundary integrations are introduced for simplicity:

$$(u, v)_\Omega = \int_\Omega uv \, d\Omega, \quad (\mathbf{u}, \mathbf{v})_\Omega = \int_\Omega \mathbf{u} \cdot \mathbf{v} \, d\Omega, \quad (2.20)$$

$$\langle u, v \rangle_\Gamma = \int_\Gamma uv \, d\Gamma, \quad \langle \mathbf{u}, \mathbf{v} \rangle_\Gamma = \int_\Gamma \mathbf{u} \cdot \mathbf{v} \, d\Gamma. \quad (2.21)$$

From Gauss' theorem and the vector calculus identities, the integrations satisfy the following equations:

$$(\mathbf{u}, \nabla v)_\Omega + (\nabla \cdot \mathbf{u}, v)_\Omega = \langle v, \mathbf{u} \cdot \mathbf{n} \rangle_\Gamma, \quad (2.22)$$

$$(\nabla \times \mathbf{u}, \mathbf{v})_\Omega - (\mathbf{u}, \nabla \times \mathbf{v})_\Omega = \langle \mathbf{n}, \mathbf{u} \times \mathbf{v} \rangle_\Gamma. \quad (2.23)$$

Hereafter, we assume that the conductivity in Ω_c is σ . The multiplication of a differentiable vector function \mathbf{w} to (2.11) and integration over the entire region Ω result in the following equation.

$$(\mathbf{w}, \nabla \times \nu \nabla \times \mathbf{A})_\Omega + \left(\mathbf{w}, \sigma \frac{\partial \mathbf{A}}{\partial t} \right)_{\Omega_c} + (\mathbf{w}, \sigma \nabla \phi)_{\Omega_c} = (\mathbf{w}, \mathbf{J}_s)_{\Omega_c} \quad (2.24)$$

The non-uniformity of material characteristics is naturally incorporated into analyses through the discretization process.

Through a similar process, (2.25) is derived by multiplying a differential scalar function w to (2.12) and integrating it into the conductive region Ω_c .

$$\left(w, \nabla \cdot \sigma \left(\frac{\partial \mathbf{A}}{\partial t} + \nabla \phi \right) \right)_{\Omega_c} = 0 \quad (2.25)$$

If (2.24) and (2.25) are satisfied for any \mathbf{w} and w , (2.11) and (2.12) are also satisfied. The functions \mathbf{w} and w are generally called vector and scalar weighting functions, respectively.

The first term of (2.24) can be transformed using (2.23) as

$$(\mathbf{w}, \nabla \times \nu \nabla \times \mathbf{A})_\Omega = (\nabla \times \mathbf{w}, \nu \nabla \times \mathbf{A})_\Omega + \langle \mathbf{n}, \nu (\nabla \times \mathbf{A}) \times \mathbf{w} \rangle_\Gamma, \quad (2.26)$$

where the second term of the right-hand side

$$\langle \mathbf{n}, \nu (\nabla \times \mathbf{A}) \times \mathbf{w} \rangle_\Gamma = \langle \mathbf{w}, \mathbf{n} \times \mathbf{H} \rangle_\Gamma \quad (2.27)$$

is a boundary integration term, which represents the contribution from an externally provided magnetic field along the boundary. In the motor CLN, the unit source of the tangential magnetic field along the boundary is expressed by the boundary integration term, which is introduced in Chapter 4. When the PEC condition (2.15) or PMC condition (2.19) is applicable, the boundary integration term is omitted and (2.24) is transformed to

$$(\nabla \times \mathbf{w}, \nu \nabla \times \mathbf{A})_{\Omega} + \left(\mathbf{w}, \sigma \frac{\partial \mathbf{A}}{\partial t} \right)_{\Omega_c} + (\mathbf{w}, \sigma \nabla \phi)_{\Omega_c} = (\mathbf{w}, \mathbf{J}_s)_{\Omega}. \quad (2.28)$$

Similarly, the left-hand side of (2.25) is transformed using (2.22) as follows:

$$\left(w, \nabla \cdot \sigma \left(\frac{\partial \mathbf{A}}{\partial t} + \nabla \phi \right) \right)_{\Omega_c} = - \left(\sigma \left(\frac{\partial \mathbf{A}}{\partial t} + \nabla \phi \right), \nabla w \right)_{\Omega_c} + \langle \mathbf{J}_e \cdot \mathbf{n}, w \rangle_{\Gamma_c} \quad (2.29)$$

where

$$\mathbf{J}_e = \sigma \mathbf{E} = -\sigma \left(\frac{\partial \mathbf{A}}{\partial t} + \nabla \phi \right). \quad (2.30)$$

When the PEC condition (2.15) and (2.16) or PMC condition (2.18) is satisfied on Γ_c , the second term of (2.29) is neglected; hence,

$$\left(\sigma \left(\frac{\partial \mathbf{A}}{\partial t} + \nabla \phi \right), \nabla w \right)_{\Omega_c} = 0 \quad (2.31)$$

is obtained. Equations (2.28) and (2.31) comprise the weak form, which requires only piecewise continuity.

2.3.2 Galerkin Method Using the Whitney Form

The Galerkin method is commonly employed to solve the weak form. It assigns interpolation functions as the weight function at each element of the discretized space. The electromagnetic field is represented by a linear combination of the interpolation functions, whose coefficients become unknown variables.

The Whitney elements have compatibility with the differential form of electromagnetics [37, 38]; hence they are used as the interpolation functions in the following explanation.

Nodal Elements The scalar potential ϕ can be discretized as follows:

$$\phi = \sum_{i=1}^{N_n} \phi_i w_i^n, \quad (2.32)$$

where w_i^n is the Whitney nodal element, which is used as a scalar interpolation function, of the i -th node; it is one at the i -th node and zero at other nodes. N_n is the number of nodal elements in the analysis domain Ω , and ϕ_i is the value of the scalar potential ϕ at the i -th node. A variable vector of the scalar potential in the FE space is represented as

$$\boldsymbol{\phi} = [\phi_1, \phi_2, \dots, \phi_{N_n}]^T. \quad (2.33)$$

Edge Elements The Whitney edge element \boldsymbol{w}_i^e of the i -th edge directed from the j -th to the k -th node is defined with the nodal elements w_j^n and w_k^n as

$$\boldsymbol{w}_i^e = w_j^n \nabla w_k^n - w_k^n \nabla w_j^n. \quad (2.34)$$

The variables \boldsymbol{A} and \boldsymbol{E} are discretized using \boldsymbol{w}_i^e :

$$\boldsymbol{A} = \sum_{i=1}^{N_e} a_i \boldsymbol{w}_i^e, \quad \boldsymbol{E} = \sum_{i=1}^{N_e} e_i \boldsymbol{w}_i^e, \quad (2.35)$$

where N_e is the number of the edge elements in the analysis domain. Coefficients a_i and e_i are the line integrals of \boldsymbol{A} and \boldsymbol{E} , respectively, along the i -th edge. They construct vectors

$$\boldsymbol{a} = [a_1, a_2, \dots, a_{N_e}]^T, \quad \boldsymbol{e} = [e_1, e_2, \dots, e_{N_e}]^T. \quad (2.36)$$

Facet Elements The Whitney facet element \boldsymbol{w}_i^f of the i -th facet composed of the j -th, k -th, and l -th nodes is represented as

$$\boldsymbol{w}_i^f = 2 (w_j^n \nabla w_k^n \times \nabla w_l^n + w_l^n \nabla w_j^n \times \nabla w_k^n + w_k^n \nabla w_l^n \times \nabla w_j^n). \quad (2.37)$$

The vector \mathbf{B} is discretized in the finite element space as follows.

$$\mathbf{B} = \sum_{i=1}^{N_f} b_i \mathbf{w}_i^f, \quad (2.38)$$

where N_f is the number of facet elements in the analysis domain. The coefficient b_j is the surface integral of \mathbf{B} over the i -th face, and it comprises an FE vector

$$\mathbf{b} = [b_1, b_2, \dots, b_{N_f}]^T. \quad (2.39)$$

Incidence Matrices Matrices connecting the nodal, edge, and facet functions are called incidence matrices. The node-edge incidence matrix $\mathbf{G} = \{G_{ij}\} \in \mathbb{R}^{N_e \times N_n}$ and edge-face incidence matrix $\mathbf{C} = \{C_{jk}\} \in \mathbb{R}^{N_f \times N_e}$ satisfy the relationships

$$\nabla w_i^n = \sum_{j=1}^{N_e} G_{ji} \mathbf{w}_j^e, \quad \nabla \times \mathbf{w}_j^e = \sum_{k=1}^{N_f} C_{kj} \mathbf{w}_k^f. \quad (2.40)$$

From (2.7) and the discretized expressions (2.35)–(2.39) and (2.40), a relation $\mathbf{b} = \mathbf{C}\mathbf{a}$ is derived. This reveals that \mathbf{C} corresponds to the discretized representation of the curl operation. Similarly, if $\mathbf{E} = -\nabla\phi$ is satisfied as a special case of (2.10), $\mathbf{e} = -\mathbf{G}\phi$ can be derived using (2.32)–(2.36) and (2.40). The matrix \mathbf{G} is the discretized representation of the gradient operation. The relationship $\mathbf{C}\mathbf{G} = \mathbf{0}$, which corresponds to curl grad = 0, is satisfied.

2.3.3 Discretized Eddy-Current Field Equations

The weak form of the \mathbf{A} - ϕ formulation (2.28) and (2.31) is discretized with the variable vectors (2.33) and (2.36) and incidence matrix (2.40) as

$$\mathbf{C}^T \boldsymbol{\nu} \mathbf{C} \mathbf{a} + \boldsymbol{\sigma} \frac{d\mathbf{a}}{dt} + \boldsymbol{\sigma} \mathbf{G} \phi = \mathbf{j}_s, \quad (2.41)$$

$$\mathbf{G}^T \boldsymbol{\sigma} \frac{d\mathbf{a}}{dt} + \mathbf{G}^T \boldsymbol{\sigma} \mathbf{G} \phi = \mathbf{0}, \quad (2.42)$$

where $\mathbf{j}_s = [j_1, j_2, \dots, j_{N_e}]^T$ is a variable vector of the source current density, whose elements are obtained as $j_i = \int_{\Omega} \mathbf{J}_s \cdot \mathbf{w}_i^e d\Omega$. The matrices $\boldsymbol{\nu}$ and $\boldsymbol{\sigma}$ are reluctivity

and conductivity matrices, respectively, which are constructed as follows:

$$\boldsymbol{\nu} = \{\nu_{ij}\} \in \mathbb{R}^{N_f \times N_f}, \quad \nu_{ij} = (\boldsymbol{\nu} \mathbf{w}_i^f, \mathbf{w}_j^f)_\Omega, \quad (2.43)$$

$$\boldsymbol{\sigma} = \{\sigma_{ij}\} \in \mathbb{R}^{N_e \times N_e}, \quad \sigma_{ij} = (\boldsymbol{\sigma} \mathbf{w}_i^e, \mathbf{w}_j^e)_{\Omega_c}. \quad (2.44)$$

The constitutive representations are $\mathbf{h} = \boldsymbol{\nu} \mathbf{b}$ and $\mathbf{j}_e = \boldsymbol{\sigma} \mathbf{e}$, where \mathbf{h} and \mathbf{j}_e are the discretized vectors of the magnetic field and eddy-current density, respectively.

Similarly, (2.8) and (2.9) are discretized in the FE space as

$$\mathbf{C}^T \boldsymbol{\nu} \mathbf{C} \mathbf{a} = \boldsymbol{\sigma} \mathbf{e} + \mathbf{j}_s, \quad (2.45)$$

$$\mathbf{C} \mathbf{e} = -\frac{d}{dt} \mathbf{C} \mathbf{a}. \quad (2.46)$$

If $\mathbf{G}\phi$ can be set to zero in the analysis domain, (2.41) and (2.42) can be simplified into

$$\left(\mathbf{C}^T \boldsymbol{\nu} \mathbf{C} + \boldsymbol{\sigma} \frac{d}{dt} \right) \mathbf{a} = \mathbf{j}_s. \quad (2.47)$$

Chapters 3–5 mostly focus on problems in which the gauge $\mathbf{G}\phi = \mathbf{0}$ can be used. When eddy currents flow in unconnected multiple domains, the scalar potential must be used as a variable, which is discussed in Chapter 6.

2.4 Cauer Ladder Network Method

The CLN method consists of three components: the governing equations of the eddy-current field, the CLN recurrence formula, and the state equations of the CLN (Fig. 2.2). One of them is deducible from the other two when the linear material characteristics are assumed [6, 32]. The derivation of the state equations assuming the nonlinear magnetic characteristics is discussed in Chapter 3.

In this section, the linear magnetic characteristics are assumed, and the single-port CLN method (see Fig. 1.2(a)) is introduced. Subsequently, the multi-port CLN method, whose circuit elements are represented by matrices (Fig. 1.2(b)), is introduced as a natural extension of the single-port CLN.

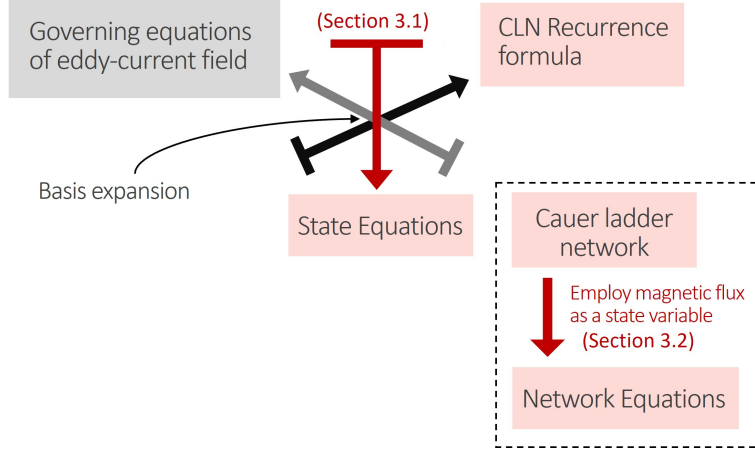


Figure 2.2: Overview of the structure of the CLN method.

2.4.1 Single-port Cauer Ladder Network Method

The CLN method provides an efficient decomposition

$$\mathbf{a}(t, \mathbf{x}) = \sum_k I_{2k+1}(t) \mathbf{a}_{2k+1}(\mathbf{x}) \quad (2.48)$$

$$\approx \sum_{k=0}^{N_s-1} I_{2k+1}(t) \mathbf{a}_{2k+1}(\mathbf{x}), \quad (2.49)$$

$$\mathbf{e}(t, \mathbf{x}) = \sum_k V_{2k}(t) \mathbf{e}_{2k}(\mathbf{x}) \quad (2.50)$$

$$\approx \sum_{k=0}^{N_s-1} V_{2k}(t) \mathbf{e}_{2k}(\mathbf{x}), \quad (2.51)$$

where $I_{2k+1}(t)$ and $V_{2k}(t)$ are the CLN current and voltage, respectively, at time t ; $\mathbf{a}_{2k+1}(\mathbf{x})$ and $\mathbf{e}_{2k}(\mathbf{x}) \in \mathbb{R}$ are the basis vectors as functions of space \mathbf{x} ; N_s is the number of stages of the CLN. The notations (t, \mathbf{x}) , (t) , and (\mathbf{x}) are omitted henceforward. The CLN method approximates the fields and constructs a reduced model of its dimension N_s using the first N_s bases as shown in (2.49) and (2.51). When the material characteristics are linear, the circuit equations obtained by applying Kirchhoff's voltage and current laws to the N_s -stage ladder network are

$$I_{2k+1} = \frac{V_{2k}}{R_{2k}} - \frac{V_{2k+2}}{R_{2k+2}}, \quad (k = 0, 1, \dots, N_s - 1) \quad (2.52)$$

$$V_{2k} = L_{2k-1} \frac{dI_{2k-1}}{dt} - L_{2k+1} \frac{dI_{2k+1}}{dt}, \quad (k = 1, 2, \dots, N_s - 1) \quad (2.53)$$

$$V_0 = V_s - L_1 \frac{dI_1}{dt}. \quad (2.54)$$

where V_s is the source voltage. Network elements L_{2n+1} and R_{2n} ($n = 0, 1, \dots, N_s - 1$) of the CLN are derived from

$$L_{2n+1} = \mathbf{a}_{2n+1}^T \mathbf{K} \mathbf{a}_{2n+1}, \quad 1/R_{2n} = \mathbf{e}_{2n}^T \boldsymbol{\sigma} \mathbf{e}_{2n}, \quad (2.55)$$

where $\mathbf{K} = \mathbf{C}^T \boldsymbol{\nu} \mathbf{C}$ is the stiffness matrix. Fig. 2.3 shows the relationship between the basis vectors and network elements.

The CLN transient analysis is performed by solving the state equations (2.52)–(2.54). The vector potential \mathbf{a} and electric field \mathbf{e} of the eddy-current field can be reproduced from the obtained I_{2k+1} and V_{2k} using (2.49) and (2.51).

The basis vectors are defined such that the instantaneous magnetic energy $W_m(t)$ and Joule loss $W_e(t)$ of the electromagnetic field are equal to those of the CLN:

$$2W_m(t) = \mathbf{a}^T \mathbf{K} \mathbf{a} = \sum_k L_{2k+1} I_{2k+1}^2 \quad (2.56)$$

$$\approx \sum_{k=0}^{N_s-1} L_{2k+1} I_{2k+1}^2, \quad (2.57)$$

$$W_e(t) = \mathbf{e}^T \boldsymbol{\sigma} \mathbf{e} = \sum_k V_{2k}^2 / R_{2k} \quad (2.58)$$

$$\approx \sum_{k=0}^{N_s-1} V_{2k}^2 / R_{2k}. \quad (2.59)$$

The linear magnetic characteristics are assumed in (2.56) and (2.57). Equations (2.56) and (2.58) demand the basis vectors to be orthogonal based on energy norms:

$$\mathbf{a}_{2i+1}^T \mathbf{K} \mathbf{a}_{2j+1} = \delta_{ij} L_{2i+1}, \quad \mathbf{e}_{2i}^T \boldsymbol{\sigma} \mathbf{e}_{2j} = \delta_{ij} / R_{2i}, \quad (2.60)$$

where δ_{ij} is the Kronecker delta.

The CLN recurrence formula with a fixed reluctivity matrix $\boldsymbol{\nu}$ is derived by substituting (2.49), (2.51), (2.52)–(2.54) into (2.45) and (2.46) as follows [6]:

$$\mathbf{K}(\mathbf{a}_{2n+1} - \mathbf{a}_{2n-1}) = R_{2n} \boldsymbol{\sigma} \mathbf{e}_{2n}, \quad (2.61)$$

$$\mathbf{C}(\mathbf{e}_{2n+2} - \mathbf{e}_{2n}) = -\frac{1}{L_{2n+1}} \mathbf{C} \mathbf{a}_{2n+1}. \quad (2.62)$$

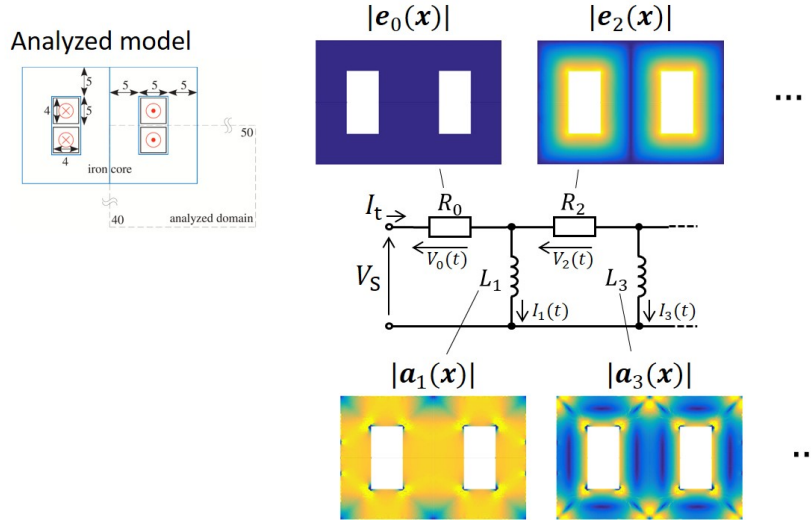


Figure 2.3: Relationship between the basis vectors and network elements using an iron-cored inductor model as an example.

When the gauge $\phi = \mathbf{0}$ is employed, (2.62) is rewritten as

$$\mathbf{e}_{2n+2} - \mathbf{e}_{2n} = -\frac{1}{L_{2n+1}} \mathbf{a}_{2n+1}. \quad (2.63)$$

When the CLN recurrence formula is solved, the unit source is used as its initial condition. When an electric field \mathbf{e}_s is supplied as a unit source, the initial condition

$$\mathbf{a}_{-1} = \mathbf{0}, \quad \mathbf{e}_0 = \mathbf{e}_s \quad (2.64)$$

is used, whereas the condition

$$\mathbf{e}_0 = \mathbf{0}, \quad \mathbf{K} \mathbf{a}_1 = \mathbf{j}_s \quad (2.65)$$

is employed when a unit current density \mathbf{j}_s is supplied. By solving (2.61) and (2.63) recursively with the initial condition (2.64) or (2.65), one can obtain basis vectors \mathbf{e}_{2n} and \mathbf{a}_{2n+1} and the network elements R_{2n} and L_{2n+1} . This derivation process of the CLN elements corresponds to the model reduction of the eddy-current field governed by (2.45) and (2.46).

2.4.2 Multi-port Cauer Ladder Network Method

The multi-port CLN can be constructed using a straightforward extension of the single-port CLN. The network equations of the multi-port CLN remain the same as the single-port network, except that the basis and circuit elements are expressed in matrix form.

Let M be the number of ports of the ladder network, and $\mathbf{I}_{2n-1}, \mathbf{V}_{2n} \in \mathbb{R}^M$ ($n = 1, 2, \dots, N_s$) be the state vectors of the current and voltage, respectively, at the n -th stage. It is assumed that the decompositions of \mathbf{a} and \mathbf{e} and their approximations are given as

$$\mathbf{a} = \sum_n \mathbf{a}_{2n-1} \mathbf{I}_{2n-1} \approx \sum_{n=1}^{N_s} \mathbf{a}_{2n-1} \mathbf{I}_{2n-1}, \quad (2.66)$$

$$\mathbf{e} = \sum_n \mathbf{e}_{2n} \mathbf{V}_{2n} \approx \sum_{n=1}^{N_s} \mathbf{e}_{2n} \mathbf{V}_{2n}, \quad (2.67)$$

where unlike (2.48)–(2.51), \mathbf{a}_{2n-1} and $\mathbf{e}_{2n} \in \mathbb{R}^{N_e \times M}$ are not vectors but matrices defined as

$$\mathbf{a}_{2n-1} = [\mathbf{a}_{1,2n-1}, \mathbf{a}_{2,2n-1}, \dots, \mathbf{a}_{M,2n-1}], \quad \mathbf{e}_{2n} = [\mathbf{e}_{1,2n}, \mathbf{e}_{2,2n}, \dots, \mathbf{e}_{M,2n}]. \quad (2.68)$$

Here, $\mathbf{a}_{m,2n-1}$ and $\mathbf{e}_{m,2n}$ ($m = 1, 2, \dots, M$) are the basis vectors of the magnetic vector potential and electric field, respectively, when a unit input is provided only to the m -th port [33].

The state equations of the N_s -stage ladder network are

$$\mathbf{V}_{2n} = \mathbf{L}_{2n-1} \frac{d\mathbf{I}_{2n-1}}{dt} - \mathbf{L}_{2n+1} \frac{d\mathbf{I}_{2n+1}}{dt}, \quad (2.69)$$

$$\mathbf{I}_{2n+1} = \mathbf{R}_{2n}^{-1} \mathbf{V}_{2n} - \mathbf{R}_{2n+2}^{-1} \mathbf{V}_{2n+2}, \quad (2.70)$$

for $n = 1, 2, \dots, N_s$, where \mathbf{L}_{2n-1} and \mathbf{R}_{2n} are the inductance and resistance matrices of the CLN, respectively.

With the assumption of the decompositions (2.66) and (2.67), the recurrence formula is derived from (2.45), (2.46), (2.69), and (2.70) as

$$\mathbf{K}(\mathbf{a}_{2n+1} - \mathbf{a}_{2n-1}) = \boldsymbol{\sigma} \mathbf{e}_{2n} \mathbf{R}_{2n}, \quad (2.71)$$

$$\mathbf{e}_{2n+2} - \mathbf{e}_{2n} = -\mathbf{a}_{2n+1} \mathbf{L}_{2n+1}^{-1}, \quad (2.72)$$

where $\mathbf{L}_{2n-1} = \mathbf{a}_{2n-1}^T \mathbf{K} \mathbf{a}_{2n-1}$ and $\mathbf{R}_{2n}^{-1} = \mathbf{e}_{2n}^T \boldsymbol{\sigma} \mathbf{e}_{2n}$. The initial conditions

$$\mathbf{e}_0 = \mathbf{0}, \quad \mathbf{K} \mathbf{a}_1 = \mathbf{j}_{\text{unit}} \quad (2.73)$$

are used assuming that a unit source

$$\mathbf{j}_{\text{unit}} = [\mathbf{j}_1, \mathbf{j}_2, \dots, \mathbf{j}_m, \dots, \mathbf{j}_M] \in \mathbb{R}^{N_e \times M} \quad (2.74)$$

is provided. Here, \mathbf{j}_m is an input vector discretized in the FE space when a unit input is given only to the m -th port. \mathbf{L}_{2n-1} and \mathbf{R}_{2n} are systematically obtained by solving (2.71) and (2.72) with the initial conditions.

2.4.3 Procedure of the CLN Method

The procedure for the execution of the CLN method is depicted in Fig. 2.4. The simulation of electric machines using the CLN method consists of the following steps:

Step 1: Network elements are derived by solving the CLN recurrence formula under appropriate initial conditions.

Step 2: State equations of the ladder network are solved with the network elements prepared in Step 1.

In this thesis, Steps 1 and 2 are called the offline and online calculations, respectively. When the offline calculation is completed in Step 1, the CLN can yield any output under any transient input only by solving the state equations in Step 2. Field vectors \mathbf{a} and \mathbf{e} , having more than ten-thousand unknowns, are reduced to the state vectors of the CLN, which have several hundred unknowns at most; hence, each time step of the online calculation of the CLN consumes significantly less time than that of the FEM.

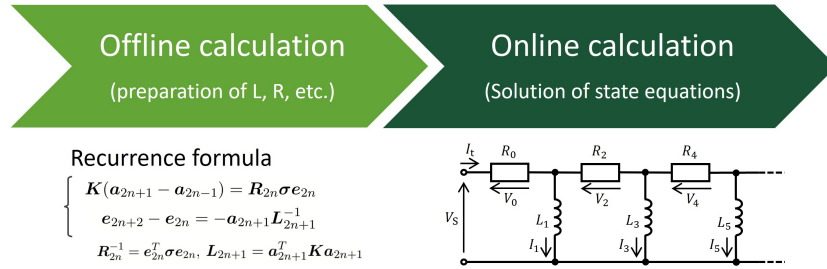


Figure 2.4: Procedure of the CLN method; first the network elements are prepared in the offline calculation, and then the state equations are solved in the online calculation.

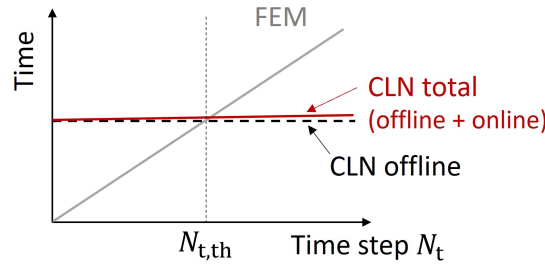


Figure 2.5: Schematic illustration of the computation time; the CLN and FEM are compared.

2.4.4 Computation Time of the CLN Method Compared with FEM

The computation time for the FEM and parameterized CLN is dominated by the solutions of the linear system in the FE space.

In the FEM, the computation time and number of time steps have a linear relation, as shown in Fig. 2.5. In contrast, the CLN method requires the solutions of the linear systems only in the offline computation, whose time consumption is independent of the number of time steps. The solution of state equations in the online computation consumes a negligible amount of time compared with the FEM. Therefore, as shown in Fig. 2.5, the CLN becomes faster than the FEM when the number of the time step is larger than a certain threshold $N_{t,th}$.

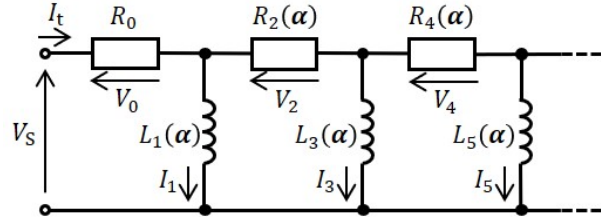
The CLN method is particularly effective in reducing the computation time when (a) large time steps are required, for instance, pulse-width modulation (PWM) input and transient input for a long duration, and (b) calculations are conducted under various conditions.

Chapter 3

Theoretical Development of the Parameterized CLN Method

In this chapter, the effect of the parameter variation on reduced systems is numerically studied, and a general formulation for the parametrized CLN method with a dynamical transition is developed. Two parameterized CLN representations are developed for handling the nonlinear magnetic field: one parameterizes reluctivity, and the other parameterizes differential reluctivity to reflect the degree of saturation.

Specifically, in Sections 3.1.2 and 3.1.3, the state equation is derived from the governing equations of the eddy current field and CLN recurrence formula in the presence of magnetic saturation. Moreover, in Section 3.2, the circuit equations are studied using the magnetic flux as state variables, as shown in the dashed box in Fig. 2.2.

Figure 3.1: CLN parametrized with α .

3.1 Parameterized CLN Method

3.1.1 Parameterization of Reluctivity and Differential Reluctivity

In this study, the reluctivity matrix $\boldsymbol{\nu}$ is parameterized using the degree of magnetic saturation. Because $\boldsymbol{\nu}$ depends on the magnetic flux density

$$\mathbf{b} = \sum I_{2n+1} \mathbf{C} \mathbf{a}_{2n+1} \approx \sum_{n=0}^{N_s-1} I_{2n+1} \mathbf{C} \mathbf{a}_{2n+1}, \quad (3.1)$$

it can be considered a function of $\boldsymbol{\alpha}$ in the parameterized CLN, as follows:

$$\boldsymbol{\nu} = \boldsymbol{\nu}(\boldsymbol{\alpha}), \quad \boldsymbol{\alpha} = (I_1, I_3, \dots, I_{2N_s-1}). \quad (3.2)$$

With the first-order (FO) approximation [31], which assumes that I_1 has a dominant impact on the saturation, it is approximated as a function of I_1 by selecting $\alpha = I_1$ as follows:

$$\boldsymbol{\nu} = \boldsymbol{\nu}(\alpha), \quad \alpha = I_1. \quad (3.3)$$

Fig. 3.1 shows a general form of the parameterized CLN, wherein the circuit elements derived using $\boldsymbol{\nu}(\alpha)$ are functions of α .

The CLN method can also be formulated using the differential reluctivity matrix $\boldsymbol{\nu}^d$ defined by

$$\boldsymbol{\nu}^d = \{\nu_{ij}^d\}, \quad \nu_{ij}^d = \left(\frac{\partial \mathbf{H}}{\partial \mathbf{B}} \mathbf{w}_i^f, \mathbf{w}_j^f \right)_{\Omega}, \quad (3.4)$$

where $\partial \mathbf{H}/\partial \mathbf{B}$ is a second-order tensor of the differential reluctivity. The reluctivity matrix $\boldsymbol{\nu}^d$ is also parameterized using the degree of saturation as follows.

$$\boldsymbol{\nu}^d = \boldsymbol{\nu}^d(\alpha), \quad \alpha = I_1 \quad (3.5)$$

3.1.2 Parameterized CLN Method Based on Reluctivity

The exact derivation of the nonlinear state equations is introduced in this section. State equations are derived by substituting the CLN recurrence formula (2.61) and (2.63) to the eddy-current field equations (2.45) and (2.46) with the assumption of basis expansion (2.49) and (2.51) and the orthogonality of the bases (2.60). In previous studies, the linear state equations (2.52)–(2.54) were derived when the reluctivity is constant, whereas those with the nonlinear reluctivity are derived in the following.

Substituting (2.49) and (2.51) into (2.45) and (2.46) yields the following equations:

$$\begin{aligned} \mathbf{K} \sum_{n=0}^{N_s-1} I_{2n+1} \mathbf{a}_{2n+1} &= \boldsymbol{\sigma} \sum_{n=0}^{N_s-1} V_{2n} \mathbf{e}_{2n}, \\ \mathbf{C} \sum_{n=0}^{N_s-1} V_{2n} \mathbf{e}_{2n} &= \mathbf{C} \sum_{n=0}^{N_s-1} V_{2n} \mathbf{e}_{2n} - \mathbf{C} V_S \mathbf{e}_0 \\ &= -\frac{d}{dt} \sum_{n=0}^{N_s-1} I_{2n+1} \mathbf{C} \mathbf{a}_{2n+1}, \end{aligned} \quad (3.6)$$

$$(3.7)$$

where the initial condition is given by \mathbf{e}_0 , which satisfies $\mathbf{C} \mathbf{e}_0 = \mathbf{0}$, and V_S is the source voltage. Equation (3.7) yields

$$\sum_{n=0}^{N_s-1} V_{2n} \mathbf{e}_{2n} - V_S \mathbf{e}_0 = -\frac{d}{dt} \sum_{n=0}^{N_s-1} I_{2n+1} \mathbf{a}_{2n+1}. \quad (3.8)$$

Multiplying $\mathbf{a}_{2k+1}/L_{2k+1}$ to both sides of (3.6) and using (2.60) and (2.63), one obtains

$$I_{2k+1} = \frac{V_{2k}}{R_{2k}} - \frac{V_{2k+2}}{R_{2k+2}}. \quad (k = 0, 1, \dots, N_s - 1) \quad (3.9)$$

Multiplying both sides of (3.8) by $R_{2k}\boldsymbol{\sigma}e_{2k}$ and substituting (2.61) results in the following equation:

$$R_{2k}\mathbf{e}_{2k}^T\boldsymbol{\sigma}\left(\sum_{n=0}^{N_s-1}V_{2n}\mathbf{e}_{2n}-V_S\mathbf{e}_0\right)=-\left(\mathbf{a}_{2k+1}-\mathbf{a}_{2k-1}\right)^T\mathbf{K}\frac{d}{dt}\sum_{n=0}^{N_s-1}I_{2n+1}\mathbf{a}_{2n+1}. \quad (3.10)$$

With (2.60) and (3.3), (3.10) is rewritten as

$$V_{2k}=-\left(L_{2k+1}\frac{dI_{2k+1}}{dt}-L_{2k-1}\frac{dI_{2k-1}}{dt}\right)-\left(\mathbf{a}_{2k+1}-\mathbf{a}_{2k-1}\right)^T\mathbf{K}\sum_{n=0}^{N_s-1}I_{2n+1}\frac{d\mathbf{a}_{2n+1}}{d\alpha}\frac{d\alpha}{dt}, \quad (k=1,\dots,N_s-1) \quad (3.11)$$

$$V_0=V_S-L_1\frac{dI_1}{dt}-\mathbf{a}_1^T\mathbf{K}\sum_{n=0}^{N_s-1}I_{2n+1}\frac{d\mathbf{a}_{2n+1}}{d\alpha}\frac{d\alpha}{dt}. \quad (3.12)$$

The last terms in (3.11) and (3.12) concerning $d\mathbf{a}_{2n+1}/d\alpha$ are called parameter variation terms here. They appear owing to the variation in the system parameter and are newly derived using an exact formulation of the parameterized CLN. When the FO approximation is applied, i.e., $\alpha=I_1$, the term including $d\mathbf{a}_{2n+1}/dI_1$ can be prepared in the offline calculation. The bases are obtained for each value of I_1 , and the difference between them provides the term.

On the condition that the parameter variation terms are negligible, (3.11) and (3.12) are approximated as

$$V_{2k}=-\left(L_{2k+1}\frac{dI_{2k+1}}{dt}-L_{2k-1}\frac{dI_{2k-1}}{dt}\right), \quad (k=1,2,\dots,N_s-1) \quad (3.13)$$

$$V_0=V_S-L_1\frac{dI_1}{dt}. \quad (3.14)$$

Equations (3.9), (3.13), and (3.14) correspond to the Cauer network equations with a constant reluctivity [21].

3.1.3 Parameterized CLN Method Based on Differential Reluctivity

When the differential reluctivity is used instead of the reluctivity, (2.45) and (2.46) are rewritten as

$$\mathbf{C}^T \mathbf{h} = \boldsymbol{\sigma} \mathbf{e}, \quad (3.15)$$

$$\mathbf{C} \mathbf{e} = -(\boldsymbol{\nu}^d)^{-1} \frac{d\mathbf{h}}{dt}, \quad (3.16)$$

where \mathbf{h} is the variable vector of the magnetic field.

The CLN method is assumed to provide spatial basis vectors, which can provide the approximated decompositions of the variable vectors \mathbf{h} and \mathbf{e} as follows:

$$\mathbf{h} = \sum_n I_{2n+1} \boldsymbol{\nu}^d \mathbf{C} \mathbf{a}_{2n+1}^d \approx \sum_{n=0}^{N_s-1} I_{2n+1} \boldsymbol{\nu}^d \mathbf{C} \mathbf{a}_{2n+1}^d, \quad (3.17)$$

$$\mathbf{e} = \sum_n V_{2n} \mathbf{e}_{2n}^d \approx \sum_{n=0}^{N_s-1} V_{2n} \mathbf{e}_{2n}^d. \quad (3.18)$$

The CLN procedure with the differential reluctivity matrix $\boldsymbol{\nu}^d$ for a fixed α consists of the following equations:

$$\mathbf{K}^d (\mathbf{a}_{2n+1}^d - \mathbf{a}_{2n-1}^d) = R_{2n}^d \boldsymbol{\sigma} \mathbf{e}_{2n}^d, \quad (3.19)$$

$$\mathbf{e}_{2n+2}^d - \mathbf{e}_{2n}^d = -\frac{1}{L_{2n+1}^d} \mathbf{a}_{2n+1}^d, \quad (3.20)$$

$$1/R_{2n}^d = (\mathbf{e}_{2n}^d)^T \boldsymbol{\sigma} \mathbf{e}_{2n}^d, \quad L_{2n+1}^d = (\mathbf{a}_{2n+1}^d)^T \mathbf{K}^d \mathbf{a}_{2n+1}^d, \quad (3.21)$$

where $\mathbf{K}^d = \mathbf{C}^T \boldsymbol{\nu}^d \mathbf{C}$. The basis vectors, network elements, and stiffness matrix are denoted by superscript d because they differ from those with reluctivity ν .

Similar to the case with the reluctivity ν , the basis vectors satisfy orthogonal relations based on the energy norms:

$$(\mathbf{e}_{2i}^d)^T \boldsymbol{\sigma} \mathbf{e}_{2j}^d = \delta_{ij} / R_{2i}^d, \quad (\mathbf{a}_{2i+1}^d)^T \mathbf{K}^d \mathbf{a}_{2j+1}^d = \delta_{ij} L_{2i+1}^d. \quad (3.22)$$

A similar derivation of the nonlinear state equations can also be performed based on the differential reluctivity as follows. Substituting (3.17) and (3.18) into

(3.15) and (3.16) derives

$$\mathbf{K}^d \sum_{n=0}^{N_s-1} I_{2n+1} \mathbf{a}_{2n+1}^d = \boldsymbol{\sigma} \sum_{n=0}^{N_s-1} V_{2n} \mathbf{e}_{2n}^d, \quad (3.23)$$

$$\mathbf{K}^d \sum_{n=0}^{N_s-1} V_{2n} \mathbf{e}_{2n}^d = -\frac{d}{dt} \left(\sum_{n=0}^{N_s-1} I_{2n+1} \mathbf{K}^d \mathbf{a}_{2n+1}^d \right). \quad (3.24)$$

From (3.20), (3.22), and (3.23), the following relation is obtained:

$$-I_{2k+1} = \frac{V_{2k+2}}{R_{2k+2}^d} - \frac{V_{2k}}{R_{2k}^d}. \quad (k = 0, 1, \dots, N_s - 1) \quad (3.25)$$

Transforming (3.24) and considering the initial conditions yield the following equation:

$$\begin{aligned} & \mathbf{K}^d \left(\sum_{n=0}^{N_s-1} V_{2n} \mathbf{e}_{2n}^d - V_S \mathbf{e}_0^d \right) \\ &= -\mathbf{K}^d \sum_{n=0}^{N_s-1} \mathbf{a}_{2n+1}^d \frac{dI_{2n+1}}{dt} - \sum_{n=0}^{N_s-1} I_{2n+1} \frac{d(\mathbf{K}^d \mathbf{a}_{2n+1}^d)}{dt}. \end{aligned} \quad (3.26)$$

Multiplying both sides of equation (3.26) by $(\mathbf{a}_{2k+1}^d - \mathbf{a}_{2k-1}^d)$ and using (3.19) and (3.22) lead to the following equations:

$$\begin{aligned} V_{2k} &= -(L_{2k+1}^d \frac{dI_{2k+1}}{dt} - L_{2k-1}^d \frac{dI_{2k-1}}{dt}) \\ &\quad - (\mathbf{a}_{2k+1}^d - \mathbf{a}_{2k-1}^d)^T \sum_{n=0}^{N_s-1} I_{2n+1} \frac{d(\mathbf{K}^d \mathbf{a}_{2n+1}^d)}{d\alpha} \frac{d\alpha}{dt}, \quad (k = 1, 2, \dots, N_s - 1) \end{aligned} \quad (3.27)$$

$$V_0 = V_S - L_1^d \frac{dI_1}{dt} - (\mathbf{a}_1^d)^T \sum_{n=0}^{N_s-1} I_{2n+1} \frac{d(\mathbf{K}^d \mathbf{a}_{2n+1}^d)}{d\alpha} \frac{d\alpha}{dt}. \quad (3.28)$$

The last terms in (3.27) and (3.28) concerning $d(\mathbf{K}^d \mathbf{a}_{2n+1}^d)/d\alpha$ are the parameter variation terms. They can be prepared in the offline calculation.

If the parameter variation terms are negligible, (3.27) and (3.28) are approximated as

$$V_{2k} = -(L_{2k+1}^d \frac{dI_{2k+1}}{dt} - L_{2k-1}^d \frac{dI_{2k-1}}{dt}), \quad (k = 1, 2, \dots, N_s - 1) \quad (3.29)$$

$$V_0 = V_S - L_1^d \frac{dI_1}{dt}. \quad (3.30)$$

Equations (3.25), (3.29), and (3.30) correspond to the nonlinear Cauer network equations examined by [31].

3.2 Network Equations Using the Magnetic Flux as a Variable

The state equations derived in the previous subsections are not the circuit equations of the CLN because they include parameter variation terms. In contrast, when the magnetic flux is used as a variable, the circuit equations of the CLN are represented as

$$V_{2k} = \frac{d\Phi_{2k-1}}{dt} - \frac{d\Phi_{2k+1}}{dt}, \quad (k = 1, \dots, N_s - 1) \quad (3.31)$$

$$V_0 = V_s - \frac{d\Phi_1}{dt}, \quad (3.32)$$

where Φ_{2k-1} is the magnetic flux that flows through the k -th inductor.

Equations (3.31) and (3.32) are transformed into

$$V_{2k} = \frac{d(L_{2k-1}I_{2k-1})}{dt} - \frac{d(L_{2k+1}I_{2k+1})}{dt}, \quad (k = 1, \dots, N_s - 1) \quad (3.33)$$

$$V_0 = V_s - \frac{d(L_1I_1)}{dt}, \quad (3.34)$$

where the inductance is defined as $L_{2k-1} = \Phi_{2k-1}/I_{2k-1}$. Equations (3.33) and (3.34) directly express the time variance of the nonlinear inductors and may have the same effect as the parameter variation terms.

Equations (3.31) and (3.32) can also be transformed using the differential inductance $L_{2k-1}^d = d\Phi_{2k-1}/dI_{2k-1}$ as

$$\begin{aligned} V_{2k} &= \frac{d\Phi_{2k-1}}{dI_{2k-1}} \frac{dI_{2k-1}}{dt} - \frac{d\Phi_{2k+1}}{dI_{2k+1}} \frac{dI_{2k+1}}{dt}, \quad (k = 1, \dots, N_s - 1) \\ &= L_{2k-1}^d \frac{dI_{2k-1}}{dt} - L_{2k+1}^d \frac{dI_{2k+1}}{dt}, \quad (k = 1, \dots, N_s - 1) \end{aligned} \quad (3.35)$$

$$V_0 = V_s - L_1^d \frac{dI_1}{dt}, \quad (3.36)$$

which are identical to the state equations without the parameter variation terms (3.29) and (3.30).

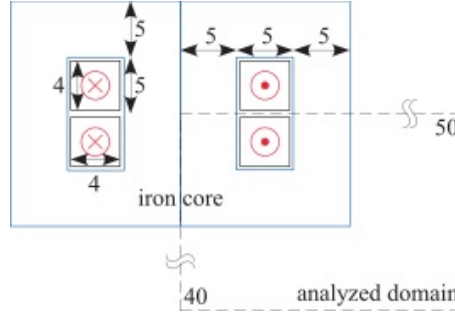


Figure 3.2: Iron-cored inductor with dimensions in millimeters.

3.3 Numerical Results

A 2D iron-cored inductor, shown in Fig. 3.2, was analyzed. The bulk material was assumed for the iron core. Only a quarter of the entire domain was calculated by the utilization of its line symmetry. The magnetic characteristics of the iron core are represented by the polynomial function

$$\mathbf{H} = \nu_i \left[h_1 \left(\frac{|\mathbf{B}|}{B_0} \right)^a + h_2 \right] \mathbf{B}, \quad (3.37)$$

where $\nu_i = (1/4\pi) \times 10^3$ m/H, $h_1 = 2$, $h_2 = 1$, $B_0 = 1$ T, and $a = 6$. The reluctivity $\nu(\mathbf{B})$ and differential reluctivity $\nu^d(\mathbf{B})$ are derived as follows:

$$\nu(\mathbf{B}) = \nu_i \left[h_1 \left(\frac{|\mathbf{B}|}{B_0} \right)^a + h_2 \right], \quad (3.38)$$

$$\nu^d(\mathbf{B}) = \frac{\partial \mathbf{H}}{\partial \mathbf{B}} = \nu_i \left[h_1 \left(\frac{|\mathbf{B}|}{B_0} \right)^a + h_2 \right] \mathbf{1} + \nu_i a h_1 \left(\frac{|\mathbf{B}|}{B_0} \right)^{a-2} \frac{\mathbf{B}\mathbf{B}^T}{B_0^2}, \quad (3.39)$$

where $\mathbf{1}$ is a unit matrix.

The B–H characteristics of the iron core, represented by (3.37), are shown in Fig. 3.3. The conductivity of the iron core was 1.0×10^6 S/m, whereas the reluctivity and conductivity of the coil were $(1/4\pi) \times 10^7$ m/H and 4.0×10^6 S/m, respectively.

3.3.1 Offline Calculation

Preparation of the Network Elements The network elements R , L , R^d , and L^d were calculated along with several parameter variation terms in the offline calculation. They were obtained for $\alpha = I_1 = 0$ –200 A with intervals of 0.1 A.

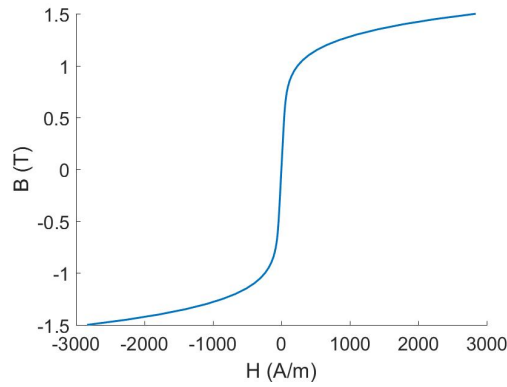


Figure 3.3: B–H characteristics of the iron core assumed in the simulation.

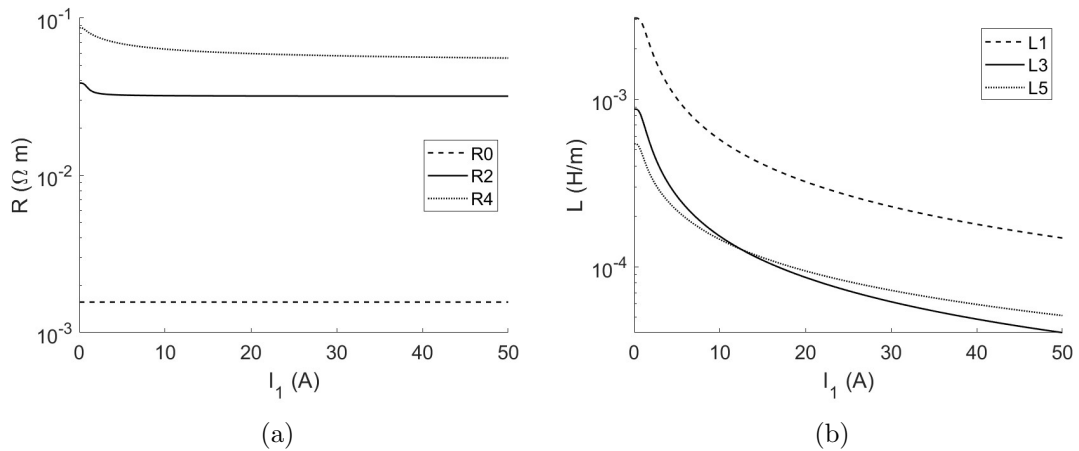


Figure 3.4: Result of (a) R_{2n} and (b) L_{2n+1} using ν .

Fig. 3.4 shows the variations in R_{2n} and L_{2n+1} ($n = 0, 1, 2$) based on the reluctivity ν for $I_1 = 0\text{--}50$ A. The inductance L_{2n+1} decreased as I_1 increased owing to magnetic saturation. L_1 was larger than L_{2n+1} ($n > 0$).

The variations in R_{2n}^d and L_{2n+1}^d ($n = 0, 1, 2$) based on the differential reluctivity ν^d are shown in Fig. 3.5 for $I_1 = 0\text{--}50$ A. Tendencies similar to those of R_{2n} and L_{2n+1} were observed, except for the slope of L_{2n+1}^d against I_1 , which was steeper than that of L_{2n+1} .

Preparation of the Parameter Variation Term A part of the parameter variation terms was also prepared in the offline calculation. The $d\mathbf{a}_{2n-1}/dI_1$ part in the parameter variation terms was obtained by calculating the central difference of \mathbf{a}_{2n-1} regarding I_1 . The results of $\mathbf{a}_{2k-1}^T \mathbf{K} d\mathbf{a}_{2n-1}/dI_1$ are shown in Fig. 3.6 for $(k, n) = (1, 1), (1, 3), (3, 1),$ and $(3, 3)$. The dominance of component $(k, n) =$

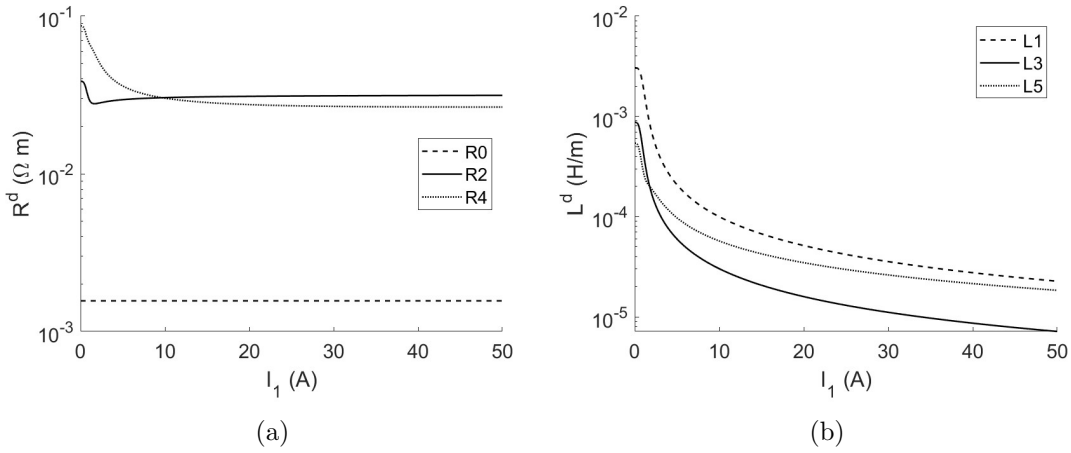


Figure 3.5: Results of (a) R_{2n}^d and (b) L_{2n+1}^d using ν^d .

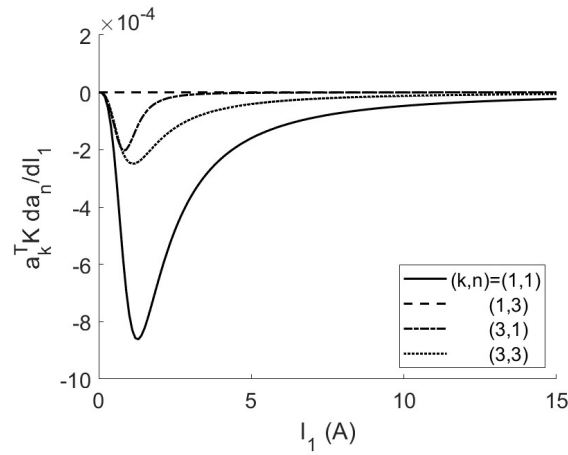


Figure 3.6: Result of $\mathbf{a}_{2k-1}^T \mathbf{K} d\mathbf{a}_{2n-1} / dI_1$ using ν .

(1,1) was observed. The components with $k \neq n$ were small. In particular, $(k, n) = (1, 3)$ remained almost zero for all I_1 values.

When the differential reluctivity ν^d was used, $(\mathbf{a}_{2k-1}^d)^T d(\mathbf{K}^d \mathbf{a}_{2n-1}^d) / dI_1$ was prepared using the central difference scheme regarding I_1 , as shown in Fig. 3.7 for $(k, n) = (1, 1)$, $(1, 3)$, $(3, 1)$, and $(3, 3)$. Unlike the result based on the reluctivity ν , the component $(k, n) = (1, 1)$ was small, whereas the $(k, n) = (1, 3)$ term was dominant.

By combining the results in Figs. 3.4 and 3.6, $L_1 + I_1 \mathbf{a}_1^T \mathbf{K} d\mathbf{a}_1 / dI_1$ was obtained as plotted in the solid line in Fig. 3.8, and L_1 is also shown in this figure for comparison. As I_1 increased, the solid line moved farther from the dashed line, which indicates that the parameter variation terms have a significant influence on the inductance.

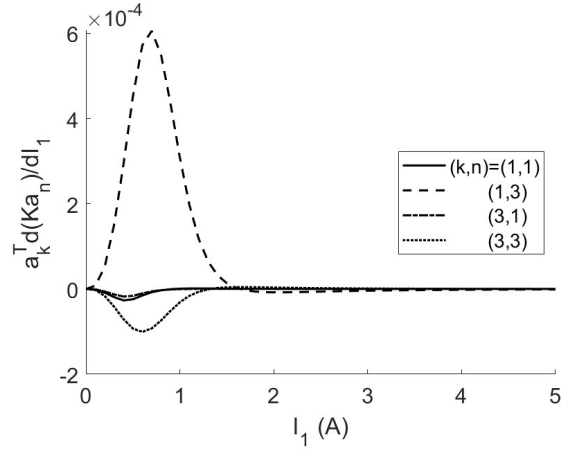


Figure 3.7: Result of $(\mathbf{a}_{2k-1}^d)^T d(\mathbf{K}^d \mathbf{a}_{2n-1}^d)/dI_1$ using ν^d .

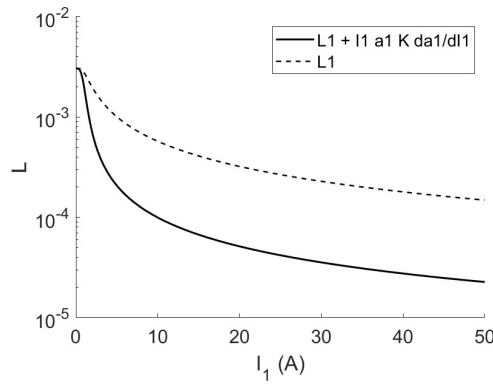


Figure 3.8: Results of L_1 and $L_1 + I_1 \mathbf{a}_1^T \mathbf{K} d\mathbf{a}_1/dI_1$ using ν .

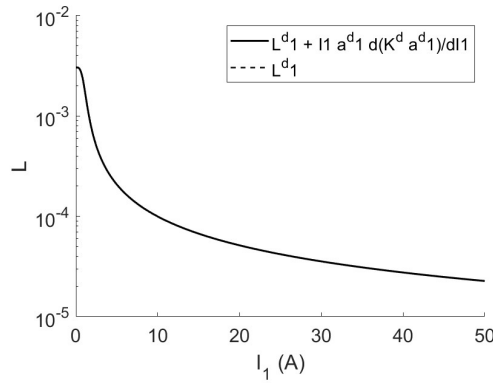


Figure 3.9: Results of L_1^d and $L_1^d + I_1 (\mathbf{a}_1^d)^T d(\mathbf{K}^d \mathbf{a}_1^d)/dI_1$.

The corresponding result based on differential reluctivity ν^d is shown in Fig. 3.9. The term $L_1^d + I_1 (\mathbf{a}_1^d)^T d(\mathbf{K}^d \mathbf{a}_1^d)/dI_1$ is plotted using the solid line, which is almost identical to the dashed line showing L_1^d . The influence of the parameter variation term was expected to be negligible.

3.3.2 Online Calculation

The output current was derived by solving the state equations with the prepared parameters in the online calculation. A sinusoidal electric field E_S with an amplitude of 0.3 V/m and frequency $f = 5$ Hz was applied to the coil. When $B = 0$ and $f = 5$ Hz, the skin depth was $\sqrt{2\nu_i/2\pi f\sigma_i} \approx 2.3$ mm. The frequency at which the skin depth was smaller than the thickness of the iron core (5 mm) was selected to observe the effect of eddy-current generation. The CLN used in the simulation consisted of five stages and was terminated with L_9 . A nonlinear transient analysis using the ordinary FEM, which directly solves (2.47), was also performed for comparison.

The resultant total current I_t (see Fig. 3.1) obtained with the reluctivity ν are shown in Fig. 3.10. The dots show the result of the FEM, whereas the lines are obtained by applying the CLN method. The dotted line (linear) is the result of the linear CLN, which differed significantly from the FEM result, as well as the dashed line (nonlinear 1) obtained using the nonlinear CLN neglecting the parameter variation terms. Both were calculated by solving the approximated state equations (3.9), (3.13), and (3.14), and the linear CLN used the circuit elements at $I_1 = 0$. In contrast, the solid line (nonlinear 2) obtained from the parameterized CLN, including the parameter variation terms calculated using (3.9), (3.11), and (3.12), was close to the FEM result.

Fig. 3.11 shows the results of the total current I_t when the differential reluctivity ν^d was used. The solid line (nonlinear d), which was calculated from the nonlinear CLN without the variation terms, reproduced the FEM result. This result indicated that the parameter variation terms could be neglected.

Fig. 3.12 shows the current I_{2n+1} ($n = 0, 1, 2$) flowing through each inductor L_{2n+1} for (a) nonlinear 1 and (b) nonlinear 2 based on the reluctivity ν . The current I_1 , which flowed through the first inductor L_1 , was the most dominant component in nonlinear 2, and it yielded a result similar to that of the FEM. Currents I_3 and I_5 appeared particularly when the total current was less than approximately 50 A. The FO approximation was not fully satisfied when $I_t < 50$ A; thus, the current did not agree very accurately with the FEM result for low current. Note that the applied frequency was high for the bulk-type iron core, as mentioned earlier; hence, the FO approximation was invalid owing to the generation of the eddy-current field.

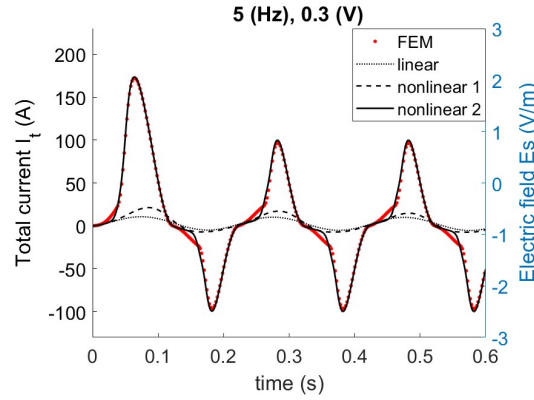


Figure 3.10: Transient waveform of the total current I_t obtained using the FEM, linear CLN method, and nonlinear CLN method with and without the parameter variation terms (nonlinear 1 and 2, respectively) when ν is used with $\alpha = I_1$. The applied electric field E_S is indicated as a blue solid line.

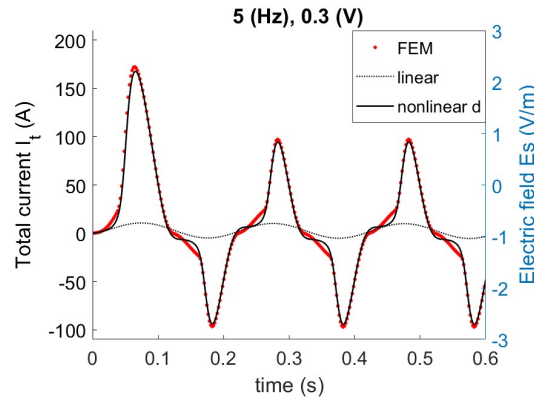


Figure 3.11: Transient waveform of the total current obtained using the FEM, linear CLN method, and nonlinear CLN method when ν^d is used with $\alpha = I_1$.

The following modifications can be effective for improving the representation accuracy in the low current range: (a) parameterizing not only with I_1 but also with I_3 , (b) using a total current $I_t (= \sum_n I_{2n+1})$ instead of I_1 as the parameter α when solving the state equations. The second method was observed to be effective in Ref. [31].

Fig. 3.13 shows the current I_{2n+1} ($n = 0, 1, 2$) flowing through each inductor L_{2n+1}^d for nonlinear d when the differential reluctivity ν^d was used. The current I_1 was dominant in the high current region, indicating the validity of using the FO approximation.

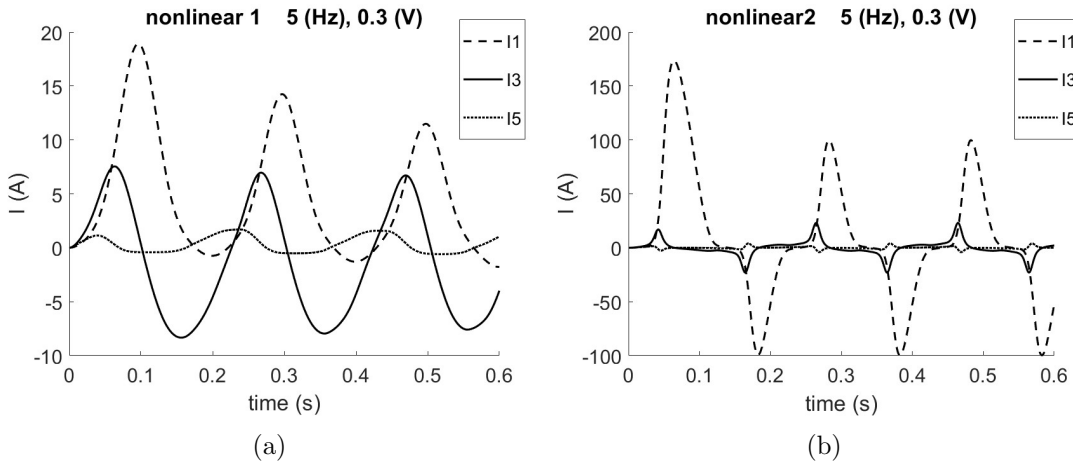


Figure 3.12: Computational results of currents flowing through each stage of the CLN when ν is used. The parameter variation terms are neglected in (a) nonlinear 1, whereas they are included in (b) nonlinear 2.

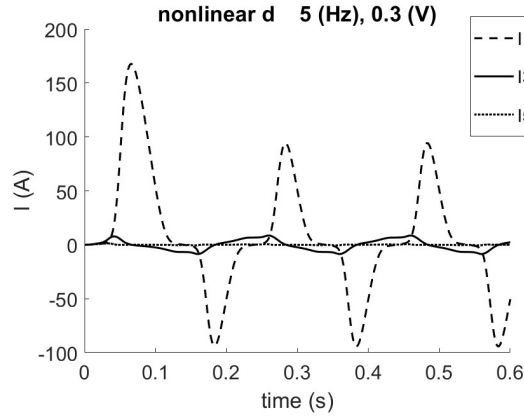


Figure 3.13: Currents flowing through each stage of the CLN when ν^d is used (nonlinear d).

3.3.3 Computation Time

As mentioned in 2.4.4, solving the linear systems in the FE space dominates the computation time of the FEM as well as the parameterized CLN. The Newton–Raphson (NR) method was used for the nonlinear solutions, and the analysis presented in this chapter required approximately four iterations on average for convergence in both the FE analysis and CLN method.

Accordingly, the number of linear solutions required for the time-dependent nonlinear FE simulation was $4N_t$, where N_t is the number of time steps.

In contrast, the offline calculation of the five-stage CLN required one nonlinear solution for the first stage to obtain L_1 , and four linear solutions for the

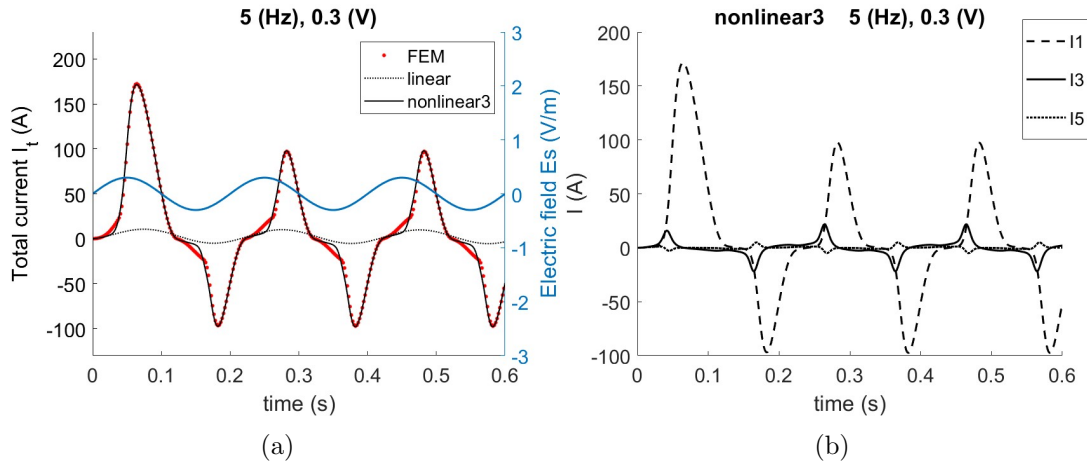


Figure 3.14: (a) Transient waveform of the total current obtained using the FEM, linear CLN method, and nonlinear CLN method where the network equation is directly derived from the CLN. (b) Currents flowing through each stage.

remaining stages (L_3 to L_9) per parameter; therefore, approximately eight linear solutions were performed per parameter. Let N_α be the number of parameter values; the number of linear solutions required in the offline computation in total was approximately $8N_\alpha$. Assuming that the computational cost for the online computation was negligible, the CLN method was faster than the FEM when $N_t > 2N_\alpha$ was satisfied (see Fig. 2.5).

The parameterized CLN significantly reduces the computation time when a large number of time steps and/or conditions must be tested.

3.3.4 Solution of Network Equations Using Magnetic Flux as a Variable

The solid line (nonlinear 3) shown in Fig. 3.14(a) is the total current computed from the network equation (3.33), which employs the magnetic flux as a variable. The resultant current agreed with that of FEM. This result demonstrated that the equation can account for parameter variation by incorporating the time variation of inductance, instead of using the parameter variation terms. The current flowing through each inductor is shown in Fig. 3.14(b).

3.4 Summary

A parameterized CLN method is formulated to include magnetic saturation, where the dynamic behavior of an orthogonal basis is represented by the parameter variation terms. The terms are newly derived by an exact formulation of the parameterized CLN. The parameter variation terms play a significant role in the state equations when the reluctivity ν is used, whereas they can be neglected when the differential reluctivity ν^d is used. The computation time of nonlinear transient analyses can be reduced significantly by applying the parameterized CLN when the number of time steps is large.

Additionally, even when the reluctivity is used, the network equations using the magnetic flux as a variable sufficiently consider the parameter variation of the inductors. They are used in Chapter 6 to avoid the computation of parameter variation terms.

Chapter 4

Analysis of Induction Motors Using the Parameterized Multi-port CLN

This chapter discusses the application of the multi-port CLN method to motor analysis. Specifically, the multi-port CLN method is parameterized and applied to the nonlinear analysis of IMs.

For application to an IM, the multi-port CLN is used for the rotor domain to represent the eddy-current field in the rotor bars. As shown in Fig. 4.1, the stator and rotor networks are constructed separately and connected on the interface. Fig. 4.2 provides an overview of the IM analysis using the parameterized CLN method. The circuit construction does not require frequency or slip information.

The coefficients of the Fourier decomposition of the electromagnetic field are assigned as port variables between the stator and rotor, as stated in Section 4.1.1. Therefore, the required number of ports can be more than a hundred depending on the structure of the motor; using all port variables as the parameters is time-consuming and unrealistic to implement. Appropriate parameters must be selected to achieve both fast and accurate analysis. This point is described in detail in Section 4.1.3.

In the CLN analysis, a rotor network and a lookup table of the stator matrix and rotor are prepared beforehand in the offline calculation (the upper part of

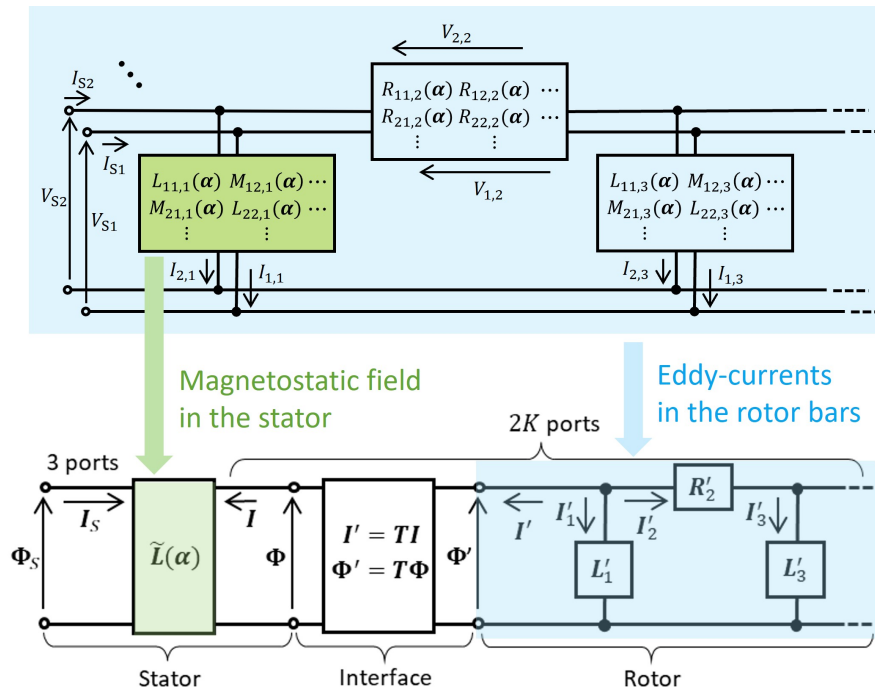


Figure 4.1: Network including the CLN for motor application.

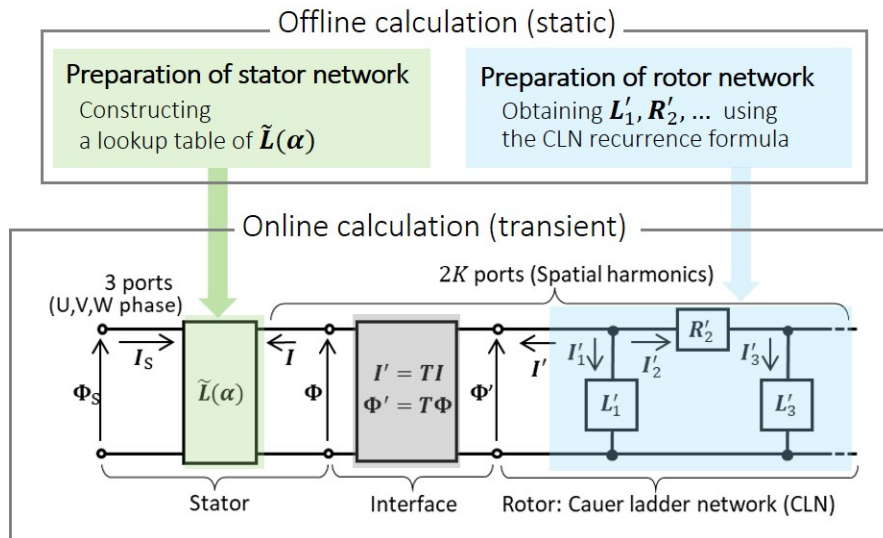


Figure 4.2: Overview of the motor analysis using the parameterized CLN method.

Fig. 4.2), and then the transient analysis is performed in the online calculation (the lower part of Fig. 4.2).

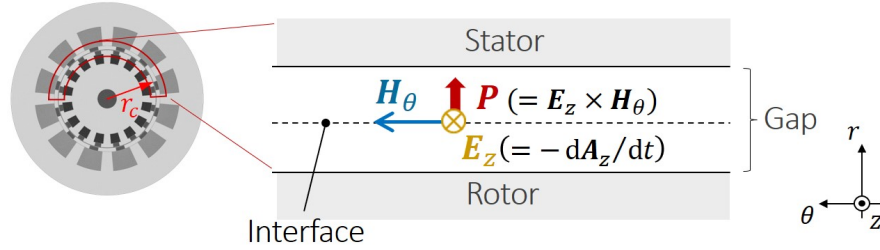


Figure 4.3: State variables on the interface \mathbf{I} and Φ are defined such that $\mathbf{I} \cdot d\Phi/dt$ represents the Poynting vector flowing through the interface.

4.1 Parameterized Motor CLN

4.1.1 Definition of State Vectors on the Interface

Vectors \mathbf{I} and Φ of the motor CLN (see the circuit in Fig. 4.2) are defined by the spatial harmonics of the circumferential magnetic field H_θ and the axial vector potential A_z on the interface. They represent the energy flow between the stator and rotor. The detailed definition is given below.

Let us assume that the electromagnetic fields of the stator and rotor at time t are represented as functions of (r, θ, z, t) and (r', θ', z', t') , respectively, where r , θ , and z are the radial, circumferential, and axial components, respectively, of the cylindrical coordinate. For simplicity, it is assumed that the electromagnetic fields are uniform along z . The relations between the stator and rotor coordinates are

$$r' = r, \quad \theta' = \theta - \omega_R t, \quad z' = z, \quad t' = t, \quad (4.1)$$

where ω_R is the mechanical angular frequency, and the relationship between ω_R and synchronous angular frequency ω_s is $\omega_R = (1 - s)\omega_s/p$, where s and p are the slip and number of pole pairs, respectively.

State variables are defined to represent the flow of the Poynting vector \mathbf{P} on the interface between the stator and rotor, as shown in Fig. 4.3. On the interface at a radius $r = r_c$, the partial differentiations satisfy the following relations:

$$\frac{\partial}{\partial \theta'} = \frac{\partial}{\partial \theta}, \quad \frac{\partial}{\partial t'} = \frac{\partial}{\partial t} + \omega_R \frac{\partial}{\partial \theta}. \quad (4.2)$$

The tangential field H_θ at the interface is given as the Neumann boundary condition in the FE formulation. Applying the Fourier expansion to H_θ [33] leads to

$$H_\theta(\theta, t) = \sqrt{2} \sum_k [H_{ck}(t) \cos(kp\theta) + H_{sk}(t) \sin(kp\theta)]. \quad (4.3)$$

The coefficients comprise the vector \mathbf{I} as

$$\mathbf{I} = [H_{c1}, H_{s1}, H_{c2}, H_{s2}, \dots, H_{cK}, H_{sK}]^T \in \mathbb{R}^{2K}. \quad (4.4)$$

The subscripts ck and sk denote the cosine and sine components of the k -th harmonics, respectively. The harmonic components are defined in the spatial period Θ_c , and those higher than the K -th harmonics are truncated. The expansion of the axial electric field E_z and vector potential A_z in the same manner defines \mathbf{V} and Φ as

$$\begin{aligned} \mathbf{V} &= -r_c \Theta_c l [E_{c1}, E_{s1}, E_{c2}, E_{s2}, \dots, E_{cK}, E_{sK}]^T, \\ \Phi &= r_c \Theta_c l [A_{c1}, A_{s1}, A_{c2}, A_{s2}, \dots, A_{cK}, A_{sK}]^T, \end{aligned} \quad (4.5)$$

where $\mathbf{V} = d\Phi/dt$ is satisfied. Here, l is the axial length of the analysis domain, and $r_c \Theta_c l$ corresponds to the area of the interface; it is multiplied such that $\mathbf{I} \cdot \mathbf{V}$ represents the total energy flowing through the interface in the analyzed domain.

A similar definition can be made on the rotor side interface. Coefficients obtained using the Fourier expansion of the field H'_θ , E'_z and A'_z on the rotor side interface comprise \mathbf{I}' , \mathbf{V}' and Φ' as follows.

$$\mathbf{I}' = [H'_{c1}, H'_{s1}, H'_{c2}, H'_{s2}, \dots, H'_{cK}, H'_{sK}]^T, \quad (4.6)$$

$$\mathbf{V}' = -r_c \Theta_c l [E'_{c1}, E'_{s1}, E'_{c2}, E'_{s2}, \dots, E'_{cK}, E'_{sK}]^T \quad (4.7)$$

$$\Phi' = r_c \Theta_c l [A'_{c1}, A'_{s1}, A'_{c2}, A'_{s2}, \dots, A'_{cK}, A'_{sK}]^T. \quad (4.8)$$

Boundary conditions $H'_\theta(\theta', t') = H_\theta(\theta, t)$ and $A'_z(\theta', t') = A_z(\theta, t)$ provide the relations

$$\mathbf{I}' = \mathbf{T}\mathbf{I}, \quad \Phi' = \mathbf{T}\Phi, \quad (4.9)$$

where

$$\mathbf{T} = \begin{bmatrix} \mathbf{T}_1 & & & O \\ & \mathbf{T}_2 & & \\ & & \ddots & \\ O & & & \mathbf{T}_K \end{bmatrix} \quad (4.10)$$

is a rotation matrix with

$$\mathbf{T}_k = \begin{bmatrix} \cos(kp \int \omega_R dt) & \sin(kp \int \omega_R dt) \\ -\sin(kp \int \omega_R dt) & \cos(kp \int \omega_R dt) \end{bmatrix}, \quad (4.11)$$

for $k = 1, 2, \dots, K$. The electromotive force in the rotor, generated by the slip, can be incorporated into the CLN using \mathbf{T} .

The connection between \mathbf{V} and \mathbf{V}' is calculated as

$$\begin{aligned} \mathbf{V}' &= \frac{d\Phi'}{dt} = \mathbf{T} \frac{d\Phi}{dt} + \frac{d\mathbf{T}}{dt} \Phi \\ &= \mathbf{T} (\mathbf{V} + r_c \omega_R \mathbf{B}), \end{aligned} \quad (4.12)$$

where \mathbf{B} is defined by the radial magnetic flux density $B_r = (1/r_c) \partial A_z / \partial \theta$ on the interface as

$$\mathbf{B} = p \Theta_c l [A_{s1}, -A_{c1}, 2A_{s2}, -2A_{c2}, \dots, KA_{sK}, -KA_{cK}]^T. \quad (4.13)$$

The term $r_c \omega_R \mathbf{T} \mathbf{B}$ in (4.12) corresponds to the motional electromotive force.

4.1.2 State Equations Solved in the Online Calculation

Stator The source current and magnetic flux with three-phase components are represented by $\mathbf{I}_s = [I_U, I_V, I_W]^T$ and $\Phi_s = [\Phi_U, \Phi_V, \Phi_W]^T$, respectively. The source voltage $\mathbf{V}_s = [V_U, V_V, V_W]^T$ can be derived using $\mathbf{V}_s = d\Phi_s/dt$.

For simplicity, it is assumed that the stator-winding resistance is not included in the CLN, and the iron-core conductivity is neglected. Accordingly, the stator-side CLN is represented by a single stage with a single inductance matrix. The stator equation is

$$\tilde{\Phi} = \tilde{\mathbf{L}} \tilde{\mathbf{I}}, \quad (4.14)$$

where

$$\tilde{\Phi} = \begin{bmatrix} \Phi_s \\ \Phi \end{bmatrix}, \quad \tilde{I} = \begin{bmatrix} I_s \\ I \end{bmatrix}, \quad \tilde{L} = \begin{bmatrix} L_{00} & L_{10}^T \\ L_{10} & L_{11} \end{bmatrix}. \quad (4.15)$$

Rotor The rotor network employs the CLN for expressing the eddy currents in the rotor bars. The state equations of the rotor CLN [33] are derived as follows:

$$\frac{d(\mathbf{L}'_{2n-1}\mathbf{I}'_{2n-1})}{dt'} - \frac{d(\mathbf{L}'_{2n+1}\mathbf{I}'_{2n+1})}{dt'} = \mathbf{R}'_{2n}\mathbf{I}'_{2n},$$

$$\mathbf{I}'_{2n} = -\mathbf{I}' - \mathbf{I}'_1 - \dots - \mathbf{I}'_{2n-1}, \quad (4.16)$$

where \mathbf{I}'_{2n-1} is the state vector of the current flowing through \mathbf{L}'_{2n-1} (see the rotor network in Fig. 4.2). The magnetic flux at the interface Φ' is equal to that through the first-stage inductance \mathbf{L}'_1 ; hence one obtains

$$\Phi' = \mathbf{L}'_1\mathbf{I}'_1. \quad (4.17)$$

Interface The substitution of (4.14) and (4.17) to the boundary condition (4.9) results in the equation of the interface:

$$\Phi = \mathbf{T}^{-1}\mathbf{L}'_1\mathbf{I}'_1 = \mathbf{L}_{10}\mathbf{I}_s + \mathbf{L}_{11}\mathbf{I}. \quad (4.18)$$

Solution of the State Equations The variables Φ_s , \mathbf{I} , and Φ at time t can be derived by solving (4.14) and (4.16) with the boundary condition (4.18) and a given source current \mathbf{I}_s . The total input power P_1 , air-gap power P_2 , and output electric torque τ are calculated as follows [33]:

$$P_1 = \mathbf{V}_s^T \mathbf{I}_s, \quad P_2 = -\mathbf{V}^T \mathbf{I}, \quad \tau = r_c \mathbf{I}^T \mathbf{B}. \quad (4.19)$$

4.1.3 Parameterization of the Multi-port Network

By introducing the concept of parameterization to multi-port CLNs, this thesis aims to conduct eddy-current simulations of a rotating induction motor reflecting the magnetic saturation. A parameter vector α consisting of multiple parameters is employed to represent the nonlinearity of multi-port CLN.

Because the number of ports is large, using all the multiple-port variables as parameters requires significant computational costs. An appropriate parameter set must be selected to achieve fast and accurate analyses. The parameter selection is described below.

Parameterization of the Stator Inductance For simplicity, only the stator network is parameterized in the following, but the same procedure can be applied to the rotor CLN. The stator inductance matrix is parameterized as

$$\tilde{\Phi} = \begin{bmatrix} \mathbf{L}_{00}(\boldsymbol{\alpha}) & \mathbf{L}_{10}^T(\boldsymbol{\alpha}) \\ \mathbf{L}_{10}(\boldsymbol{\alpha}) & \mathbf{L}_{11}(\boldsymbol{\alpha}) \end{bmatrix} \tilde{\mathbf{I}} = \tilde{\mathbf{L}}(\boldsymbol{\alpha})\tilde{\mathbf{I}}, \quad (4.20)$$

where the inductance matrix $\tilde{\mathbf{L}}$ is a function of $\boldsymbol{\alpha}$.

Selection of Parameter Vectors for IM Analysis For the application of rotating IMs, a balanced three-phase current

$$\mathbf{I}_s = I_{\text{src}} \left[\cos \theta_{\text{src}}, \cos(\theta_{\text{src}} - \frac{2}{3}\pi), \cos(\theta_{\text{src}} - \frac{4}{3}\pi) \right]^T \quad (4.21)$$

is assumed, where I_{src} and θ_{src} are the current magnitude and phase angle, respectively. The simplest parameterization can be achieved using a parameter vector $\boldsymbol{\alpha}_1 = [I_{\text{src}}, \theta_{\text{src}}]$.

In the offline calculation, first, the reluctivity matrix $\boldsymbol{\nu}$ of the stator, which is a function of the magnetic flux density, is determined by imposing the current source (4.21) for various $\boldsymbol{\alpha}_1$ values. For simplicity, when $\boldsymbol{\nu}$ is determined, it is assumed that $\mathbf{I} = \mathbf{0}$, which corresponds to $H_\theta = 0$ on the interface. Subsequently, the stator inductance matrix is calculated using the determined $\boldsymbol{\nu}$ (the derivation is detailed in Section 4.1.4.) During the online calculation, the stator inductance at $\boldsymbol{\alpha}_1$ is obtained from a lookup table using spline interpolation.

However, when the rotor influence is significant ($\mathbf{I} \neq \mathbf{0}$), the source currents, and therefore $\boldsymbol{\alpha}_1$, do not directly represent the level of magnetic saturation. The magnetic field distribution inside the stator is more strongly associated with the magnetic fluxes at the source port or interface than the source currents. Hence, other parameter vectors $\boldsymbol{\alpha}_2 = [\Phi_{\text{coil}}, \theta_{\text{coil}}]$ and $\boldsymbol{\alpha}_3 = [\Phi_{\text{gap}}, \theta_{\text{gap}}]$ are proposed here, where $[\Phi_{\text{coil}}, \theta_{\text{coil}}]$ and $[\Phi_{\text{gap}}, \theta_{\text{gap}}]$ are the amplitude and phase angle of the coil flux

and gap flux, respectively, calculated as follows:

$$\Phi_{\text{coil}} = \sqrt{\frac{2}{3}(\Phi_U^2 + \Phi_V^2 + \Phi_W^2)}, \theta_{\text{coil}} = \tan^{-1} \left(\frac{\Phi_\beta}{\Phi_\alpha} \right), \quad (4.22)$$

$$\Phi_{\text{gap}} = \sqrt{(\Phi_{c1}^2 + \Phi_{s1}^2)}, \theta_{\text{gap}} = \tan^{-1} \left(\frac{\Phi_{s1}}{\Phi_{c1}} \right). \quad (4.23)$$

Here, $[\Phi_U, \Phi_V, \Phi_W]$ are components of Φ_s , and $[\Phi_{c1}, \Phi_{s1}]$ are the first two components of Φ . The variables Φ_α and Φ_β are amplitudes of magnetic flux of α and β phase, respectively. They are obtained from Φ_U , Φ_V , and Φ_W using Clarke transformation:

$$\begin{bmatrix} \Phi_\alpha \\ \Phi_\beta \end{bmatrix} = \sqrt{\frac{2}{3}} \begin{bmatrix} \cos 0 & \cos \frac{2}{3}\pi & \cos \frac{4}{3}\pi \\ \sin 0 & \sin \frac{2}{3}\pi & \sin \frac{4}{3}\pi \end{bmatrix} \begin{bmatrix} \Phi_U \\ \Phi_V \\ \Phi_W \end{bmatrix} \quad (4.24)$$

where $\Phi_U + \Phi_V + \Phi_W = 0$ is assumed.

In the offline calculation, a table containing the relation of α_2 and α_3 to α_1 was created from (4.20), (4.22), and (4.23) under the condition that $\mathbf{I} = \mathbf{0}$. During the online calculation, the stator inductance was determined using the inductance lookup table for α_2 or α_3 , where \mathbf{I} was not necessarily zero depending on the rotor condition.

4.1.4 Offline Calculations

Preparation of the Stator Inductance For the computation of $\tilde{\mathbf{L}}(\alpha_1)$, first, the nonlinear reluctivity matrix ν is determined by solving the magnetostatic equation

$$\mathbf{C}^T \nu(\mathbf{C}\mathbf{a}) \mathbf{C}\mathbf{a} = \mathbf{j}_s(\alpha_1). \quad (4.25)$$

Here, ν is a function of the magnetic flux density $\mathbf{C}\mathbf{a}$, and $\mathbf{j}_s(\alpha_1) \in \mathbb{R}^{N_e}$ is the current source density when $\mathbf{I}_s(\alpha_1)$ is given to the coils. Subsequently, \mathbf{a}_1 is derived with the determined ν by solving

$$\mathbf{C}^T \nu \mathbf{C}\mathbf{a}_1 = \mathbf{j}_{\text{unit}} = [\mathbf{j}_U, \mathbf{j}_V, \mathbf{j}_W, \mathbf{j}_{c1}, \mathbf{j}_{s1}, \mathbf{j}_{c2}, \mathbf{j}_{s2}, \dots, \mathbf{j}_{cK}, \mathbf{j}_{sK}], \quad (4.26)$$

where $\mathbf{j}_{\text{unit}} \in \mathbb{R}^{N_e \times (3+2K)}$ represents a unit source as introduced in (2.74). Vectors \mathbf{j}_U , \mathbf{j}_V , and \mathbf{j}_W represent current densities discretized in the FE space when a unit current is provided to U, V, and W ports, respectively. The boundary integration term (2.27) on the interface is represented by \mathbf{j}_{ck} and \mathbf{j}_{sk} ($k = 1, \dots, K$), which are the k -th harmonics of the circumferential magnetic field given as a unit source along the interface. Finally, $\tilde{\mathbf{L}}(\boldsymbol{\alpha}_1) = \mathbf{a}_1^T \mathbf{C}^T \boldsymbol{\nu} \mathbf{C} \mathbf{a}_1$ is obtained using \mathbf{a}_1 derived in (4.26).

The relation of $\boldsymbol{\alpha}_2$, $\boldsymbol{\alpha}_3$, and $\boldsymbol{\alpha}_1$ is also prepared in the offline calculation to transform the parameters of $\tilde{\mathbf{L}}(\boldsymbol{\alpha}_1)$, as explained in Section 4.1.3.

Preparation of the Rotor Network The rotor CLN consists of the inductance and resistance matrices $\mathbf{L}'_1, \mathbf{R}'_2, \mathbf{L}'_3, \dots$, which are obtained by solving the CLN recurrence formula (2.71) and (2.72) in the rotor domain of the FE space. The boundary integration term (2.27) on the interface is represented by \mathbf{j}_{ck} and \mathbf{j}_{sk} ($k = 1, \dots, K$) comprising $\mathbf{j}_{\text{unit}} = [\mathbf{j}_{c1}, \mathbf{j}_{s1}, \mathbf{j}_{c2}, \mathbf{j}_{s2}, \dots, \mathbf{j}_{cK}, \mathbf{j}_{sK}]$.

4.2 Numerical Results

The induction motor depicted in Fig. 4.4(a) was analyzed in the FE space. The stator had 12 slots and 2 pole pairs. The rotor consisted of an iron core and 16 rotor bars. The mesh generated in the FE field is shown in Fig. 4.4(b). Because the number of the rotor bars in half of the electrical cycle was an integer (4), the antiperiodic boundary condition should be satisfied for one electrical period; hence, the spatial period $\Theta_c = \pi/p$ was analyzed, and the even components, which canceled out with the boundary condition, were neglected in (4.4)–(4.8). The reluctivity of stator iron was given by (3.38) with the same coefficients used in Section 3.3. The iron in the rotor was assumed to have a linear property with reluctivity $(1/4\pi) \times 10^4$ m/H. The conductivity of the rotor bar was 4.0×10^7 S/m.

4.2.1 Offline Calculation of Stator Inductance

The lookup table of the stator inductance matrices was prepared for $I_{\text{src}} = 0\text{--}631$ AT (20 divisions in log scale) and $\theta_{\text{src}} = 0\text{--}\pi$ (24 divisions). Because the inductance did not change significantly in the saturated region, dividing the amplitude

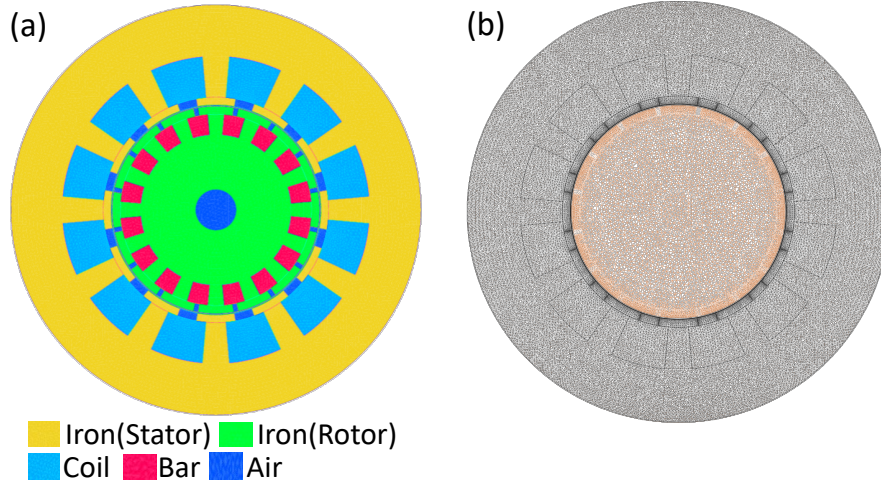


Figure 4.4: (a) Induction motor model, (b) mesh generated in the finite element space. The mesh for the stator and rotor domains is shown in different colors.

©2022 IEEE

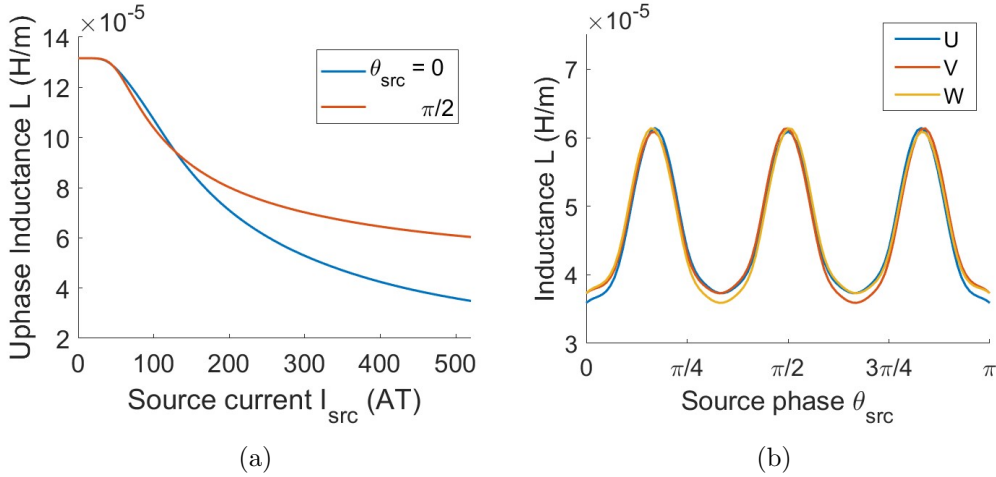


Figure 4.5: (a) U-phase diagonal component, and (b) three-phase diagonal components ($I_{src} = 500$ AT) of the inductance \mathbf{L}_{00} .

in the log scale reduced the number of parameter values without sacrificing the accuracy. Fig. 4.5 shows the stator inductance matrix \mathbf{L}_{00} , wherein the U-phase diagonal component with the source phase $\theta_{src} = 0$ and $\pi/2$ is shown in (a). The inductance decreased as the amplitude increased owing to the magnetic saturation. The difference in inductances between the two phases also resulted from the nonlinear magnetic characteristics; owing to the spatial distribution of the core material, the degree of saturation depends on the source phase. Fig. 4.5(b) shows the three-phase diagonal components with $I_{src} = 500$ AT. The inductance was minimal when the source phase corresponded to the center of the stator slots.

Fig. 4.6 depicts the relation between the state of the source current α_1 and

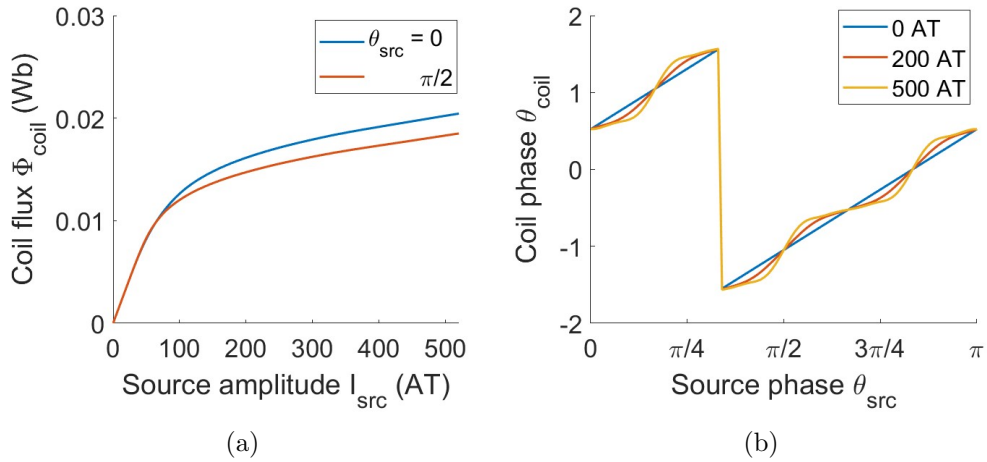


Figure 4.6: (a) The coil flux Φ_{coil} , and (b) the coil phase θ_{coil} .

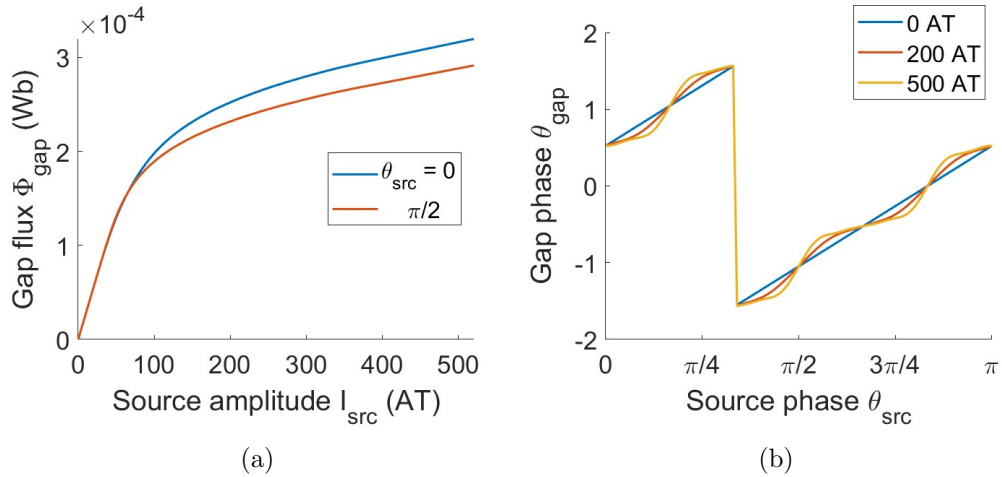


Figure 4.7: (a) The gap flux Φ_{gap} , and (b) the gap phase θ_{gap} .

coil flux α_2 obtained from (4.22). The coil flux in Fig. 4.6(a) clearly shows the effect of magnetic saturation. The difference between the source and coil flux phases in Fig. 4.6(b) is attributed to the stator structure.

Similar tendencies were observed with the gap flux α_3 . Fig. 4.7 shows the gap flux and phase, which were computed using (4.23).

4.2.2 Online Computation

As shown in Fig. 4.8, the source-current amplitude I_{src} increased from 0 to 500 AT in the first three cycles and remained constant for the last two cycles. The frequency was changed from 10 to 100 Hz, and the slip was varied from 0 to 1.

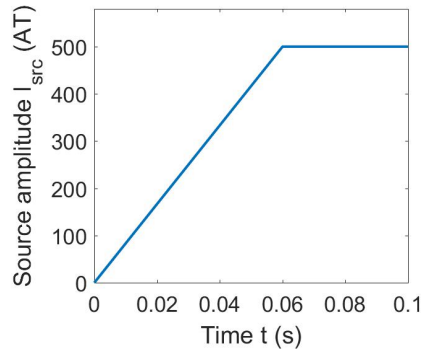


Figure 4.8: Amplitude of the input current I_{src} .

Identical circuit parameters were used for all conditions because the CLN can incorporate the change in rotation speed by modulating the matrix \mathbf{T} in (4.10).

Fig. 4.9 shows transient waveforms of (a) V-phase magnetic flux Φ_V , and (b) torque τ . The black solid line shows the results of the full-order FE analysis, whereas the dashed lines are those of the CLN. The results of the parameterized CLN agreed with those of the FE analyses when α_2 or α_3 was used as the parameters, as predicted in Section 4.1.3. Fig. 4.10 compares the averaged torque in the final cycle with various (a) slips and (b) frequencies. The nonlinear CLN parameterized by α_2 or α_3 yielded results close to those of the FE analysis.

4.2.3 Computation Time

As mentioned in Section 2.4.4, the linear solutions in the FE domain dominated the computation time in both FE and CLN analyses. The nonlinear equations were solved by iterating linear solutions using the NR method. The average number of iterations was 5.4 and 7.5 for the FE and CLN calculations, respectively. Hence, the transient FE analyses with N_t time-steps required $5.4N_t$ linear solutions.

In contrast, the online calculation time of the CLN method was negligible compared with that of the FEM (see Fig. 2.5). In the offline calculation, for each stator-CLN parameter, a single nonlinear solution was conducted to determine the reluctivity, and 35 linear solutions were executed to determine the inductance matrix (3 phase + 32 harmonic components). The rotor CLN with two stages required 32×2 linear solutions to derive \mathbf{R}' and \mathbf{L}' with 32 harmonic components. Therefore, $(7.5+35)N_\alpha+64$ linear solutions were required for the offline calculation.

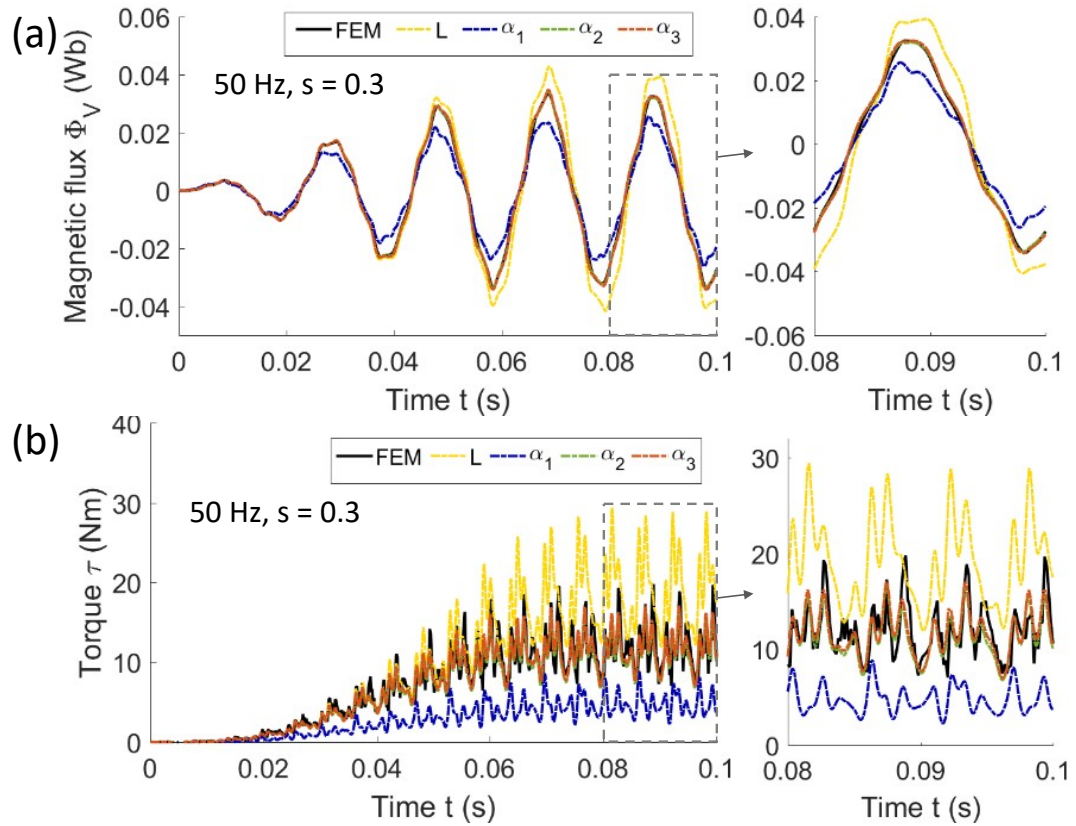


Figure 4.9: Transient waveforms of (a) V-phase magnetic flux, and (b) torque. They were obtained using the FEM, linear CLN (L), nonlinear CLN parameterized by the source current (α_1), coil flux (α_2), and gap flux (α_3). ©2022 IEEE

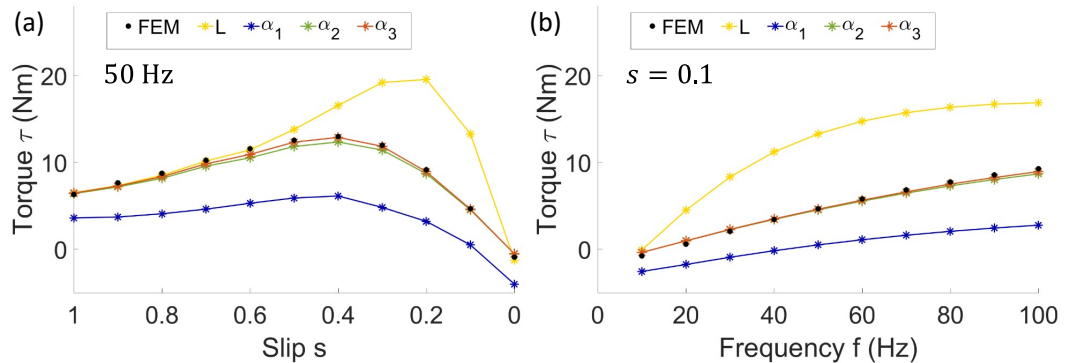


Figure 4.10: Torque averaged in the final cycle with various (a) slips, and (b) input frequencies. ©2022 IEEE

Because the degrees of freedom in the full FE analyses were more than that of the stator or rotor model individually computed in the CLN method, the speed-up ratio of the parameterized CLN to transient FE analyses was estimated to be more than $5.4N_t / (42.5N_\alpha + 64)$, which was 4.1 for calculating 20 operating points shown in Fig. 4.10. The number of parameter values and timesteps were $N_\alpha = 480$ and

$N_t = 3114$, respectively.

The speed-up ratio becomes particularly large for analyses with a large number of time steps, such as the evaluation of PWM input with high carrier frequencies, the generation of an efficiency map with various frequencies and slips, and coupled analyses with a control circuit.

4.3 Summary

The parameterized multi-port CLN method is developed and applied to an induction motor with nonlinear magnetic characteristics. When the amplitude and phase of either the coil or gap magnetic flux are used as the parameters, the developed method reproduces the transient waveforms obtained from full-order FE analysis with various slips and frequencies. In the presented example, the CLN method reduced the computation time by a factor of 4.1. The speed-up ratio further improves as the number of time steps increases.

Chapter 5

Analysis of Variable Reluctance Stepper Motors Using the Parameterized Multi-port CLN

In this chapter, the parameterized multi-port CLN method is applied to the analysis of a VR stepper motor. The reduced model represents the magnetic saturation of the stator and the effect of eddy currents in the rotor core. This chapter further shows that without any additional offline preparations, the CLN method can analyze the transient stepwise motion and step-out behavior, which should be studied to evaluate the control methods of VR stepper motors.

5.1 Parameterized CLN for a Stepper Motor

For the stepper motor analysis, the parameterized CLN method is used in almost the same manner as introduced in Chapter 4 (the overview is depicted in Fig. 4.2), except for the following two points:

- A one-phase-on operation by switching three current inputs is assumed instead of the three-phase balanced source. Consequently, a switching sequence is employed, instead of the source phase, as one of the parameters of the stator network.
- The equation of motion describing the load condition is simultaneously solved with the CLN during the online calculation to

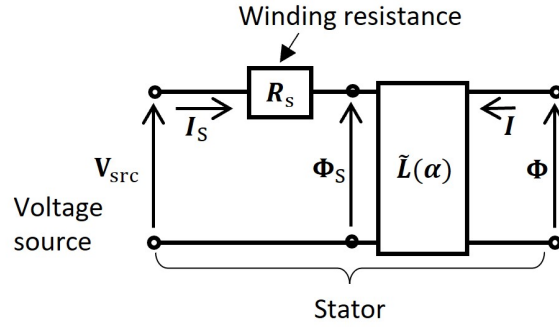


Figure 5.1: Stator network including the stator winding resistance R_s driven by a voltage source V_{src} .

analyze dynamical behavior such as stepping motions; mechanical analysis is coupled with the electromagnetic field analysis to satisfactorily address the dynamical behavior of the stepper motor.

These two points are detailed below.

5.1.1 Definition of Source Current and Parameters

Generally, VR stepper motors are driven by a voltage source. However, a current-source drive is assumed in the following description to simulate the motor behavior separately from the power supply. A drive with voltage source V_{src} can also be analyzed using the same parameterization method by adding the stator winding resistance R_s to the stator network as shown in Fig. 5.1.

The induction motor analysis in Chapter 4 assumed the three-phase balanced current source, whereas a one-phase-on operation by switching three current inputs

$$\mathbf{I}_s(\boldsymbol{\alpha}) = \begin{cases} [I_{src}, 0, 0]^T & (q = 1), \\ [0, I_{src}, 0]^T & (q = 2), \\ [0, 0, I_{src}]^T & (q = 3), \end{cases} \quad (5.1)$$

is assumed here, where $\boldsymbol{\alpha} = (I_{src}, q)$, I_{src} is the amplitude of the current source, and q is the input index. Although it is outside the scope of this study, a micro-step operation with any phase number can be handled by assigning the index q to the possible inputs.

As in the case with the IM analysis, for simplicity, it is assumed that the stator iron core is laminated, and its iron loss is negligible. Hence, the stator network comprises a single-stage nonlinear inductance $\tilde{\mathbf{L}}(\boldsymbol{\alpha})$, where $\boldsymbol{\alpha}$ is the parameter vector representing the nonlinear magnetic characteristics.

The result shown in Section 4.2.2 reveal that the preferred parameter to achieve high accuracy is either the magnetic flux interlinking the coils or the flux on the gap interface, but not the current source. Therefore, the parameter of $\tilde{\mathbf{L}}$ is transformed from $\boldsymbol{\alpha} = (I_{\text{src}}, q)$ to (Φ_{coil}, q) , where Φ_{coil} is the amplitude of the coil flux obtained using

$$\Phi_{\text{coil}} = \sqrt{\frac{2}{3}} \|\boldsymbol{\Phi}_s\|_2 = \sqrt{\frac{2}{3}} (\Phi_U^2 + \Phi_V^2 + \Phi_W^2). \quad (5.2)$$

In the offline preparation of $\mathbf{L}_{00}(\boldsymbol{\alpha})$, the relation between $\boldsymbol{\Phi}_s$ and \mathbf{I}_s is computed using $\boldsymbol{\Phi}_s = \mathbf{L}_{00}(\boldsymbol{\alpha})\mathbf{I}_s$, which is derived from (4.20) under the condition that $\mathbf{I} = \mathbf{0}$.

5.1.2 Coupling with the Equation of Motion

The equation of motion of the rotor

$$J \frac{d^2\theta_m}{dt^2} + D \frac{d\theta_m}{dt} = \tau - \tau_L \quad (5.3)$$

is solved at each timestep with the electromagnetic torque τ obtained in (4.19); τ_L and θ_m are the load torque and mechanical angle, respectively; J and D are the moment of inertia and friction coefficient, respectively, of the rotor and load.

5.2 Numerical Results

The concentrated-winding three-phase stepper motor, shown in Fig. 5.2, was analyzed. Although commercial VR stepper motors frequently have more than a few dozen teeth, a simple model with eight rotor teeth and four stator poles was used in this study. The current direction (+ or -) when the amplitude is positive and the corresponding magnetic polarities (N and S) of the U, V, and W phases are also indicated in Fig. 5.2.

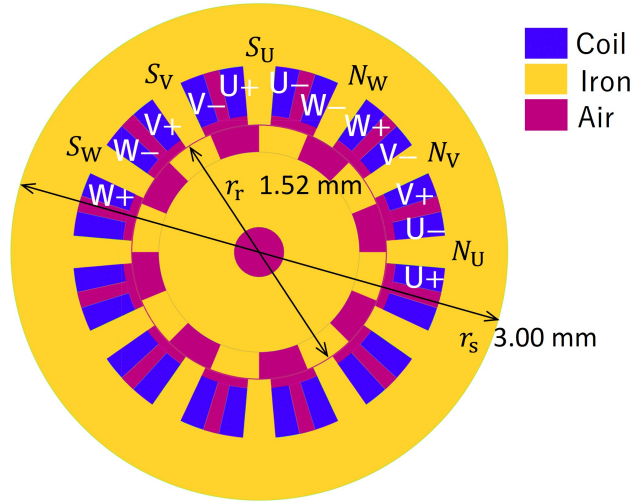


Figure 5.2: Configuration of the VR stepper motor model analyzed in this study.

©2022 IEEE

The same polynomial equation (3.38) was used to define the reluctivity of the stator iron core. The effect of eddy current was one of the targets of the study; hence, the rotor was assumed to be bulk iron with a constant reluctivity and conductivity of $(1/4\pi) \times 10^4$ m/H and 1.0×10^6 S/m, respectively.

The inertia J and friction coefficient D were 1.0×10^{-4} kg m² and 5.0×10^{-5} N m s, respectively. The initial rotor angle and speed were $-\pi/36$ rad and 0 rad/s, respectively. A fan-type load torque $\tau_L = b\Omega^3/|\Omega|$ N m was assumed, where $\Omega = d\theta_m/dt$ is the mechanical rotation speed.

The current inputs used in the simulation are shown in Fig. 5.3. From the configuration shown in Fig. 5.2, a continuous rotation in the counterclockwise direction was achieved by changing the index q in the sequence of $q = 1, 3, 2, 1, 3, 2, \dots$.

5.2.1 Offline Computation

Static offline calculations were conducted before the transient analyses. The CLN consisting of three stages was used for the rotor. Thirty-two harmonic components constituted the state vectors \mathbf{I} , \mathbf{I}' , Φ , and Φ' .

A lookup table of the stator inductance matrix $\tilde{\mathbf{L}}(\boldsymbol{\alpha})$ was created for three input indices ($q = 1, 2, 3$) and various amplitudes ($I_{\text{src}} = 0\text{--}301$ AT, 10 divisions in the log scale for 4.77–301 AT). As in the case of the IM, the amplitude was divided in a log scale to reduce the number of parameter values. Fig. 5.4(a)

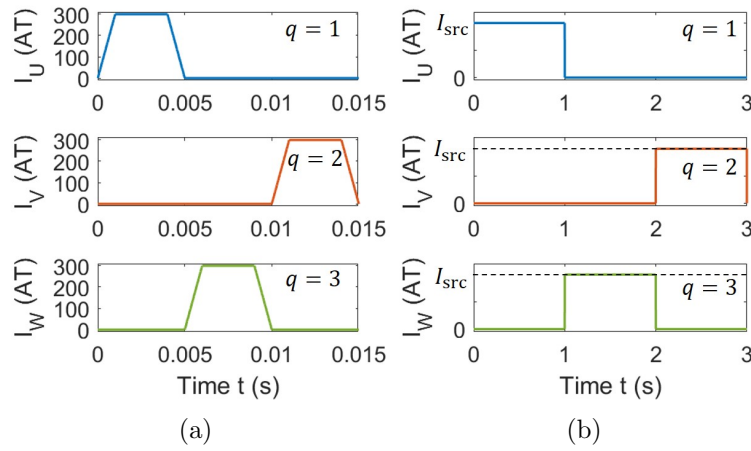


Figure 5.3: (a) Trapezoidal and (b) rectangular current inputs. ©2022 IEEE

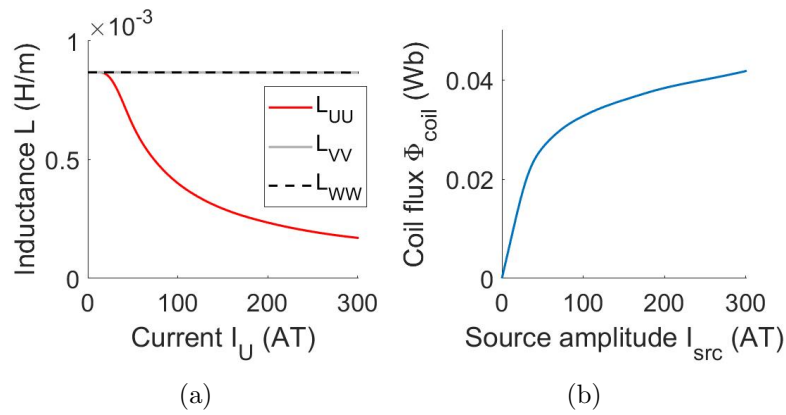


Figure 5.4: (a) Self-inductances L_{UU} , L_{VV} , and L_{WW} with $q = 1$. (b) Magnetic flux interlinking the coils. ©2022 IEEE

shows the U, V, and W-phase self-inductances, L_{UU} , L_{VV} , and L_{WW} , which are the diagonal components of $L_{00}(\boldsymbol{\alpha})$ in (4.20). The results are those with $q = 1$, where only the U-phase current I_U was supplied. The inductance L_{UU} decreased as I_U increased owing to the magnetic saturation. Conversely, L_{VV} and L_{WW} were almost constant; the effect of saturation was barely observed because of the salient structure of the stator teeth. Fig. 5.4(b) shows the Φ_{coil} derived from (5.2) when $q = 1$. The same curve was obtained for $q = 2$ and 3 owing to the symmetric structure of the stator.

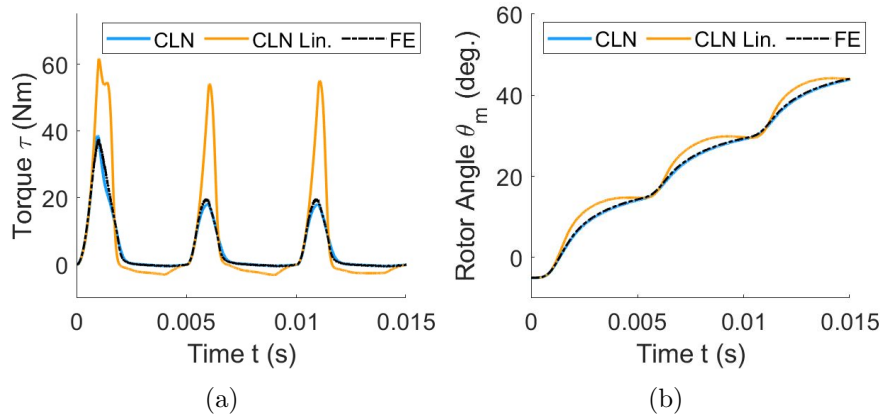


Figure 5.5: Time evolution of (a) electromagnetic torque and (b) rotor angle calculated using the parameterized CLN method (CLN), linear CLN (CLN Lin.), and FE analysis (FE). ©2022 IEEE

5.2.2 Online Computation

The stator and rotor network equations were solved using the equation of motion. The stator inductance matrix $\tilde{\mathbf{L}}(\Phi_{\text{coil}}, q)$ was determined using cubic spline interpolation.

Continuous Rotation First, continuous rotation was simulated with the current input shown in Fig. 5.3(a) to demonstrate that the CLN method can handle variable amplitudes. The coefficient of the load torque b was 1.0×10^{-3} . Figs. 5.5(a) and (b) show the electromagnetic torque τ and rotor angle θ_m , respectively, obtained using the parameterized CLN method (CLN), linear CLN method (CLN Lin.), and the FE analysis (FE). The results obtained using the parameterized CLN agreed closely with the FE analysis, whereas those by the linear CLN were inaccurate.

Stepwise Rotation and Step-out Motion Stepwise rotation, which is a characteristic operation of stepper motors, was simulated with a longer switching time. The current input with a constant switching time of 1 s and amplitude $I_{\text{src}} = 20$ AT (Fig. 5.3(b)) was assumed. A constant $b = 5.0 \times 10^{-4}$ was used for the coefficient of the load torque.

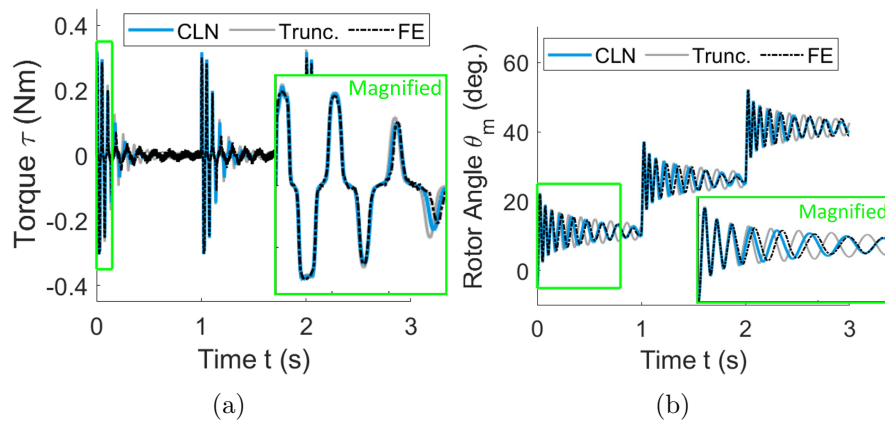


Figure 5.6: (a) Torque and (b) rotor angle of stepwise rotation. The results of the truncated network (Trunc.) are also shown. ©2022 IEEE

Fig. 5.6 shows the waveform of the torque and rotor angle. The figure also includes the results obtained using the truncated network (Trunc.) Its rotor network consisted of only L'_1 , which represents the magnetostatic field, and the effect of the eddy current was not included. In Fig. 5.6(a), a large instantaneous torque was observed after the input was switched. As shown in Fig. 5.6(b), the stepwise changes with oscillations were observed. The oscillation period of the CLN result agreed with the FE analysis better than the truncated network, which indicated that the CLN method can accurately simulate the effect of eddy current in the rotor.

The step-out behavior was also analyzed. A smaller load torque with $b = 2 \times 10^{-5}$ and lower amplitude $I_{src} = 5$ AT were employed for observing the step-out motion. The results until 2 s are shown in Fig. 5.7. The torque computed using the CLN and FE agreed well, as shown in Fig. 5.7(a). In Fig. 5.7(b), the stepwise motion was observed for the first sequence (0–1 s), where the rotor rotated by 15° . However, when the current input was switched at 1 s, the oscillation was sufficiently large to cause a step out, and the rotor angle transitioned in the negative direction. The CLN showed good agreement with the FE analysis, whereas the truncated network yielded an inaccurate result.

5.2.3 Evaluation of Computation Time

The time consumed in the online calculation of the CLN method was negligible compared with the solutions of equations in the FE space (see Fig. 2.5). The

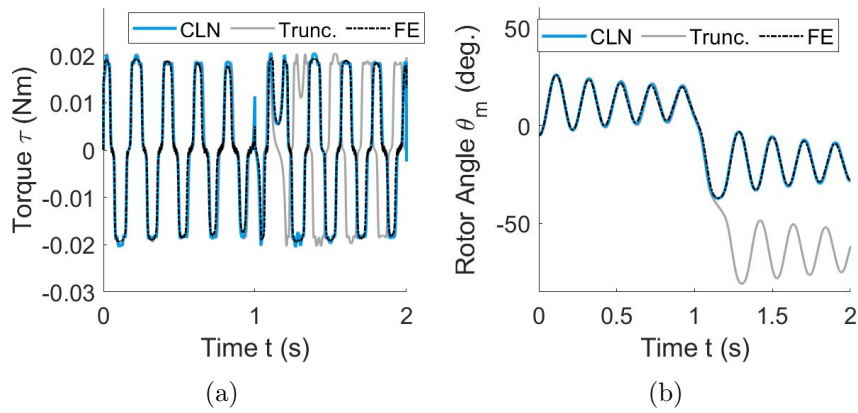


Figure 5.7: Time evolution of the (a) torque and (b) rotor angle when the load torque was small. A step-out motion was observed at $t = 1$ s. ©2022 IEEE

computation time of the FE and CLN methods should be evaluated by comparing the number of linear equations solved in the FE space.

The CLN method requires FE-space computations only for static offline calculations, and 1269 linear equations were solved, including iterations for solving nonlinear equations by the NR method. The NR method was also used in transient FE analyses, where the average number of iterations was 3.1 at each timestep. Therefore, the speed-up ratio of the CLN method to the FE analysis was $3.1N_t/1269 \approx N_t/409$, where N_t is the total number of timesteps. For the FE analyses shown in Figs. 5.5–5.7, N_t was 8000; hence, the speed-up ratio was 19.5. The ratio increases with a larger N_t , which means that the CLN method can be an effective tool for studying various operating conditions during the coupling analysis with a control system.

5.3 Summary

A nonlinear MOR of the VR stepper motor is constructed using the parameterized CLN method. The input index and amplitude of coil flux are used as the parameters. The electromagnetic analysis using the CLN method is coupled with solving the equation of motion. Its results agreed well with those of the FE analysis. The parameterized CLN method is applicable to stepwise rotation and step-out motion analyses without any additional offline preparations. The CLN method reduces the computation time by a factor of 19.5.

Chapter 6

Hysteretic Magnetic Field as a Nonlinear Problem

Empirical models of the magnetic hysteresis, such as Steinmetz's equation, are commonly employed for estimating the performance of electric machines. However, they have difficulty in accurately evaluating the minor hysteresis loops when the input waveform is distorted by PWM. Therefore, in FE analysis, the magnetic characteristics of the iron core should be given at each FE step using a precise hysteresis model; the problem with such analysis is that it can be extremely time-consuming.

This chapter is dedicated to reducing the computation time of electric-machine analysis considering the magnetic hysteresis characteristics. First, a semi-implicit (SI) method for FE analysis is proposed to speed up the FE analysis. In this chapter, the SI method is used to provide static hysteresis loops for modeling the inductor of the hysteretic CLN, as well as reference results of eddy-current analysis. Next, a hysteretic model order reduction method for electric machines is established using the parameterized single-port CLN method. The hysteresis effect is represented by the first inductor of CLN. The developed method is applied to the analysis of an iron-core inductor.

6.1 Semi-implicit Method for FE Analysis

The play model is selected for the modeling method of the magnetic hysteresis characteristics in this thesis because of its superiority to other methods, which is detailed in Appendix B. An implicit scheme is generally used to solve the hysteretic field equations in FE analysis to achieve numerical stability. The NR method is a widely employed iteration method; however, it can suffer from poor convergence owing to the discontinuous derivative of the hysteretic curve, particularly when the play model is used. Moreover, multiple iterations cost nonnegligible computation time. Instead of the NR method, the SI method is introduced in the following to update the magnetic field to avoid iterative computations in the FE analysis. The formulations introduced in this chapter are expected to apply to both 2D and 3D problems; 2D analysis results of an inductor are presented to validate the method.

6.1.1 SI Method for Transient Analysis

In the following, it is assumed that the analysis domain consists of multiple iron sheets. Because the divergence of the eddy currents flowing in each sheet must be zero, the scalar potential must be used as a variable. It is further assumed that the model is uniform in z direction, and the source current or voltage is imposed in the z direction; the 2D analysis in the x - y plane is discussed below because of the uniformity of electromagnetic field in the z direction.

Let the number of iron sheets be N_L , and ϕ_k ($k = 1, 2, \dots, N_L$) be the scalar potential at the k -th sheet. The gradient of the scalar potential $e_{z,k} (= \partial\phi_k/\partial z)$ can be assumed to be constant at each sheet. The weak form of the eddy-current equations (2.41) and (2.42) are represented as follows:

$$\mathbf{C}^T \boldsymbol{\nu} \mathbf{C} \mathbf{a} + \sigma \frac{d\mathbf{a}}{dt} + \mathbf{S} \mathbf{e}_z = \mathbf{j}_s, \quad (6.1)$$

$$\mathbf{S}^T \frac{d\mathbf{a}}{dt} + \mathbf{P} \mathbf{e}_z = \mathbf{0}, \quad (6.2)$$

where $\mathbf{e}_z = [e_{z,1}, \dots, e_{z,N_L}]^T$, and

$$\mathbf{S} = \{S_{ik}\} \in \mathbb{R}^{N_e \times N_L}, \quad S_{ik} = \int_{\Omega_k} \sigma \mathbf{w}_i^e d\Omega, \quad (6.3)$$

$$\mathbf{P} = \text{diag}(P_{11}, P_{22}, \dots, P_{N_L N_L}) \in \mathbb{R}^{N_L \times N_L}, \quad P_{kk} = \int_{\Omega_k} \sigma d\Omega. \quad (6.4)$$

The time evolution of (6.1) and (6.2) can be solved using the implicit Euler time-stepping scheme:

$$\begin{bmatrix} \frac{\sigma}{\Delta t} & \mathbf{S} \\ \mathbf{S}^T & \Delta t \mathbf{P} \end{bmatrix} \mathbf{y}_{m+1} = \begin{bmatrix} -\mathbf{C}^T \mathbf{h}_{m+1} + \frac{\sigma \mathbf{a}_m}{\Delta t} + \mathbf{j}_{m+1} \\ \mathbf{S}^T \mathbf{a}_m \end{bmatrix}, \quad (6.5)$$

where

$$\mathbf{y}_m = \begin{bmatrix} \mathbf{a}_m \\ \mathbf{e}_{z,m} \end{bmatrix}. \quad (6.6)$$

A variable vector with the subscript m denotes a vector of the m -th time step. The magnetic field vector \mathbf{h}_{m+1} is determined from the magnetic flux density vector $\mathbf{b}_{m+1} = \mathbf{C} \mathbf{a}_{m+1}$ based on the hysteretic magnetic characteristics of the material. In this setting, the vector play model [39] is used to determine \mathbf{h} at each finite element. A brief introduction to the vector play model is presented in Appendix B.3.

The NR method frequently exhibits poor convergence in FE analysis when the differential reluctivity matrix $\boldsymbol{\nu}_m^d = \boldsymbol{\nu}^d(\mathbf{b}_m)$ is discontinuous. To solve this problem, a linear approximation of the magnetic field

$$\mathbf{h}_{m+1} \approx \mathbf{h}_m + \boldsymbol{\nu}_m^d (\mathbf{b}_{m+1} - \mathbf{b}_m) \quad (6.7)$$

is introduced here. By substituting (6.7) into (6.5), the following SI formulation is obtained:

$$\begin{bmatrix} \frac{\sigma}{\Delta t} + \mathbf{K}^d & \mathbf{S} \\ \mathbf{S}^T & \Delta t \mathbf{P} \end{bmatrix} \mathbf{y}_{m+1} = \begin{bmatrix} -\mathbf{C}^T \mathbf{h}_m + (\mathbf{K}^d + \frac{\sigma}{\Delta t}) \mathbf{a}_m + \mathbf{j}_{m+1} \\ \mathbf{S}^T \mathbf{a}_m \end{bmatrix}, \quad (6.8)$$

which is a linear equation for \mathbf{y}_{m+1} .

6.1.2 Combination With the Predictor–Corrector Scheme

As (6.8) employs a linear approximation, its accuracy is expected to be insufficient; the predictor–corrector (PC) scheme can be introduced to improve and evaluate the accuracy. The PC scheme is a multi-step algorithm conventionally employed for solving ordinary differential equations; first, an integration is executed to obtain

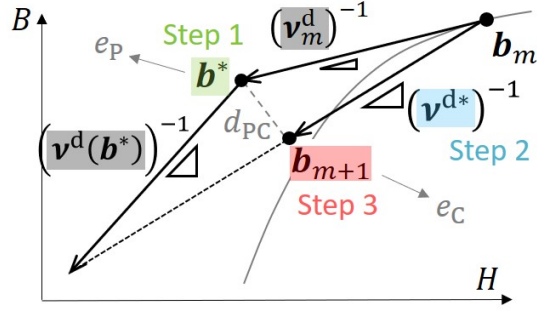


Figure 6.1: Procedure of the SI method combined with the PC scheme.

a prediction, based on which a nonlinear function is updated, and then a more accurate solution is obtained.

A three-step procedure is proposed here, as shown in Fig. 6.1, for combining the PC scheme with the SI method. Detailed descriptions are provided below.

Step 1: The prediction of \mathbf{y} at the $(m + 1)$ -th time step is derived from (6.8) as a predictor $\mathbf{y}^* = [\mathbf{a}^{*\text{T}}, \mathbf{e}_z^{*\text{T}}]^\text{T}$:

$$\begin{bmatrix} \frac{\sigma}{\Delta t} + \mathbf{K}^{\text{d}} & \mathbf{S} \\ \mathbf{S}^\text{T} & \Delta t \mathbf{P} \end{bmatrix} \mathbf{y}^* = \begin{bmatrix} -\mathbf{C}^\text{T} \mathbf{h}_m + (\mathbf{K}^{\text{d}} + \frac{\sigma}{\Delta t}) \mathbf{a}_m + \mathbf{j}_{m+1} \\ \mathbf{S}^\text{T} \mathbf{a}_m \end{bmatrix}, \quad (6.9)$$

Step 2: ν_{d} is corrected based on the predictor as

$$\nu^{\text{d}*} = 0.5 \times (\nu_m^{\text{d}} + \nu^{\text{d}}(\mathbf{b}^*)), \quad (6.10)$$

where $\mathbf{b}^* = \mathbf{C} \mathbf{a}^*$.

Step 3: Equation (6.8) is solved again using the updated reluctivity $\nu^{\text{d}*}$ as

$$\begin{bmatrix} \frac{\sigma}{\Delta t} + \mathbf{K}^{\text{d}*} & \mathbf{S} \\ \mathbf{S}^\text{T} & \Delta t \mathbf{P} \end{bmatrix} \mathbf{y}_{m+1} = \begin{bmatrix} -\mathbf{C}^\text{T} \mathbf{h}_m + (\mathbf{K}^{\text{d}*} + \frac{\sigma}{\Delta t}) \mathbf{a}_m + \mathbf{j}_{m+1} \\ \mathbf{S}^\text{T} \mathbf{a}_m \end{bmatrix}, \quad (6.11)$$

where $\mathbf{K}^{\text{d}*} = \mathbf{C}^\text{T} \nu_{\text{d}}^* \mathbf{C}$. The solution to (6.11) is defined as the corrector.

6.1.3 SI Method for Static Analysis

The SI method can also be applied to static problems; instead of (6.5), the following magnetostatic equation is solved:

$$\begin{bmatrix} O & \mathbf{S} \\ O & \mathbf{P} \end{bmatrix} \mathbf{y}_{m+1} = \begin{bmatrix} -\mathbf{C}^T \mathbf{h}_{m+1} + \mathbf{j}_{m+1} \\ \mathbf{0} \end{bmatrix}, \quad (6.12)$$

from which $\mathbf{e}_{z,m+1} = \mathbf{0}$ is obtained. Equation (6.12) is further simplified to

$$\mathbf{S} \mathbf{a}_{m+1} = -\mathbf{C}^T \mathbf{h}_{m+1} + \mathbf{j}_{m+1}. \quad (6.13)$$

The predictor and corrector of the static analysis are obtained as

$$\mathbf{K}^d \mathbf{a}^* = -\mathbf{C}^T \mathbf{h}_m + \mathbf{K}^d \mathbf{a}_m + \mathbf{j}_{m+1}, \quad (6.14)$$

$$\mathbf{K}^{d*} \mathbf{a}_{m+1} = -\mathbf{C}^T \mathbf{h}_m + \mathbf{K}^{d*} \mathbf{a}_m + \mathbf{j}_{m+1}, \quad (6.15)$$

instead of (6.9) and (6.11), respectively.

6.1.4 Numerical Results

The 2D laminated iron-core inductor model used in the analysis is shown in Fig. 6.2(a). Point A in the figure indicates the probe for obtaining data from the local field. The iron core comprised ten layers with a thickness of each steel sheet of 0.475 mm. The fill factor was 95 %. The created mesh shown in Fig. 6.2(b) consisted of 10486 triangular elements. The linear triangular element was used for the vector potential with its degree of freedom being 5337.

The vector hysteretic property $\mathbf{h}(\mathbf{b})$ of the iron core in the FE analyses was calculated using the vector play model, which was identified by the measurement data of the non-oriented silicon steel sheet JIS 50A470. The B–H loops computed by the vector play model are shown in Fig. 6.3, in which the normal magnetization curve is plotted as a blue line. The conductivities of the steel sheet and the coil were 2.0×10^6 and 6.0×10^7 S/m, respectively.

A subtle but important point is that the analysis was implemented on the free FE software FreeFEM++ [40]. To the author's best knowledge, this is the first implementation of FE analysis employing the play model on free software.

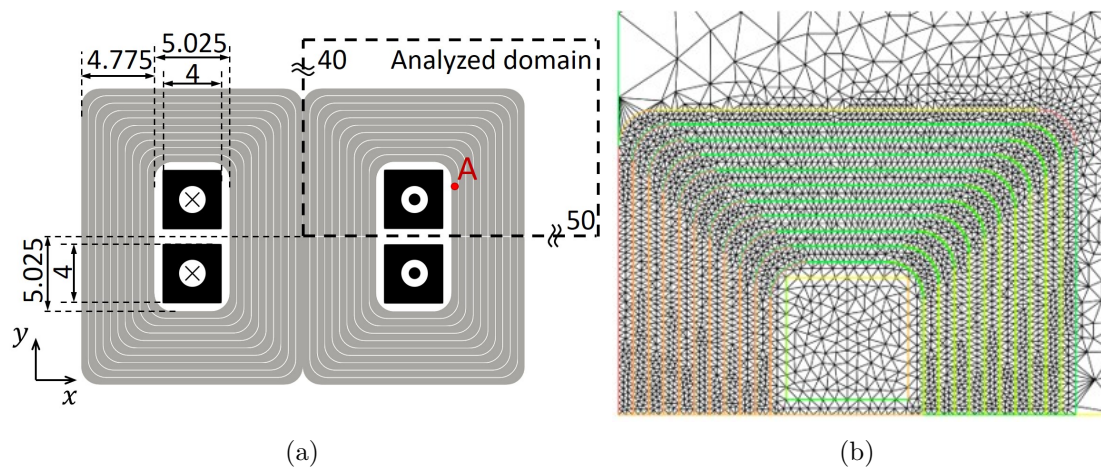


Figure 6.2: (a) Iron-core inductor used in the simulation. Point A indicates the probe for obtaining data from the local field. The unit of the dimension is mm.

(b) Mesh created in (a). ©2023 IEEE

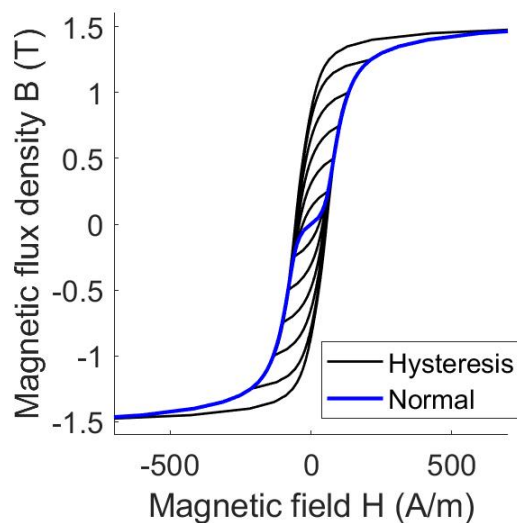


Figure 6.3: Symmetric B–H loop characteristics of the iron core given by the vector play model.

To evaluate the error of the SI method, a problem with good convergence was analyzed, and $\mathbf{b}_{\text{NR}} = \mathbf{C}\mathbf{a}_{\text{NR}}$ was used as the reference solution. Here, \mathbf{a}_{NR} denotes the solution to (6.5), which was solved iteratively using the NR method. The formulation for obtaining the variation in the NR method is shown in Appendix A.

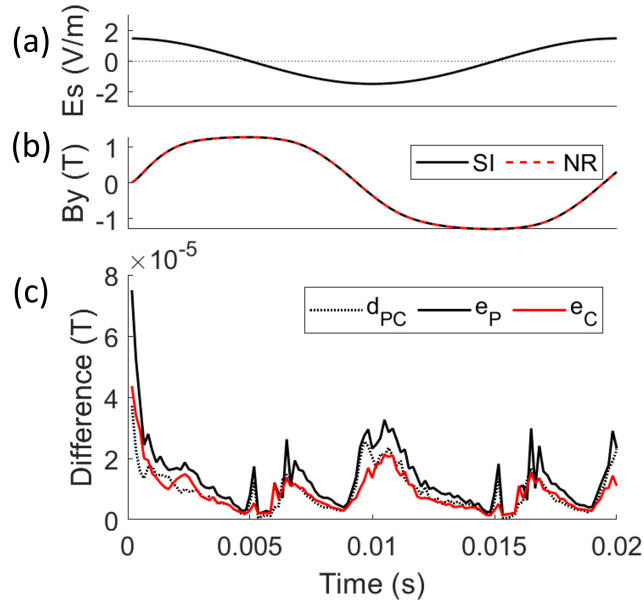


Figure 6.4: Results of the SI method with the sinusoidal electric field input E_s , which is plotted in (a). (b) Magnetic flux density at the probe. (c) PC difference d_{PC} and errors, e_P and e_C . ©2023 IEEE

6.1.4.1 Transient Analysis

Sinusoidal input A cosine electric field input E_s with an amplitude of 1.5 V/m and frequency of 50 Hz, as shown in Fig. 6.4(a), was applied to the coil. One period (0–0.02 s) was analyzed, and the number of time steps was 120.

Fig 6.5(a) shows H_y – B_y locus at probe A (see Fig. 6.2(a)). The locus of the SI method, which was the corrector obtained from (6.11), conformed with that of the NR method. The magnetic flux density at the probe is plotted in Fig. 6.4(b), which also shows good agreement.

Fig. 6.4(c) shows the differences among \mathbf{b}^* , \mathbf{b}_{m+1} , and \mathbf{b}_{NR} , where \mathbf{b}^* and \mathbf{b}_{m+1} were obtained from (6.9) and (6.11), respectively. The dotted line indicates the PC difference d_{PC} , which is the difference between the predictor and corrector, calculated as $d_{PC} = \text{ave}(|\mathbf{b}^* - \mathbf{b}_{m+1}|)$. The function $\text{ave}(\mathbf{x}) = \sum_i x_i / N_{f, \text{iron}}$, where $N_{f, \text{iron}}$ and x_i indicate the number of finite elements and value of the i -th element in the iron core region, respectively. The black and red solid lines correspond to the errors of the predictor $e_P = \text{ave}(|\mathbf{b}^* - \mathbf{b}_{NR, m+1}|)$ and corrector $e_C = \text{ave}(|\mathbf{b}_{m+1} - \mathbf{b}_{NR, m+1}|)$, respectively. The PC scheme effectively reduced the error, as evidenced by the lower value of e_C compared with e_P .

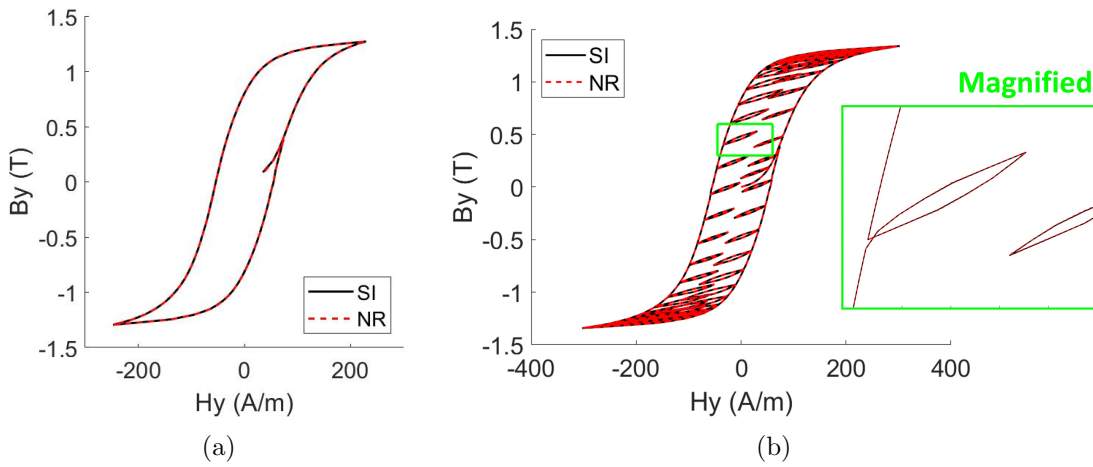


Figure 6.5: H_y - B_y locus of the SI and NR method with (a) sinusoidal and (b) PWM inputs. ©2023 IEEE

PWM input Subsequently, a PWM input, shown in Fig. 6.6(a), was applied to the coil. The amplitude was 3 V/m, and the fundamental and carrier frequencies were 50 Hz and 2.25 kHz, respectively.

Fig. 6.5(b) shows the H_y - B_y locus at the probe. The SI method accurately reproduced the minor loops, which was also confirmed in the waveform of B_y , shown in Fig. 6.6(b).

The error evaluation is presented in Fig. 6.6(c). When the input voltage was switched, the differential reluctance was discontinuous, resulting in an inaccurate prediction and an increase in e_P . However, in such instances, d_{PC} increases and e_C decreases, which indicates that the modification provided by (6.10) is also effective for discontinuous input.

6.1.4.2 Static Analysis

Magnetostatic analysis was conducted using a cosine electric field input E_s with an amplitude of 5.6×10^{-2} V/m shown in Fig. 6.7(a). The phase of the input was varied for 0 - $5\pi/2$ divided into 120 steps.

Fig. 6.8(a) shows the H_y - B_y loop at probe A, and the magnetic flux density at the probe is plotted in Fig. 6.7(b). The result of the SI method generally agreed with that of the NR method. Although some discrepancies between the two methods were observed in the B-H loop, the resultant I - Φ loops, shown in Fig. 6.8(b), were almost identical, where I and Φ are the current flowing through

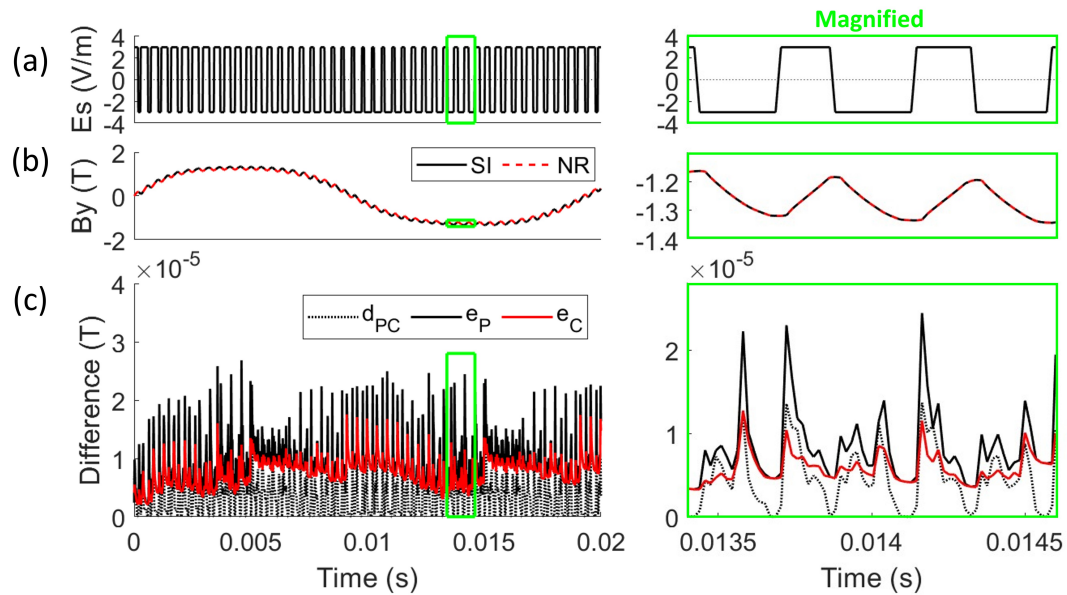


Figure 6.6: Results of the SI method with the PWM input shown in (a). Magnified figures are shown on the right. The plotted parameters in (b) and (c) are the same as those in Fig. 6.4. ©2023 IEEE

the coil and magnetic flux generated in the core, respectively. This result validated the use of the SI method for computing static loops, which are required for the identification of the play model, as described in Section 6.2.2.

The differences among the predictor, corrector, and solution of the NR method are shown in Fig. 6.7(c). When the change in input was large, the predictor error e_P increased owing to the significant change in the differential reluctivity. The PC difference was generally similar to e_P . The corrector error e_C was lower than e_P , which indicated that the differential reluctivity was effectively corrected by the PC scheme.

The NR method conducted about 4.2 solutions for iterative computation until convergence at each step, whereas the SI method required two solutions. The NR method also necessitated a line search at several steps, and the search was conducted five times in total.

6.1.4.3 Comparison of the computation time

The computation was performed using the finite element software FreeFem++ [40] on a computer with a 12th Gen Intel(R) Core(TM) i7-12700 2.10 GHz CPU. For the PWM input with the same number of time steps, the computation times of

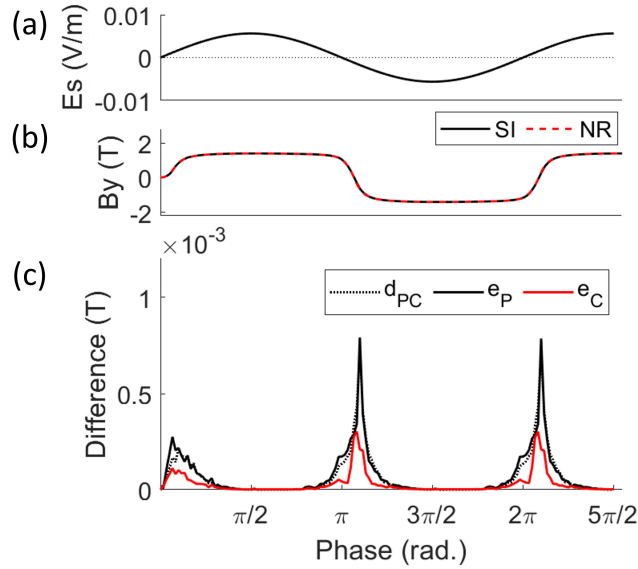


Figure 6.7: Results of a static analysis using the SI method with the sinusoidal input shown in (a). The plotted parameters in (b) and (c) are the same as those in Fig. 6.4.

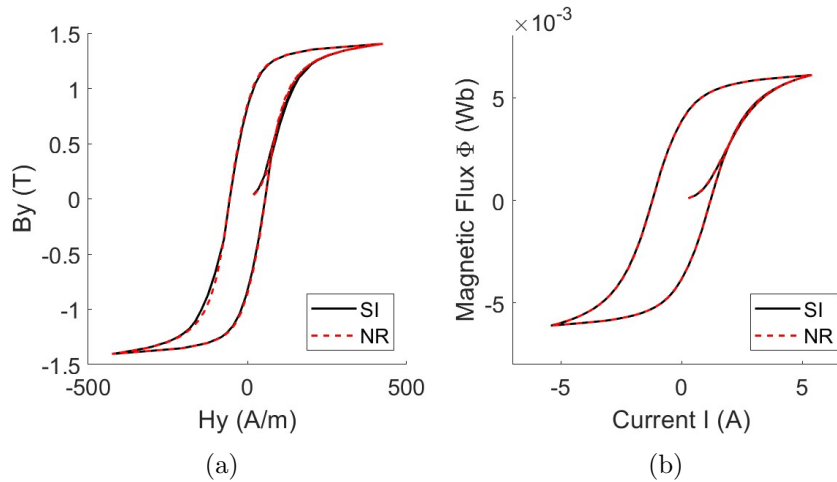


Figure 6.8: Static (a) H_y - B_y and (b) I - Φ loops of the SI and NR method.

the SI and NR methods were 8880 and 20650 s, respectively. The speed-up ratio of the proposed method was 2.33.

6.2 Hysteretic CLN Method

In this section, a method for incorporating hysteretic magnetic characteristics into the parameterized single-port CLN method is discussed.

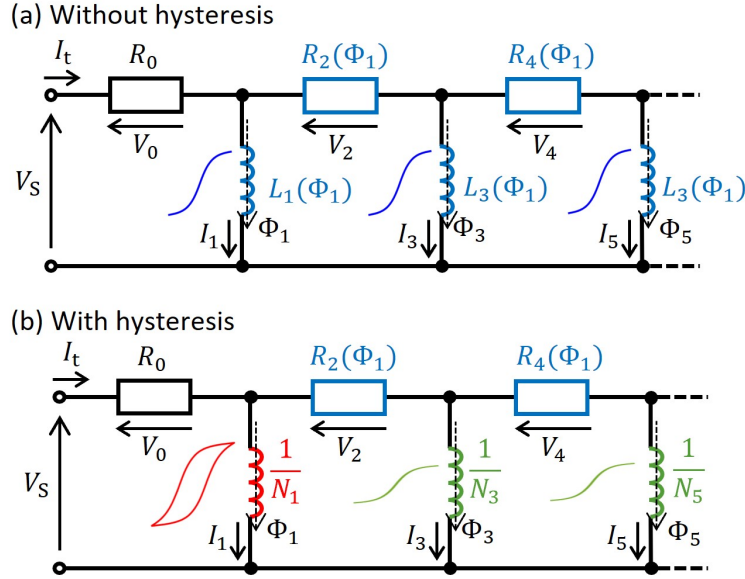


Figure 6.9: (a) Cauer ladder network (CLN) without hysteresis, where the circuit elements are functions of flux Φ_1 . (b) CLN with hysteresis, constructed by replacing the inductances of (a). The first stage inductance, representing the DC magnetic field, incorporates magnetic hysteresis characteristics.

6.2.1 CLN Without Hysteresis

CLN Recurrence Formula for a Laminated Core First, the nonlinear network elements of the CLN are generated without considering hysteresis, as depicted in Fig. 6.9(a). The circuit elements R_{2k} and L_{2k+1} are systematically obtained by solving the recurrence formula as introduced in Section 2.4. Specifically, in this chapter, the 2D analysis involving a laminated core region is conducted; hence, the scalar potential must be introduced to impose the condition that the eddy currents do not flow among the multiple domains. The recurrence formula including the scalar potential [34, 35] is introduced in the following.

The CLN recurrence formulae (2.61) and (2.62) are reintroduced here:

$$\mathbf{K}(\mathbf{a}_{2n+1} - \mathbf{a}_{2n-1}) = R_{2n} \boldsymbol{\sigma} \mathbf{e}_{2n}, \quad (6.16)$$

$$\mathbf{C}(\mathbf{e}_{2n+2} - \mathbf{e}_{2n}) = -\frac{1}{L_{2n+1}} \mathbf{C} \mathbf{a}_{2n+1}. \quad (6.17)$$

Let $\boldsymbol{\phi}_{2n+2}$ be a variable vector of the scalar potential discretized in the FE space when \mathbf{e}_{2n+2} is generated; (6.17) is rewritten as

$$\mathbf{e}_{2n+2} - \mathbf{e}_{2n} = -\frac{1}{L_{2n+1}} (\mathbf{a}_{2n+1} + \mathbf{G} \boldsymbol{\phi}_{2n+2}). \quad (6.18)$$

The term ϕ_{2n+2} merely adjusts the vector potential to satisfy specific conditions depending on the setting of analyses. It does not appear in the circuit representation. The CLN recurrence formula (6.16) and (6.17) are still satisfied when \mathbf{a}_{2n+1} is substituted to a new vector potential basis $\mathbf{a}'_{2n+1} = \mathbf{a}_{2n+1} + \mathbf{G}\phi_{2n+2}$; hence, the bases produced from (6.16) and (6.18) retains orthogonality.

With the assumption of a laminated core with N_L layers introduced in Section 6.1, the condition that the divergence of the eddy currents is zero in each domain can be imposed by determining $\mathbf{e}_{z,2n+2} = \mathbf{G}\phi_{2n+2}$ from

$$\mathbf{S}^T \mathbf{a}_{2n+1} + \mathbf{P} \mathbf{e}_{z,2n+2} = \mathbf{0}. \quad (6.19)$$

(6.19) is further transformed to

$$\mathbf{e}_{z,2n+2} = -\mathbf{P}^{-1} \mathbf{S}^T \mathbf{a}_{2n+1}. \quad (6.20)$$

The circuit elements R_{2k} and L_{2k+1} are obtained from the recursive solution of (6.16), (6.18), and (6.20).

Parameterization Chapter 4 shows that the computational accuracy for motor applications is improved by using the magnetic flux as a parameter. Hence, the method here also employs $\nu = \nu(\Phi_1)$, where $\Phi_1 = L_1 I_1$ is the first-stage magnetic flux. Consequently, R_{2k} and L_{2k+1} are also functions of Φ_1 , as shown in Fig. 6.9(a).

State Equations Section 3.3.4 shows that the state equations (3.31) and (3.32) directly derived from the magnetic flux can incorporate the parameter variation. The same equations are employed for hysteretic model order reduction, and (2.52), (3.31), and (3.32) are rewritten into the form of matrix calculation as

$$\frac{d\Phi}{dt} = \mathbf{v}'_s - \mathbf{R}' \mathbf{i}, \quad (6.21)$$

where

$$\Phi = [\Phi_1, \dots, \Phi_{2N_s-1}]^T, \quad (6.22)$$

$$\mathbf{v}_s = [V_s, 0, \dots, 0]^T, \quad \mathbf{v}'_s = \mathbf{U}^T \mathbf{v}_s, \quad (6.23)$$

$$\mathbf{R} = \text{diag}(R_0, \dots, R_{2N_s-2}), \quad \mathbf{R}' = \mathbf{U}^T \mathbf{R} \mathbf{U}, \quad (6.24)$$

$$\mathbf{i} = [I_1, \dots, I_{2N_s-1}]^T. \quad (6.25)$$

The matrix \mathbf{U} is an upper triangular matrix with unity components.

6.2.2 Construction of the Hysteretic CLN

For inclusion of the hysteretic property, the first inductor L_1 in Fig. 6.9(a) is replaced with a hysteretic inductor, as shown in Fig. 6.9(b). Because the first inductor provides magnetostatic property, its hysteretic property is given as described below.

First, symmetric I - Φ loops are generated through 2D FE magnetostatic analysis by applying a DC voltage input to the machine. The hysteretic magnetic field at each finite element is represented by the vector play model [39], whose input and output are magnetic flux density \mathbf{B} and magnetic field \mathbf{H} , respectively.

Here, the SI method for static problem combined with the PC scheme (Section 6.1.3) is employed as an iterative solution method instead of the NR method to obtain the static loops faster with better convergence. Next, the scalar play model [41] is identified to obtain I_1 from Φ_1 using the obtained I - Φ loops as

$$I_1 = P(\Phi_1) = \sum_{n=1}^{N_p} f_n(p_{\zeta_n}(\Phi_1)), \quad (6.26)$$

where $f_n(p_{\zeta_n})$ is a single-valued shape function representing the magnetic saturation, and p_{ζ_n} is the play hysteron; N_p is the number of play hysterons. The hysteron is given by

$$p_{\zeta_n}(\Phi_1) = \max(\min(p_{\zeta_n}^0, \Phi_1 + \zeta_n), \Phi_1 - \zeta_n), \quad (6.27)$$

where $p_{\zeta_n}^0$ is the hysteron in the previous step, $\zeta_n = (n-1)\Phi_s/N_p$ is the half-width of the hysteron, and Φ_s is the maximum magnetic flux at which hysteresis can be represented. The shape functions are determined using the method described in Ref. [41].

6.2.3 Online Calculation of Hysteretic CLN

An implicit time-stepping scheme is generally used to solve the time evolution of state equations to achieve numerical stability. Equation (6.21) can be solved using

the modified implicit Euler method:

$$\frac{\Phi_{m+1} - \Phi_m}{\Delta t} = \mathbf{v}'_{s,m+1} - \mathbf{R}'(\Phi_m) \mathbf{i}_{m+1}, \quad (6.28)$$

where a state variable with the subscript m denotes the variable at the m -th time step, Δt indicates the time step, and $\mathbf{i}_{m+1} = \mathbf{i}(\Phi_{m+1})$. It is called the “modified” implicit Euler method because \mathbf{R}' is determined by Φ_m instead of Φ_{m+1} . The numerical result is empirically known to be stable even when the modified method is used.

The NR method is a widely employed iteration method to solve nonlinear equations such as (6.28); however, when a hysteretic element is included, it can suffer from poor convergence. The SI method with the linear approximation introduced in Section 6.1 can be used to avoid nonlinear iterative solutions:

$$\mathbf{i}(\Phi_{m+1}) \approx \mathbf{i}(\Phi_m) + \mathbf{N}(\Phi_m)(\Phi_{m+1} - \Phi_m), \quad (6.29)$$

where matrix \mathbf{N} is

$$\mathbf{N} = \frac{\partial \mathbf{i}}{\partial \Phi} = \text{diag}(N_1, N_3, \dots, N_{2N_s-1}). \quad (6.30)$$

Substituting (6.29) into (6.28) yields the following equation:

$$F(\Phi_{m+1})_{\text{SI}} = \frac{\Phi_{m+1} - \Phi_m}{\Delta t} - \mathbf{v}'_{s,m+1} - \mathbf{R}'(\Phi_m) \mathbf{i}[(\Phi^m) + \mathbf{N}(\Phi^m)(\Phi^{m+1} - \Phi^m)] = \mathbf{0}. \quad (6.31)$$

This is a linear equation for Φ_{m+1} . Hence, iterations for nonlinear solutions are not required.

The component N_1 is determined from the hysteretic properties provided by the scalar play model (see Fig. 6.9(b)), where $N_1 = dP(\Phi_1)/d\Phi_1$ is derived using (6.26).

There are several choices to represent N_{2k+1} ($k = 1, 2, \dots, N_s - 1$). Here, the reversible component $P_{\text{rev}}(\Phi_1) = f_1(\Phi_1)$ of the play model is employed based on the results reported in Ref. [23]; the B - H curve obtained from the CLN showed good agreement with the measurement and FE analysis results particularly when the inductors L_{2k+1} ($k = 1, 2, \dots$) are determined from the reversible component.

This is because high-order modes contribute significantly to the rotation of magnetization but not significantly to the magnetic domain wall motion. The slope of the reversible component is obtained by using only the first hysteron introduced in Appendix B.2. To preserve the ratio of the inductances, N_{2k+1} is calculated as:

$$N_{2k+1} = \frac{L_1(\Phi_1)}{L_{2k+1}(\Phi_1)} \frac{dP_{\text{rev}}(\Phi_1)}{d\Phi_1}, \quad (6.32)$$

where L_1, L_3, \dots are given by the non-hysteretic CLN introduced in Section 6.2.1.

6.2.4 Numerical Analysis

The model shown in Fig. 6.2 was analyzed, where the characteristics of the iron core were modeled using the vector play model with the same measurement data as the one introduced in Section 6.1.4. The conductivities of the steel sheet and coil were 1.0×10^6 and 4.0×10^7 S/m, respectively.

6.2.4.1 Offline Calculation

Preparation of Network Elements The CLN elements L_{2k+1} and R_{2k} obtained using the non-hysteretic CLN recurrence formula including the scalar potential (6.16), (6.18) and (6.20) are shown in Fig. 6.10 (a) and (b). Before the recurrence formula was solved, the distribution of ν was determined as a function of I_1 through magnetostatic analysis. The normal magnetization curve was used as the magnetic property. Fig. 6.10(c) and (d) show the resistance R_{2k} and ratio L_{2k+1}/L_1 in (6.32) as a function of Φ_1 , respectively.

Identification of the Scalar Play Model The I - Φ loops obtained using the static FE analysis are shown in Fig. 6.11 (a). Fifty-two loops were generated (four of them are plotted), the maximum flux Φ_s was 5.2×10^{-3} Wb, the amplitude of the r -th loop was $\Phi_r = 2r\Phi_s/N_p$ ($r = 1, \dots, N_p/2$), and the number of hysterons was $N_p = 104$.

The solid black lines in Fig. 6.11(b) show I - Φ loops generated using the identified scalar play model. The green line shows the characteristics of the reversible component.

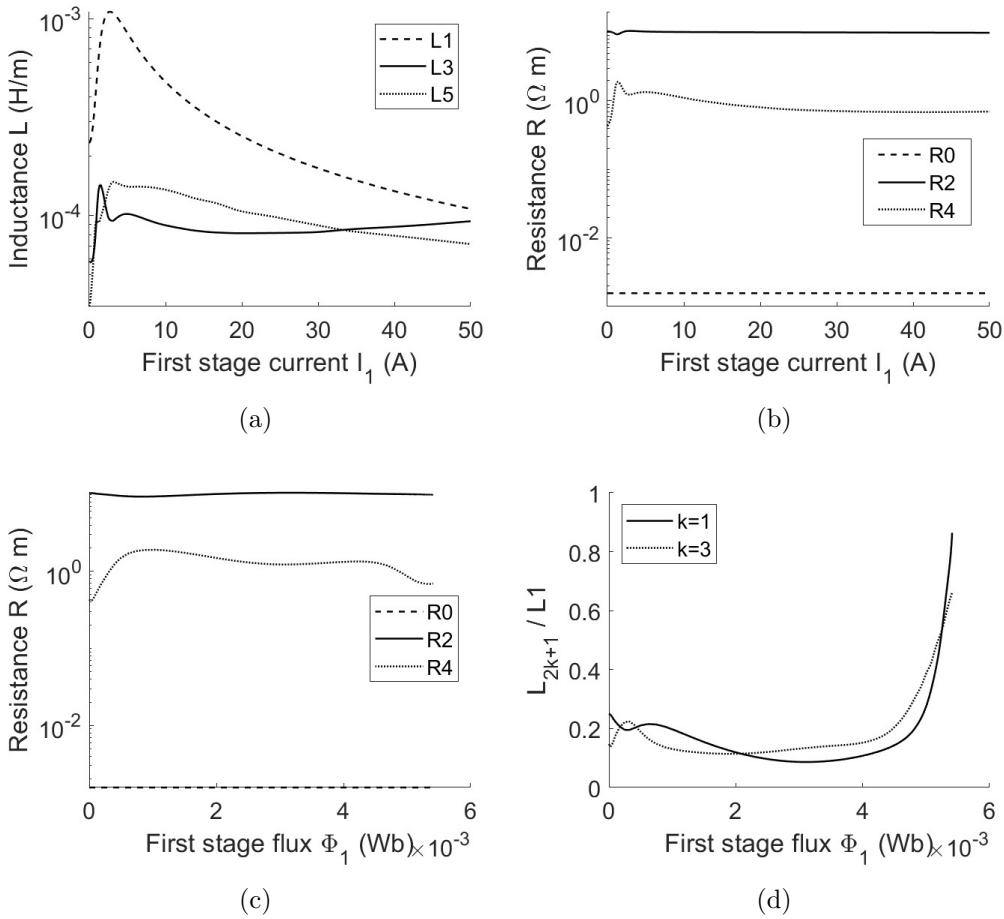


Figure 6.10: (a) Inductance and (b) resistance of the CLN as functions of I_1 without hysteresis characteristics. (c) CLN resistances as functions of the first stage magnetic flux $\Phi_1 = L_1 I_1$. (d) Ratio of the inductances L_{2k+1}/L_1 ($k = 1, 2$).

6.2.4.2 Online Calculation

A PWM input was applied to the coil. The amplitude was 1.5 V/m; the fundamental and carrier frequencies were 50 Hz and 10.25 kHz, respectively, and the simulated time range was $0-1.9 \times 10^{-2}$ s. The CLN constituted three stages. When \mathbf{B} was small, the skin depth at 10.25 kHz was 0.14 mm, which was sufficiently thinner than the thickness of the iron sheet (0.5 mm); hence, the carrier wave was expected to have a considerable influence on the eddy current.

Fig. 6.12 (a), (b), and (c) show the locus of the total current I_t and the first-stage magnetic flux Φ_1 obtained using the hysteretic and non-hysteretic transient FE analysis (red and blue lines, respectively), proposed CLN method (solid black line), and CLN truncated at R_2 (dotted black line). The clear difference between

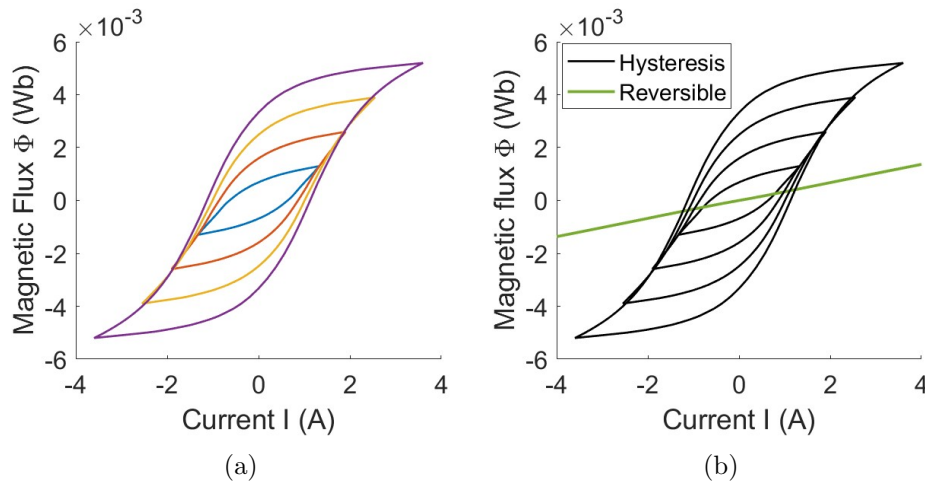


Figure 6.11: (a) Symmetric I - Φ loops obtained using FE static analysis. Four loops are shown out of 52 generated loops. (b) Loops produced using the identified scalar play model.

the non-hysteretic and hysteretic FE analyses demonstrates the importance of considering magnetic hysteresis. The proposed CLN method yielded a locus close to the transient hysteretic FE analysis, which showed that the CLN method can accurately simulate the hysteretic eddy-current field with only six circuit elements, even when the input has high-frequency components. In contrast, the truncated CLN failed to represent the curves of the minor loops, indicating that L_3 and L_5 played a key role in modeling the minor loops.

Fig. 6.12 (d) compares the computed iron losses. The result obtained using the proposed CLN method was close to that obtained using the FE analysis.

6.2.4.3 Computation Time

The linear solutions in the FE space dominate the computational cost. Identical finite elements were used for the FE space computations in the FE and CLN analyses. Therefore, the following discussion compares the required number of linear solutions between the transient FE analysis and CLN method, assuming that the computation time of the CLN state equations is negligible and the vector play model is prepared beforehand.

The transient FE analysis shown in Fig. 6.12 required 398325 linear solutions, where the average number of Newton iterations was 2.0. The number of time steps was 198960, which was large but necessary to ensure high accuracy.

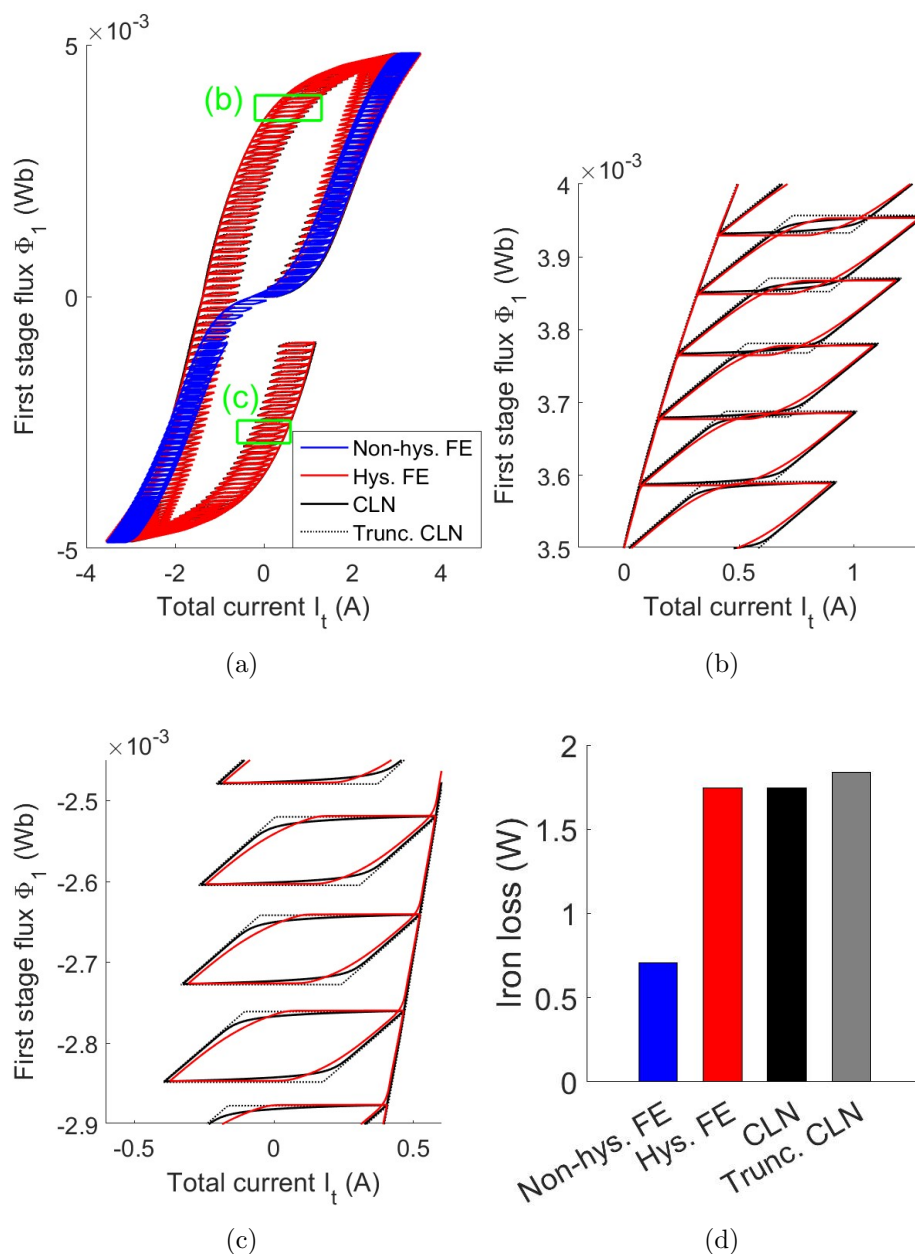


Figure 6.12: (a) Locus of the total current I_t and magnetic flux Φ_1 obtained using the non-hysteretic and hysteretic FE analyses (blue and red lines, respectively), proposed CLN method (solid black line), and truncated CLN (dotted black line). (b)(c) Magnified figures of (a). (d) Comparison of the iron loss.

In the CLN method, loop generation required $52 \times 150 \times 2 = 15600$ linear solutions, where 52 loops were computed with 150 phase divisions and two iterations per phase. The generation of CLN elements required $27 \times (4.8 + 3) = 210$ linear solutions, where each parameter $I_1 = 0-50$ A (27 divisions in the log scale) required 4.8 iterations on average to determine the reluctivity matrix and three linear solutions to solve the recurrence formula of the three-stage CLN. Thus, the

total number of linear solutions in the CLN method was 15810.

The speed-up ratio of the CLN to the FE analysis was $398325/15810 \approx 25.2$. It increases for analyses with a larger number of time steps and simulation cases.

6.3 Summary

The transient analysis of the hysteretic magnetic field is studied as a nonlinear problem. First, the SI method is introduced to speed up the analysis and solve the problem of ill convergence, which frequently occurs in the hysteretic calculation. An iterative procedure is avoided by using the linear approximation, and the combination with the PC method improves the accuracy. In numerical analyses, the B–H loci of the SI method conformed with those of the NR method both in transient and static analyses, and the error was effectively reduced by the PC scheme. The proposed SI method reduced the computation time by a factor of 2.33 compared with the NR method with the same number of timesteps.

Subsequently, a parameterized CLN method incorporating hysteresis characteristics is developed and applied to the nonlinear transient analysis of an iron-core inductor. The first-stage inductor is modeled using the scalar play model, which is identified by the static loops obtained using the SI method. The I – Φ locus obtained using the proposed method reproduces that obtained using the FE transient analysis. The linear solutions are reduced by $1/25$ compared with the FE transient analysis.

Chapter 7

Concluding Remarks

This thesis has developed the parameterized CLN method to establish a MOR method that considers nonlinear magnetic characteristics. First, the effect of the parameter variation on the CLN method is numerically studied. Subsequently, the parameterized CLN method is used to analyze an IM and a VR stepper motor. It is also extended to transient analysis incorporating the magnetic hysteresis characteristics.

The contributions and findings of this thesis are summarized as follows:

Chapter 3

- A parameterized CLN method is formulated to incorporate the nonlinear magnetic characteristics. The parameter variation terms, which represent the dynamic behavior of an orthogonal basis, are derived through an exact formulation of the parameterized CLN.
- The parameter variation terms play a significant role in the state equations when the reluctivity is used, whereas they are negligible when the differential reluctivity is used.
- The circuit equations using the magnetic flux as state variables yield an acceptable result without the parameter variation terms.

Chapter 4

- The parameterized multi-port CLN method is developed and applied to an induction motor analysis.

- The choice of parameters is important to achieve fast and accurate analysis. When the amplitude and phase of coil magnetic flux or gap magnetic flux are used as the parameters, the developed method is effective at various slips and frequencies.

Chapter 5

- The parameterized multi-port CLN method is applied to the analysis of a VR stepper motor. The amplitude of the coil magnetic flux and step sequence are used for the parameters.
- The parameterized CLN method shows good agreement with the FE method even for analyses of dynamical operations, such as stepwise rotation and step-out motion, without any additional offline preparations.

Chapter 6

- The magnetic hysteresis characteristics of the iron core are incorporated into the parameterized single-port CLN method. The first-stage inductance is determined using the play model as a modeling method of hysteresis.
- The SI method is proposed for the hysteretic FE analysis. It is used to produce static loops, which are required to prepare the play model, with less computation time than the NR method. It is also effective in avoiding iterative calculations and reducing the computation time of eddy-current analysis.

Chapters 3–6

- The computation time of nonlinear transient analyses can be significantly reduced by applying the parameterized CLN when the number of time steps is large. The threshold number of time steps is derived from the comparison of the linear solutions required in the FEM and CLN.
- All the presented analyses were conducted on FE analysis software FreeFEM++, including the computation of magnetic hysteresis at each element using the play model.

The limitation of the CLN method is that the derivation of the circuit elements is time-consuming, i.e., it requires nonnegligible time for offline computation. On the other hand, the CLN method is suitable for analyzing the same geometry with a large number of time steps and/or various conditions.

Expected future research points are as follows:

- The nonlinearization of the rotor network in the multi-port CLN.
- Inclusion of the iron loss in the stator and rotor regions of the parameterized multi-port CLN method. The iron loss in both regions was incorporated into the CLN using the homogenization method in [33], where the linear magnetic characteristics were assumed. The same approach may be useful for the parameterized CLN.
- Error evaluation of the parameterized CLN method for determining the required number of stages. The difference in the reconstructed electromagnetic field is desirable for the definition of the error. The error estimation methods established in the frequency domain [42–44] might be extended to the time domain analysis.
- Application of the hysteretic CLN method to motor analysis.
- Using the parameterized CLN as a behavior model for exploring optimal control of IMs and VR stepper motors. The eddy currents under high-frequency input are expected to be considered in the optimization.

Concerning the last point, the parameterized CLN method can facilitate the exploration of optimal control of electric machines, particularly IMs and stepper motors, even when the eddy currents largely influence the machine characteristics under high-frequency input. It may contribute to achieving the required motor drive with less restriction from the finite availability of energy and rare-earth materials.

Appendix A

Newton–Raphson Method for Hysteretic FE Analysis of Laminated Cores

This chapter provides a formulation for an iterative solution of a nonlinear eddy-current problem using the Newton–Raphson (NR) method, where the implicit Euler method is employed as a time marching scheme. Here, it is assumed that the hysteretic magnetic characteristics are computed using a model whose input is the magnetic flux density and outputs are the magnetic field and differential reluctivity. For convenience, (6.5) is rewritten as

$$M\mathbf{y}_{m+1} = \mathbf{g}, \quad (\text{A.1})$$

where

$$M = \begin{bmatrix} \frac{\sigma}{\Delta t} & \mathbf{S} \\ \mathbf{S}^T & \Delta t \mathbf{P} \end{bmatrix}, \quad \mathbf{y}_{m+1} = \begin{bmatrix} \mathbf{a}_{m+1} \\ \mathbf{e}_{z,m+1} \end{bmatrix},$$
$$\mathbf{g} = \begin{bmatrix} -\mathbf{C}^T \mathbf{h}_{m+1} + \frac{\sigma \mathbf{a}_m}{\Delta t} + \mathbf{j}_{m+1} \\ \mathbf{S}^T \mathbf{a}_m \end{bmatrix}. \quad (\text{A.2})$$

When

$$\mathbf{F}(\mathbf{y}_{m+1}) = M\mathbf{y}_{m+1} - \mathbf{g} = \mathbf{0} \quad (\text{A.3})$$

is solved using the NR method with the nonlinear magnetic characteristics, \mathbf{h} in the vector \mathbf{g} is corrected at each NR iteration. The variation $\delta\mathbf{y}_{m+1}$ for updating the solution at each iteration is derived from

$$\mathbf{F}(\mathbf{y}_{m+1} + \delta\mathbf{y}_{m+1}) \approx \mathbf{F}(\mathbf{y}_{m+1}) + \frac{\partial\mathbf{F}}{\partial\mathbf{y}_{m+1}}\delta\mathbf{y}_{m+1} \quad (\text{A.4})$$

$$= \mathbf{F}(\mathbf{y}_{m+1}) + \mathbf{M}_2\delta\mathbf{y}_{m+1} = \mathbf{0}, \quad (\text{A.5})$$

where

$$\mathbf{M}_2 = \mathbf{M} - \partial\mathbf{g}/\partial\mathbf{y}_{m+1}. \quad (\text{A.6})$$

Let \mathbf{h}^k be the magnetic field at the k -th nonlinear iteration; \mathbf{M}_2 is calculated as

$$\mathbf{M}_2 = \begin{bmatrix} \frac{\sigma}{\Delta t} + \frac{\partial(\mathbf{C}^T\mathbf{h}^k)}{\partial\mathbf{a}} & \mathbf{S} \\ \mathbf{S}^T & \Delta t\mathbf{P} \end{bmatrix} \quad (\text{A.7})$$

$$= \begin{bmatrix} \frac{\sigma}{\Delta t} + \mathbf{C}^T\boldsymbol{\nu}_d^k\mathbf{C} & \sigma\mathbf{S} \\ \mathbf{S}^T & \Delta t\mathbf{P} \end{bmatrix}, \quad (\text{A.8})$$

where $\boldsymbol{\nu}_d^k$ is the differential reluctivity matrix at the k -th nonlinear iteration.

Appendix B

Play Model

B.1 Macroscopic Models of Magnetic Hysteresis

The magnetic hysteretic characteristics of the ferromagnetic materials are the dominant sources of loss in electric machines. In the analysis of electric machines, macroscopic modeling methods, such as Jiles–Atherton (J–A) model [45], Preisach model, and play model, are commonly employed to represent the hysteretic magnetic characteristics of the iron core. These macroscopic hysteretic modeling methods are constructed based on the measured magnetic properties of the core materials.

The play model is mathematically equivalent to but more computationally efficient than the Preisach model [46], which was shown to represent minor loops more accurately than the J–A model [47]. The play model for representing hysteretic characteristics is introduced in the following.

B.2 Scalar Play Model

The play model is a phenomenological model that employs play hysterons with various widths ζ (Fig. B.1) to represent the “play” that contributes to hysteresis characteristics. Suppose X and Y are the scalar input and output of the model, respectively. When the input X transitions from increasing to decreasing (or from decreasing to increasing), the output Y does not begin to decrease (or increase) instantly but exhibits a delay in response. This represents the adherence and energy

dissipation around the impurities and lattice defects in ferromagnetic materials when the magnetic domain wall moves.

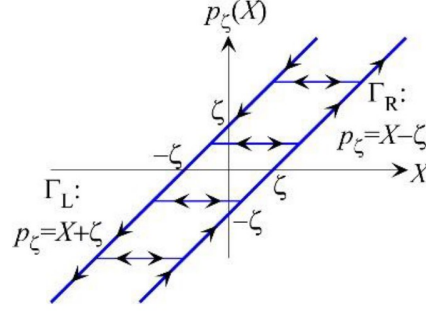


Figure B.1: Play hysteron with its width ζ [1]. It responds with some delay when the change in input X is inverted.

The play model represents hysteretic characteristics through the sum of play hysterons as

$$Y = P(X) = \sum_{n=1}^{N_p} f_n(p_{\zeta_n}(X)), \quad (\text{B.1})$$

where N_p is the number of hysterons, and $f_n(p_{\zeta_n}) = f(\zeta_n, p_{\zeta_n})$ is a single-valued function called a shape function representing the saturation. The n -th play hysteron p_{ζ_n} is represented as

$$p_{\zeta_n}(X) = \max(\min(p_{\zeta_n}^0, X + \zeta_n), X - \zeta_n). \quad (\text{B.2})$$

Here, $p_{\zeta_n}^0$ is the value of hysteron at the previous step, and $\zeta_n = (n - 1)X_s/N_p$ is the half-width of the hysteron. The output Y is assumed to become a single-valued function when $X > |X_s|$.

Practically, the shape functions are prepared in the form of piecewise linear functions. Let j denote the index for the value of hysteron p divided by an interval $\Delta p = 2X_s/N_p$, and $p_{n,j} = j\Delta p - X_s + \zeta_n$ ($j = 0, \dots, N_p - n + 1$). The n -th shape function within the range of $p_{n,j-1} \leq p \leq p_{n,j}$ is given by

$$f_n(\zeta_n, p) = f_{n,j-1} + \mu'(n, j)(p - p_{n,j-1}). \quad (\text{B.3})$$

Here, $f_{n,j} = f(\zeta_n, p_{n,j})$, and $\mu'(n, j) = (f_{n,j} - f_{n,j-1})/\Delta p$ provides the slope of the shape function.

Although using $(X, Y) = (H, B)$ is natural for the representation of the play model, the magnetic field analysis often employs the magnetic vector potential for the unknown variable, and $(X, Y) = (B, H)$ is suitable for determining the material characteristics during the computation. It can be easily achieved by swapping the input and output data of the loops for identification.

Several methods exist to determine shape functions f_n ; this thesis employs a method that uses the Everett integral, which is generated from symmetric B-H loops [1].

B.3 Vector Play Model

A vector hysteresis model is required to handle rotational magnetization or material anisotropy. Two methods have been proposed for the vectorization of the play model: one is superposing the scalar models, and the other is extending the scalar model geometrically. The latter has been confirmed to have higher computational efficiency [48]; hence, the following explanation focuses on the geometrical extension of the scalar play model.

When the vector input and output of the model are \mathbf{X} and \mathbf{Y} , respectively, (B.1) is vectorized as

$$\mathbf{Y} = \mathbf{P}(\mathbf{X}) = \sum_{n=1}^{N_p} \mathbf{f}(\zeta_n, \mathbf{p}_{\zeta_n}(\mathbf{X})), \quad (\text{B.4})$$

where \mathbf{f} is the vectorized shape function

$$\mathbf{f}(\zeta, \mathbf{p}) = f(\zeta, |\mathbf{p}|) \frac{\mathbf{p}}{|\mathbf{p}|}, \quad (\text{B.5})$$

and \mathbf{p}_{ζ_n} is the vectorized n -th play hysteron

$$\mathbf{p}_{\zeta_n}(\mathbf{X}) = \mathbf{X} - \frac{\zeta_n(\mathbf{X} - \mathbf{p}_{\zeta_n}^0)}{\max(\zeta_n, |\mathbf{X} - \mathbf{p}_{\zeta_n}^0|)}. \quad (\text{B.6})$$

Here, ζ_n is the radius of the vector play hysteron, and $\mathbf{p}_{\zeta_n}^0$ is the value of the hysteron at the previous step.

Iterative solutions using the NR method require the differentiation of vector hysteretic function. The original formulation (B.5) has difficulty in calculating $\partial \mathbf{f} / \partial \mathbf{B}$, which contains inversed terms of $|\mathbf{p}_\zeta|$. To overcome the numerical problem, Ref. [39] proposed a mathematically equivalent representation of the shape function:

$$\mathbf{f}(\zeta, \mathbf{p}) = f_0(\zeta, |\mathbf{p}|^2) \mathbf{p}, \quad (\text{B.7})$$

where $f_0(\zeta, q) = f_0(\zeta, p^2) = f(\zeta, p)/p$, and $q = p^2$. The detailed derivation of differentials required for the NR method was introduced in [39].

Although the equations (B.4)–(B.6) satisfactory model the hysteresis loss of alternating magnetic field, they cannot represent the decrease in rotational hysteresis loss in the magnetic saturation. When magnetic saturation causes the magnetic domains to become single-domain, the magnetic domain walls do not move under the rotating magnetic field. Therefore, hysteresis loss decreases with an increase in magnetic flux density. The rotational hysteresis characteristics are corrected as

$$\mathbf{P}^*(\mathbf{X}) = \mathbf{P}_\parallel(\mathbf{X}) + r(|\mathbf{X}|) \mathbf{P}_\perp(\mathbf{X}), \quad (\text{B.8})$$

where \mathbf{P}_\parallel and \mathbf{P}_\perp are the parallel and perpendicular components of \mathbf{P} to \mathbf{X} , respectively. The ratio $r(|\mathbf{X}|)$ is defined as $r(X) = L_{\text{mea}}/L_{\text{sim}}$, where L_{mea} is a measured rotational loss with an amplitude $|\mathbf{X}|$, whereas L_{sim} is a simulated rotational loss without the correction.

Bibliography

- [1] T. Matsuo, “Magnetic Hysteresis Represented by Play Model,” in *Magnetic Material for Motor Drive Systems: Fusion Technology of Electromagnetic Fields*, ser. Engineering Materials, K. Fujisaki, Ed., Singapore, 2019, pp. 191–202.
- [2] T. Henneron and S. Clénet, “Model Order Reduction of Non-Linear Magnetostatic Problems Based on POD and DEI Methods,” *IEEE Transactions on Magnetics*, vol. 50, no. 2, pp. 33–36, 2014.
- [3] Y. Sato, M. Clemens, and H. Igarashi, “Adaptive Subdomain Model Order Reduction With Discrete Empirical Interpolation Method for Nonlinear Magneto-Quasi-Static Problems,” *IEEE Transactions on Magnetics*, vol. 52, no. 1100204, 2016.
- [4] Y. Sato, T. Shimotani, and H. Igarashi, “Synthesis of Cauer-equivalent circuit based on model order reduction considering nonlinear magnetic property,” *IEEE Transactions on Magnetics*, vol. 53, no. 1100204, 2017.
- [5] M. R. Hasan, L. Montier, T. Henneron, and R. V. Sabariego, “Stabilized reduced-order model of a non-linear eddy current problem by a gappy-POD approach,” *IEEE Transactions on Magnetics*, vol. 54, no. 8001808, 2018.
- [6] A. Kameari, H. Ebrahimi, K. Sugahara, Y. Shindo, and T. Matsuo, “Cauer ladder network representation of eddy-current fields for model order reduction using finite-element method,” *IEEE Transactions on Magnetics*, vol. 54, no. 7201804, 2018.
- [7] S. L. Brunton and J. N. Kutz, *Data-Driven Science and Engineering: Machine Learning, Dynamical Systems, and Control*, 2022.

- [8] T. Henneron and S. Clénet, “Model order reduction applied to the numerical study of electrical motor based on POD method taking into account rotation movement,” *International Journal of Numerical Modelling: Electronic Networks, Devices and Fields*, vol. 27, no. 3, pp. 485–494, 2014.
- [9] T. Shimotani, Y. Sato, T. Sato, and H. Igarashi, “Fast finite-element analysis of motors using block model order reduction,” *IEEE transactions on magnetics*, vol. 52, no. 7207004, 2015.
- [10] L. Montier, T. Henneron, S. Clénet, and B. Goursaud, “Model Order Reduction Applied to a Linear Finite Element Model of a Squirrel Cage Induction Machine Based on POD Approach,” *IEEE Transactions on Magnetism*, vol. 57, no. 3066678, 2021.
- [11] L. Montier, T. Henneron, S. Clénet, and B. Goursaud, “Transient simulation of an electrical rotating machine achieved through model order reduction,” *Advanced Modeling and Simulation in Engineering Sciences*, vol. 3, no. 10, 2016.
- [12] A. E. Boumesbah, F. Martin, G. Krebs, A. Belahcen, and C. Marchand, “Comparison of Model Order Reduction Methods for a Switched Reluctance Machine Characterization,” *IEEE Transactions on Magnetism*, vol. 57, no. 7400906, 2021.
- [13] V. Mukherjee, M. F. Far, F. Martin, and A. Belahcen, “Constrained Algorithm for the Selection of Uneven Snapshots in Model Order Reduction of a Bearingless Motor,” *IEEE Transactions on Magnetism*, vol. 53, no. 7205304, 2017.
- [14] S. Paul and J. Chang, “Fast Numerical Analysis of Electric Motor Using Non-linear Model Order Reduction,” *IEEE Transactions on Magnetism*, vol. 54, no. 8101404, 2018.
- [15] P. Feldmann and R. W. Freund, “Efficient linear circuit analysis by Padé approximation via the Lanczos process,” *IEEE Transactions on Computer-Aided Design of Integrated Circuits and Systems*, vol. 14, no. 5, pp. 639–649, 1995.
- [16] Y. Sato and H. Igarashi, “Homogenization Method Based on Model Order Reduction for FE Analysis of Multi-Turn Coils,” *IEEE Transactions on Magnetism*, vol. 53, no. 1100104, 2017.

-
- [17] P. Feldmann and R. W. Freund, “Reduced-order modeling of large linear subcircuits via a block Lanczos algorithm,” in *Proceedings of the 32nd Annual Acm/Ieee Design Automation Conference*, 1995, pp. 474–479.
- [18] J. Aliaga, D. Boley, R. Freund, and V. Hernández, “A Lanczos-type method for multiple starting vectors,” *Mathematics of Computation*, vol. 69, no. 232, pp. 1577–1601, 2000.
- [19] J. Kokernak and D. Torrey, “Magnetic circuit model for the mutually coupled switched-reluctance machine,” *IEEE Transactions on Magnetics*, vol. 36, no. 2, pp. 500–507, 2000.
- [20] Y. Hane and K. Nakamura, “Reluctance network model of permanent magnet synchronous motor considering magnetic hysteresis behavior,” in *2018 IEEE International Magnetics Conference (INTERMAG)*, 2018.
- [21] T. Matsuo, A. Kameari, K. Sugahara, and Y. Shindo, “Matrix formulation of the Cauer ladder network method for efficient eddy-current analysis,” *IEEE Transactions on Magnetics*, vol. 54, no. 7205805, 2018.
- [22] J. Krahn, “Optimum discretization of a physical Cauer circuit,” *IEEE Transactions on Magnetics*, vol. 41, no. 5, pp. 1444–1447, 2005.
- [23] Y. Shindo, T. Miyazaki, and T. Matsuo, “Cauer circuit representation of the homogenized eddy-current field based on the Legendre expansion for a magnetic sheet,” *IEEE Transactions on Magnetics*, vol. 52, no. 6300504, 2016.
- [24] T. Miyazaki, T. Mifune, T. Matsuo, Y. Shindo, Y. Takahashi, and K. Fujiwara, “Equivalent circuit modeling of dynamic hysteretic property of silicon steel under pulse width modulation excitation,” *Journal of Applied Physics*, vol. 117, no. 17, p. 17D110, 2015.
- [25] J. Gyselinck and P. Dular, “A time-domain homogenization technique for laminated iron cores in 3-D finite-element models,” *IEEE Transactions on Magnetics*, vol. 40, no. 2, pp. 856–859, 2004.
- [26] J. Gyselinck, P. Dular, L. Krähenbühl, and R. V. Sabariego, “Finite-Element Homogenization of Laminated Iron Cores With Inclusion of Net Circulating Currents Due to Imperfect Insulation,” *IEEE Transactions on Magnetics*, vol. 52, no. 7209104, 2016.

- [27] S. Hiruma and H. Igarashi, "Model Order Reduction for Linear Time-Invariant System With Symmetric Positive-Definite Matrices: Synthesis of Cauer-Equivalent Circuit," *IEEE Transactions on Magnetics*, vol. 56, no. 7400608, 2020.
- [28] N. Köster, O. König, and O. Bíró, "Proper Generalized Decomposition With Cauer Ladder Network Applied to Eddy Current Problems," *IEEE Transactions on Magnetics*, vol. 57, no. 6300904, 2021.
- [29] O. Bíró and N. Köster, "Generating a Cauer Ladder Network Representation of Eddy Current Fields Using Scalar Potentials," *IEEE Transactions on Magnetics*, vol. 58, no. 7501204, 2022.
- [30] O. Bíró and M. Gyimesi, "Finite Element Implementation of the Iterative Scalar Potential Method for the Computation of Eddy Currents," *IEEE Transactions on Magnetics*, vol. 57, no. 6301704, 2021.
- [31] H. Eskandari and T. Matsuo, "Cauer ladder network representation of a non-linear eddy-current field using a first-order approximation," *IEEE Transactions on Magnetics*, vol. 56, no. 7505904, 2020.
- [32] T. Matsuo, T. Fujiwara, K. Kuriyama, K. Sugahara, A. Kameari, T. Tokumasu, and Y. Shindo, "Multi-port model order reduction using a matrix cauer ladder network," *IEEE Transactions on Magnetics*, vol. 56, no. 7506905, 2020.
- [33] T. Matsuo, K. Sugahara, A. Kameari, and Y. Shindo, "Model Order Reduction of an Induction Motor Using a Cauer Ladder Network," *IEEE Transactions on Magnetics*, vol. 56, no. 7514704, 2020.
- [34] Y. Takahashi, K. Fujiwra, K. Sugahara, and T. Matsuo, "Reduced Order Modeling Based on Multiport Cauer Ladder Network for Space Harmonics of Air-Gap Flux Density in Cage Induction Motor," *IEEE Transactions on Magnetics*, vol. 58, no. 8203306, 2022.
- [35] Y. Takahashi, K. Fujiwara, K. Sugahara, and T. Matsuo, "Model Order Reduction of Cage Induction Motor With Skewed Rotor Slots Using Multiport Cauer Ladder Network Method," *IEEE Transactions on Magnetics*, vol. 59, no. 8201004, 2023.
- [36] H. Whitney, *Geometric Integration Theory*, 1957.

-
- [37] A. Bossavit, *Computational Electromagnetism: Variational Formulations, Complementarity, Edge Elements*, 1998.
- [38] R. Hiptmair, “Finite elements in computational electromagnetism,” *Acta Numerica*, vol. 11, pp. 237–339, 2002.
- [39] R. Mitsuoka, T. Mifune, T. Matsuo, and C. Kaido, “A vector play model for finite-element eddy-current analysis using the Newton-Raphson method,” *IEEE transactions on magnetics*, vol. 49, no. 5, pp. 1689–1692, 2013.
- [40] F. Hecht, “New development in freefem++,” *Journal of Numerical Mathematics*, vol. 20, no. 3-4, pp. 251–266, 2012.
- [41] T. Matsuo and M. Shimasaki, “An identification method of play model with input-dependent shape function,” *IEEE Transactions on Magnetics*, vol. 41, no. 10, pp. 3112–3114, 2005.
- [42] S. Hiruma, S. Clénet, H. Igarashi, and T. Henneron, “Error Estimator for Cauer Ladder Network Representation,” *IEEE Transactions on Magnetics*, vol. 58, no. 7500904, pp. 1–4, 2022.
- [43] H. Nagamine, S. Hiruma, T. Mifune, and T. Matsuo, “Error Estimation of the Cauer Ladder Network Method Based on Eigenfunction Expansion,” *IEEE Transactions on Magnetics*, vol. 59, no. 7001604, 2023.
- [44] —, “Henrici-Pflüger-Type Error Estimators for the Cauer Ladder Network Representation,” *IEEE Transactions on Magnetics*, 2023.
- [45] J. Gyselinck, P. Dular, N. Sadowski, J. Leite, and J. Bastos, “Incorporation of a Jiles-Atherton vector hysteresis model in 2D FE magnetic field computations: Application of the Newton-Raphson method,” *COMPEL - The international journal for computation and mathematics in electrical and electronic engineering*, vol. 23, no. 3, pp. 685–693, 2004.
- [46] S. Bobbio, G. Miano, C. Serpico, and C. Visone, “Models of magnetic hysteresis based on play and stop hysterons,” *IEEE Transactions on Magnetics*, vol. 33, no. 6, pp. 4417–4426, 1997.
- [47] A. Benabou, S. Clénet, and F. Piriou, “Comparison of Preisach and Jiles–Atherton models to take into account hysteresis phenomenon for finite element analysis,” *Journal of Magnetism and Magnetic Materials*, vol. 261, no. 1, pp. 139–160, 2003.

- [48] T. Matsuo and M. Shimasaki, “Two types of isotropic vector play models and their rotational hysteresis losses,” *IEEE transactions on magnetics*, vol. 44, no. 6, pp. 898–901, 2008.

Publication List

Journal Publications

1. M. Tobita, H. Eskandari, and T. Matsuo, “Model order reduction of nonlinear eddy-current field using parameterized CLN,” *COMPEL - The international journal for computation and mathematics in electrical and electronic engineering*, Vol. 41 No. 3, pp. 967-980, 2022.
2. M. Tobita, and T. Matsuo, “Nonlinear Model Order Reduction of Induction Motors Using Parameterized Cauer Ladder Network Method,” *IEEE Transactions on Magnetics*, vol. 58, no. 9, Art no. 8205504, 2022.
3. M. Tobita, and T. Matsuo, “A Model Order Reduction of Hysteretic Eddy-current Fields in Electric Machines Using Cauer Ladder Network Method,” *AIP Advances*, vol. 13, no. 2, Art no. 025208, 2023.
4. M. Tobita, and T. Matsuo, “Nonlinear Model Order Reduction of a Variable Reluctance Stepper Motor Using the Parameterized Cauer Ladder Network Method,” *IEEE Transactions on Magnetics*, vol. 59, no. 5, Art no. 8200604, 2023.
5. M. Tobita, and T. Matsuo, “Hysteretic Finite Element Analysis Using a Semi-implicit Method Combined with the Predictor-Corrector Scheme,” *IEEE Transactions on Magnetics*, Early access, 2023.

Presentations in International Conference

1. M. Tobita, H. Eskandari, and T. Matsuo, “Model Order Reduction of Nonlinear Eddy-current Field Using Parameterized CLN,” 19th International IGTE Symposium, O4-1-4, Graz, Austria, on-site and online, Sep. 2020.

2. M. Tobita, and T. Matsuo, “Nonlinear Model Order Reduction of Induction Motors Using Parameterized Cauer Ladder Network Method,” Compumag2021, OB1-1, Cancun, Mexico, online, Jan. 2022.
3. M. Tobita, and T. Matsuo, “Nonlinear Model Order Reduction of a Variable Reluctance Stepper Motor,” CEFC2022, P10-6, Denver, Colorado, online, Oct. 2022.
4. M. Tobita and T. Matsuo, “A Model Order Reduction of Hysteretic Eddy-current Fields in Electric Machines Using Cauer Ladder Network Method,” MMM2022, PPC-04, FS-05, Minneapolis, US, on-site, Nov. 2022.
5. M. Tobita and T. Matsuo, “Hysteretic Finite Element Analysis Using a Semi-implicit Method Combined with the Predictor-Corrector Scheme,” Compumag2023, PA-A1:08, Kyoto, Japan, May 2023.
6. T. Matsuo, Y. Kawamura, and M. Tobita, “Predictor-Corrector Scheme for Dynamic Hysteresis Model,” 26th Soft Magnetic Materials Conference, WP-4, Prague, Czech Republic, Sep. 2023.

Honors

1. IEEJ Excellent Presentation Award, Sep. 2021.
2. Mazume Research Award for Young Scientists, July 2022.
3. JSPS Research Fellow (DC2), 2023–2024.
4. The Rita Trowbridge Prize, commendation for the best paper presented by young researchers, in Compumag2023, May 2023.
5. The Best Poster Presentation Award, in 26th Soft Magnetic Materials Conference, Sep. 2023.
6. IEEJ Excellent Presentation Award, Sep. 2023.